Denise Prutsch

Synthesis and Electrochemical Characterization of Nanostructured Anode Materials for Na-Ion Batteries

MASTERARBEIT

zur Erlangung des akademischen Grades

Diplom-Ingenieur

Masterstudium Technische Chemie

eingereicht an der

Technische Universität Graz

Betreuer:
Dr. I. Hanzu
Prof. Dr. M. Wilkening

Institut für Chemische Technologie von Materialien

Graz, im Oktober 2014

EIDESSTATTLICHE ERKLÄRUNG

AFFIDAVIT

Ich erkläre an Eides statt, dass ich die vorliegende Arbeit selbstständig verfasst, andere als die angegebenen Quellen/Hilfsmittel nicht benutzt und die den benutzten Quellen wörtlich und inhaltlich entnommene Stellen als solche kenntlich gemacht habe. Das in TUGRAZonline hochgeladene Textdokument ist mit der vorliegenden Masterarbeit identisch.

I declare that I have authored this thesis independently, that I have not used other than the declared sources / resources, and that I have explicitly indicated all material which has been quoted either literally or by content from the used sources. The text document uploaded to TUGRAZonline is identical to the present master's thesis.

…….. ……

Datum / date Unterschrift / signature

Abstract

Sodium-ion batteries are considered to be an attractive alternative to common lithium-ion systems due to its low cost and the high availability and even distribution of sodium resources. Although, so far, many materials have been proposed as suitable positive electrode materials, there is a relatively limited choice of suitable compounds operating at low Na^+ insertion potentials and thus able to serve as negative electrode active materials. In this work self-organized amorphous titania nanotubular arrays without any additives and binders are investigated as possible anodes for sodium-ion systems. The formation of highly parallel self-assembled TiO_2 nanotubes having various lengths and diameters was achieved by anodic oxidation of Ti foils in a fluoride containing viscous electrolyte based on ethylene glycol at potentials between 30-60 V and different anodization times. For electrochemical characterization, the as-anodized tubes were galvanostatic cycled in Na half-cells at constant current rates using two different electrolyte formulations, one based on $NaClO_4$ and the other one based on $NaPF_6$. These TiO_2 nanotubes-based electrodes presented excellent cycling stability and high rate capability offering specific capacity values up to 65 mAh/g and 70 mAh/g at 50 mA/g and 25 mA/g, respectively. Furthermore, stable cycling performance can be shown for 300 cycles without significant capacity fade.

In this work, also the influence of different electrolyte additives on the formation of electrochemically passive films on sodium metal was studied. It has been found that VC, FEC and 2,3,4-trifluorophenylisocyanate are effective corrosion inhibitors in combination with a 1 M solution of $NaClO_4$ in PC as electrolyte. For 0.6 M $NaPF_6$ in a EC:DMC mixture (3:7) VEC is the most suitable.

Kurzfassung

Natrium-Ionen Batterien stellen aufgrund ihrer niedrigen Kosten als auch der hohen Verfügbarkeit und gleichmäßigen Verteilung der Natrium Ressourcen eine attraktive Alternative zu den herkömmlichen Lithium-Ionen Systemen dar. Obwohl bereits eine Vielzahl an Kathodenmaterialen erforscht wurde, existiert nur eine geringe Auswahl an Materialen, die Natrium Ionen bei geringen Potentialen aufnehmen können und damit als geeignete negative Elektrodenmaterialien in Frage kommen. In dieser Arbeit werden selbstorganisierte, amorphe TiO_2-Nanoröhren ohne Zugabe von Zusatzstoffen und Bindemitteln als mögliche Anodenmaterialien vorgeschlagen. Die Synthese dieser TiO_2-Nanoröhren unterschiedlicher Länge und mit verschiedenen Durchmessern erfolgte dabei durch anodische Oxidation von reinen Titanfolien bei Potentialen zwischen 30-60 V für unterschiedliche Zeiten. Als Elektrolyt wurde Ethylenglykol mit einem Zusatz von NH_4F verwendet. Zur elektrochemischen Charakterisierung diente galvanostatische Zyklisierung in Natrium Halbzellen bei konstanten Stromraten unter Verwendung von zwei verschiedenen Elektrolyten. Solche auf TiO_2-Nanoröhren basierende Elektroden zeigten hervorragende Zyklenstabilität und hohe Leistungsfähigkeiten, wobei spezifische Kapazitäten von 65 und 70 mAh/g bei Stromraten von 50 und 25 mA/g erreicht wurden.
In dieser Arbeit wurde auch der Einfluss verschiedener Additive auf die Bildung von Passivierungsschichten auf Natriummetall untersucht. Es hat sich gezeigt, dass VC, FEC und 2,3,4-Trifluorophenylisocyanate effektive Korrosionsinhibitoren in Kombination mit einer 1 M Lösung von $NaClO_4$ in PC als Elektrolyt sind. Für eine 0,6 M Lösung von $NaPF_6$ in einer EC:DMC Mischung ist VEC am besten geeignet.

Table of Contents

List of Abbreviations

ZEBRA	zero emission battery research activities
NASICON	sodium super-ionic conductor
NaTFSI	sodium bis-trifluoromethanesulfonylimide
DEC	diethyl carbonate
DMC	dimethyl carbonate
DME	dimethyl ether
EC	ethylene carbonate
PC	propylene carbonate
THF	tetrahydrofuran
SEI	solid electrolyte interphase
VC	vinylene carbonate
FEC	fluoroethylene carbonate
VEC	vinyl ethylene carbonate
UV	ultraviolet
CV	cyclic voltammetry
GPCL	galvanostatic cycling with potential limitation
CA	chronoamperometry
EIS	electrochemical impedance spectroscopy
SEM	scanning electron microscopy
XRD	x-ray diffraction
CVA	cyclic voltammetry advanced
EDX	energy dispersive x-ray spectroscopy
CE	counter electrode
RE	reference electrode
WE	working electrode
SCE	saturated calomel electrode
NT	nanotube
R	resistance
CPE	constant phase element

1 Introduction

Apart from the already well-established Li-ion technology, an emergent area of interest in advanced electrochemical energy storage is constituted by the sodium-ion technology[1–4]. It is interesting to notice that research on Li-ion and Na-ion systems was done in parallel in the early 1980s[5], however investigations of sodium-ion batteries were almost abandoned after the commercial success of Li-ion systems. Reasons for the renewed interest in these systems are based on various economical and political interests, such as very low cost and very good availability of sodium or the even distribution of Na resources compared to economically viable lithium containing minerals. Although sodium-based batteries are in general expected to have lower specific capacity and energy than Li-ion battery systems, Na-ion technology may be a solution of choice for medium and large scale applications such as household or grid-relevant batteries, where low cost as well as an extended cycle-life would represent very valuable assets[4]. However, sodium chemistry in Na-ion galvanic cells differs from lithium making it seldom possible to directly translate the knowledge accumulated in the last two decades for lithium to the sodium-based systems.

Historically, the first compounds that were shown to reversibly intercalate sodium ions were various sodium bronze phases[5]. Since then, these materials have been significantly improved[6] and a large variety of other new compounds emerged, such as transition metal fluorides[7], phosphates[8] and fluorophosphates[9], olivines[10], NASICON framework compounds[11] etc. All these materials will undergo a reaction with sodium at high potentials vs. Na^+/Na reference redox couple making them suitable as positive electrode (cathode) materials.

On the other hand, there is a relatively limited choice of suitable compounds that can serve as negative electrode (anode) material. From the beginning, it was noticed that battery systems based on sodium metal as negative electrode material are more complicated to use than metallic Li anodes due to the low melting point of Na (97.7 °C), its higher reactivity with air, moisture, organic compounds etc. and its pronounced tendency to form dendrites during Na plating when the cell is recharged[12]. Thus, high performance host materials that are able to reversibly insert sodium ions at low potentials are needed. So far few hard carbon materials[13–15], some Sn-Sb/C intermetallic nanocomposites[16–19] as well as Sn-Cu alloys[20] and nanostructured Ge[21] were reported to present significant sodium storage capacities. However, many of these materials have less than optimum cycle life. Recently also the use of titanium-based materials[22–25] for negative electrodes in Na-ion batteries was demonstrated. The sodium titanate phase $Na_2Ti_3O_7$ was shown to

have one of the lowest sodium insertion potential for an oxide material[26]. Another interesting material is titania, which has relatively re-emerged as a possible negative electrode material for Li-ion batteries[27–29] showing high rate capability and excellent availability. Although some initial reports showed that anatase titania cannot reversibly insert sodium[30], very recently, nanostructured TiO_2 was in fact demonstrated to be able to serve as host material for sodium ions[31].

In this work a detailed electrochemical study of sodium insertion into self-organized amorphous titania nanotubes prepared by anodic oxidation from non aqueous electrolytes based on ethylene glycol is presented. The highly parallel self-assembled titania nanotubular arrays were tested using common electrochemical techniques in the absence of any other additives such as conductive agents or binders. Galvanostatic cycling experiments were carried out routinely for over 200 cycles at constant current rates of 50 mA/g and 25 mA/g in the potential ranges of 0.8-2 V and 0.1-2 V using two different electrolyte formulations namely 1 M $NaClO_4$ in PC and 0.6 M $NaPF_6$ in EC:DMC (3:7 per weight%). The morphology and the structure of the nanotubes were characterized by means of SEM and XRD analysis.

The second aim of this work was to study the effect of different electrolyte additives on the formation of surface passivation films on sodium metal electrodes using electrochemical impedance spectroscopy.

2 Theoretical Part

2.1 Rechargeable Sodium-Ion Batteries

2.1.1 General

Rechargeable batteries are nowadays indispensable and constitute an integral part of many advanced technologies and devices. For instance, lithium-ion batteries dominate the market of portable electronics[32]. They attract a significant interest because of their high voltage they can supply and thus their high energy density. The high voltages and energy densities are a direct consequence of the very low redox potential of the Li^+/Li redox couple ($E°_{(Li+/Li)}$ = -3.04 V vs. SHE)[2] and the small atomic mass of lithium (6.941 g/mol)[12]. Thanks to their long cycle life and also good rate capability of advanced systems[2], lithium-ion batteries are also proposed and currently developed as a key technology for electric vehicles and stationary storage applications[32]. However, to meet the demand for large scale stationary energy storage, much more lithium needs to be used in the future. Since the abundance of Li in the Earth crust is low and many global reserves are located in geographically constrained and political unstable areas, the price for lithium will probably rise at some point, making large scale energy storage very expensive[1].

Sodium is a low cost element of high natural abundance[1] that can easily and cost-effectively extracted from low toxic resources and minerals[12]. Sodium shares with lithium many similar chemical and physical properties as the element Na can be directly found below Li in the periodic table. Thanks to the low standard potential of the Na^+/Na redox couple ($E°_{(Na+/Na)}$ = -2.71 V vs. SHE)[2], sodium-based batteries may be a reasonable alternative to lithium-ion batteries for large scale storage applications as well as other markets[1]. Until now, sodium-based electrochemical storage technology has already been successfully utilized in sodium/sulphur and Na/$NiCl_2$ ZEBRA batteries, both working at high temperatures[3]. Considering this existing experience with sodium and the already advanced knowledge in the field of lithium-ion technology, the design and realization of a room temperature sodium-ion (Na-ion) cell seems plausible and justified.

However, there are obvious fundamental differences between Li and Na related to chemical reactivity and ionic properties such as ionic radius, solvation and ionic mobility, diffusion properties etc. Thus, most of electrode materials as well as electrolyte formulations, developed for Li-ion technology, cannot be directly adopted and translated to sodium-ion battery systems.

Indeed, sodium has a lower gravimetric capacity (1165 mAh/g compared to 3829 mAh/g for lithium) as well as a 300 mV higher standard reduction potential than Li, leading to lower operating voltages and lower energy densities in comparison to lithium. Furthermore, Na has a larger ionic radius (1.02 Å compared to 0.76 Å for Li) and also a three times larger mass. Therefore, the channels and the interstitial sites of the intercalation materials must be wide enough to successfully incorporate the larger Na^+ cations[1]. All these differences lead to different interactions between the intercalation host material and the sodium ions, influencing the thermodynamic as well as the kinetic properties of sodium-ion batteries[12]. Thus, the development of new electrode materials, for both positive and negative sides, as well as new stable electrolyte formulations is necessary to reach a competitive basis with the current Li-ion battery systems.

2.1.2 Build-up of a Sodium-Ion Battery

A battery is the combination of several electrochemical cells, connected either in series or parallel, or both, in order to meet the required electrical output. Each of these cells is made up of three major components[33]:

1. A negative electrode (also commonly referred to as anode) that sources electrons to the external circuit and is hence oxidized during cell discharge. A good negative electrode should be stable in contact with the electrolyte, should be able to insert ions reversibly, has a high electrical and ionic conductivity, be easy to fabricate from available precursors and be reasonably low priced[33].
2. A positive electrode (cathode) acts as a sink of electrons from the external circuit and is thereby reduced during cell discharge. The positive electrode should exhibit the following properties: stability in contact with the electrolyte within its working potential range and an advantageous working potential[33].
3. An electrolyte that acts as transport medium for charges, in this case sodium ions, between the positive and the negative electrode. Usually, the electrolyte consists of a liquid, such as solvents or water, in which different salts, alkalis or acids are dissolved in order to provide ionic conductivity. Sometimes, also solid electrolytes are used as ionic conductors. Some key properties that a good electrolyte should present are: high ionic conductivity while having only insignificant electronic conductivity, thermal stability that is associated with a safe behaviour, low production costs and, very important, no reactivity with the electrode active materials[33].

In the cell the positive and the negative electrode are mechanically spaced using a separator material that is however permeable to the electrolyte[33].

2.1.2.1 Negative Electrode Materials

Compared to metallic Li anodes, battery systems based on sodium metal as negative electrode material are even more problematic to use at ambient temperatures due to the low melting point of sodium (97.7 °C), dendritic metallic Na formation during cell charge process as well as the high chemical reactivity and unstable passive layer in most of the known electrolytes. These phenomena will induce a poor cycle life of sodium metal electrodes, may lead to short-circuits and other important safety hazards that would make such a cell impractical[1,12].

Finding a suitable negative electrode intercalation material for NIBs is also a significant challenge, since reaction pathways, chemistries and structures are different when sodium instead of lithium is used. Fig. 1 shows a synthetic view of the possible negative electrode materials for sodium-ion batteries. The most important are described and discussed in more detail below.

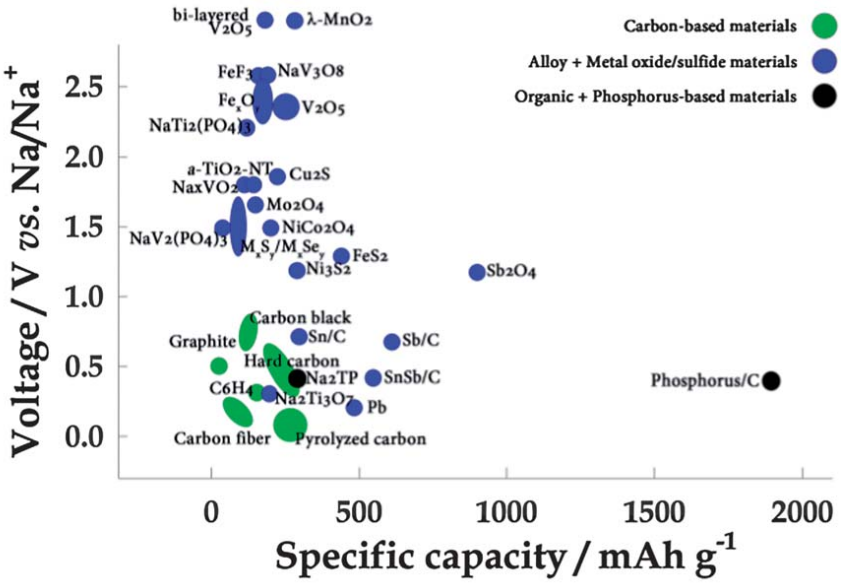

Fig. 1. Voltage vs. capacity plotted for different negative electrode materials for sodium-ion batteries; (adapted from Ref. [12])

2.1.2.1.1 Carbon-Based Materials

Graphite, which is the most commonly used negative electrode material for Li-ion batteries, cannot act as an insertion material in sodium-ion systems, since Na^+ does not intercalate between the graphite layers[1,34,35]. Presently, many other non-graphite carbonaceous materials (petroleum cokes[36,37], carbon fibers[38], carbon blacks[39] and polymers[40]) with different morphologies, such as nanowires[41], hollow carbon spheres[42], porous nanosheets[43] as well as template-made carbons[44] have been demonstrated to insert Na. Hard carbons[45,46], however, promise to be the best alternative to graphite as sodium can be successfully reversible inserted into the nanoporous voids of the disordered graphene stacks[12] leading to an electrochemical sodium insertion potential relatively similar to that of the Na metal itself[2].

2.1.2.1.2 Alloys

Alloy materials have attracted significant interest as negative electrode active materials because of their relatively high theoretical specific capacity[12]. Sn[47,48] as well as Sb-based materials[49] exhibit very good cyclability, when they are used in sodium-ion batteries. Furthermore, Sn/C[50], Sb/C[51] and SnSb/C[17] nanocomposites, which show good rate capability, high capacities and good stability during cycling, were proven as negative electrode materials. However, sodium insertion in these alloy materials is accompanied by large volume changes, which lead to unstable electrodes[4].

2.1.2.1.3 Metal Oxides and Sulfides

Titanium oxides promise to be a good choice as anode material because of their non-toxicity, low costs and their low redox potential[12]. Sodium titanate $Na_2Ti_3O_7$, for example, can reversible insert two sodium ions at a low voltage of 0.3 V vs. Na[26]. However, this material shows unsatisfactory cyclic and rate performance[4]. Sodium insertion is also observed in amorphous TiO_2 nanotubes with a diameter > 80 nm taking the larger size of Na^+ cations into account[25]. Due to their low intercalation potential for Na, vanadium oxides[52,53] have been proposed as negative electrodes too, but their high sensitivity to oxygen as well as the voltage fluctuations during cycling are challenging and difficult to tackle[2]. Through conversion reaction mechanisms of some metal oxides, for example $NiCo_2O_4$[54], Sb_2O_4[55], further host materials for Na ions are accessible.
Regarding the sulfides, TiS_2[56], TaS_2[56], MoS_2[57] as well as Ni_3S_2[58] and FeS_2[59] phases are also a possible option as negative electrode materials for sodium-ion batteries.

2.1.2.1.4 Organic Compounds

In order to meet the increasing demand for low-cost electrode materials from sustainable resources, batteries based on organic compounds promise to be a good solution thanks to their high structural diversity, reasonably low costs and recyclability. Nevertheless, some inherent disadvantages exist such as a poor electronic conductivity, poor cycleability and a relatively small volumetric capacity. For moment, disodium terephthalate shows the best performance in sodium-ion battery systems, but more research must be done to overcome the above mentioned problems[12].

2.1.2.1.5 Phosphorous-Based Compounds

Recently, amorphous red phosphorus/carbon composites have been developed as negative electrodes. With this material the highest reversible capacity can be achieved among all already existing negative electrodes for sodium-ion batteries[60].

2.1.2.2 Positive Electrode Materials

Materials that can reversibly insert sodium ions at a voltage of at least 2 V vs. Na^+/Na are considered to be suitable for use as positive electrodes for sodium-ion batteries. To ensure a good battery cycling performance over a long period of time, the volume changes of the material during sodiation and de-sodiation should be as small as possible[1]. Compared to negative electrode materials and electrolytes, research on positive electrodes has been more successful providing a large number of possible materials (see Fig. 2).

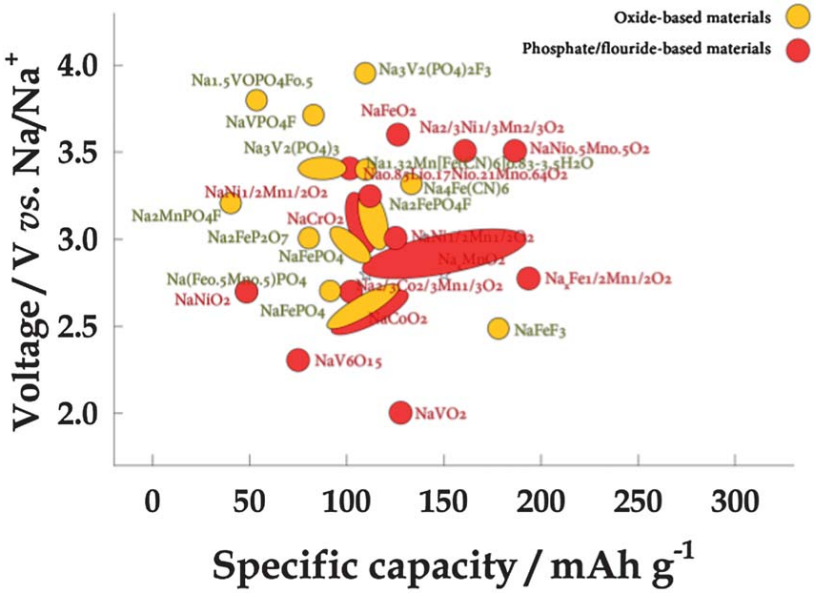

Fig. 2. Voltage vs. specific capacity plotted for positive electrode materials for NIBs; (adapted from Ref. [12])

2.1.2.2.1 Oxides

Layered structure oxides of the type $NaMO_2$ (M= transition metal) exhibit high capacity, relatively low material costs, when a convenient transition metal is used, as well as high energy densities doubled by high intercalation potentials, which make them promising materials for positive electrode systems[2,3]. In these oxides, the sodium ions can usually be found between the layers of the edge-shared MO_6 octahedra, analogue to the Li ions in the $LiMO_2$ compounds. Since the layered oxides may present many crystallographic configurations as a function of the transitional metal nature, various intercalation sites between the layers are possible for the sodium cations resulting in different electrochemical performances of each type. Although Na layered oxide materials seem to resemble their lithium counterparts, some differences in the structure occur due to the larger size of sodium[3]. This may also mean that materials that might be unusable in lithium-ion batteries may actually work as positive electrode materials in sodium-ion batteries. Na_xNiO_2[61], $NaCrO_2$[62–64] and Na_xCoO_2[65] have been currently investigated as potential positive electrodes. In order to improve their electrochemical performance, layered oxides with various transition metal mixtures[3] such as $Na_{0.58}Ni_{0.6}Co_{0.4}O_2$[66] and $Na_{0.66}Mn_{0.33}Co_{0.66}O_2$[67] have also been developed.

Furthermore, the oxides with a tunnel-type structure[12], such as the orthorhombic $Na_{0.44}MnO_2$[68,69], are also promising positive electrode materials. They offer better cycling stability, since stress due to structural changes can be better tolerated[2]. For instance, $Na_{0.44}MnO_2$ nanowires[70] have been recently investigated. λ-MnO_2[71] shows electrochemical activity to reversible Na insertion, although a total rearrangement of the lattice is necessary in order to intercalate Na in these structures[1].

From the oxides containing iron, nanocrystallized Fe_3O_4[72] as well as α-Fe_2O_3[73] can be mentioned. Vanadium oxides, either available in a channel-type (β-$Na_xV_2O_5$) or layered-type structure (α-V_2O_5 and $Na_{1+x}V_3O_8$) can be used as positive electrode materials[74]. However, a combination with pre-sodiated anodes or metallic Na is necessary, since these oxides are synthetized in the charged state and do not contain sodium[1].

2.1.2.2.2 Phosphate-Based Materials

Phosphate-based materials are promising candidates for positive electrodes in sodium-ion batteries, since phosphates are characterized by high thermal and structural stability, good safety and higher redox potential in the case of transition metals resulting from the relatively strong oxygen-phosphorus bond and the inductive effect of the polyanions PO_4^{3-}[4,12]. To overcome the negative aspects such as the low conductivity (ionic and electrical), nanosized phosphate materials are used in order to decrease the diffusion lengths of the ions[12].

Among all electroactive phosphate materials olivine $NaFePO_4$ shows the highest specific capacity. Amorphous $FePO_4$/C nanocomposites have been investigated. They were found to offer improved kinetics and less structural changes during cycling[3].

$Na_xM_2(PO_4)_3$ NASICON type compounds, containing transition metals (V, Fe, Ti, Nb) in their structure, can also serve as positive electrode materials. Their three-dimensional open framework provides large interstitial spaces for sodium diffusion[75,76]. In particular, the vanadium containing $Na_3V_2(PO_4)_3$ phase is considered as a possible electrode material[77,78]. However, since vanadium is toxic and relatively rare, more research has to be done on abundant and non-toxic elements[4].

Combining phosphates with fluorides leads to a new structural class of host materials for Na ions[4]. Particularly, sodium vanadium fluorophosphates as well as sodium iron-manganese fluorophosphates have been identified and proved to be promising electroactive materials[3].

Furthermore, pyrophosphates $Na_2MP_2O_7$ (M= Co, Fe, Mn, etc.) attract attention as possible positive electrodes for Na-ion batteries due to their very strong 3-D framework providing multiple sites for the Na insertion. However, since the pyrophosphate anions $(P_2O_7)^{4-}$ are bigger than phosphates, lower theoretical specific capacities are achieved[3].

2.1.2.2.3 Other Positive Electrode Materials

$NaMSO_4F$ materials[79], where M is a transition material, are reported as possible positive electrodes. In spite of their high Na^+ ionic conductivity, Na extraction from their structures is not energetically favored[1].

Layered sulfides, such as Na_xTiS_2[80], provide large voids for sodium intercalation, however their working voltages are low compared to that for layered oxides or poly-anionic compounds[1].

Perovskite-type transition metal fluorides of the type $NaMF_3$[81] (M=Fe, Mn, Ni), especially those with iron as a transition metal, can be mentioned as possible electrode materials. However, they exhibit slow kinetics resulting in low energy conversion efficiencies[4].

Since materials with open frameworks and hence large interstitial spaces are a good choice to handle the larger size of Na^+ ions, Prussian Blue derivates, $KMFe(CN)_6$ (M= Mn, Fe, Co, Ni, Zn)[82] and $Na_xMnFe(CN)_6$[83], are also proved compounds that can function as Na^+ host materials in sodium-ion batteries. Besides their non-toxicity, possible synthesis from low-cost cations as well as their very good electrochemical properties are advantageous[3].

Finally, polymeric electrodes represent another class of electroactive materials for Na-ion batteries. They exhibit good cyclability doubled by a good rate capability, since the polymer matrix is more flexible than the inorganic lattice, avoiding thus significant structural changes occurring during the insertion of the larger sodium ions[3].

2.1.2.3 Electrolytes

Electrolytes play an important role for the proper functioning of any battery system since they can also dramatically influence the electrochemical performance of a cell, its calendar and shelf life and even dictate the cell overall intrinsic safety characteristics and limitations. To be considered as a good electrolyte (i) no reactivity with the other cell components should occur, (ii) the ionic conductivity should be high and (iii) the electrochemical as well as the thermal stability window should be large enough to allow cell operation. The ionic conductivity, one of the most important factors affecting the performance of a battery, is influenced by the viscosity of the electrolyte (lower viscosity means higher ion mobility), the number of Na^+ cations and counter ions transported and the degree of salt dissociated (determined by the solvent's dielectric constant). To comply with the large electrochemical window, the electrolyte should be able to withstand both very high (oxidation) and low (reduction) electric potentials. Also for liquid electrolytes melting points lower and boiling points higher than the temperature range, in which the battery operates, are necessary. Additional factors that must be considered are costs and toxicity[32].

For the use in sodium-ion batteries different combinations of sodium salts ($NaClO_4$, $NaPF_6$, NaTFSI) with solvents (DEC (diethyl carbonate), DMC (dimethyl carbonate), DME (dimethyl ether), EC (ethylene carbonate), PC (propylene carbonate), THF (tetrahydrofuran), triglyme) and/or solvent mixtures (EC:DMC, EC:DME, EC:PC and EC:triglyme) have been investigated. It has been found that $NaClO_4$ or $NaPF_6$ dissolved in PC or in the EC:PC mixture are most suitable for electrolytes in sodium-ion batteries[32]. Propylene carbonate possesses the advantages of high chemical stability, high dielectric constant, low melting point as well as high boiling point that make it an attractive solvent for the use in batteries[84]. Ethylene carbonate shows a high dielectric constant value too, however its main disadvantage is the high melting point of 36.4 °C. But in combination with PC as co-solvent no electrolyte solidification occurs within the ambient temperature range[32].

2.1.2.3.1 Electrolyte Additives

Currently, sodium-ion batteries show a limited lifetime. One of the reasons behind this is the continuous degradation of electrolyte during cycling. However, it has been learned from Li-ion systems that cyclability can be improved and further electrolyte reduction/oxidation could be avoided, when a stable passivation layer, consisting of insoluble electrolyte decomposition products, is formed on the electrode surfaces[85]. This so-called solid electrolyte interphase (SEI) is on one hand electronically insulating preventing further electrolyte decomposition and hence improving the electrolyte stability, while on the other hand ionically conducting for the Li^+ cations. Since the main components of the SEI layer are the solvent and salt, organic and inorganic degradation products, their composition has a strong influence on the ionic conductivity, stability and thickness of the film[86].

Since Na-ion negative electrodes show very unstable SEI layers compared to lithium-ion batteries[4], the use of carefully chosen electrolyte additives may be one possibility to facilitate the formation of a stable layer. For lithium-ion systems many electrolyte additives have been already developed to improve the formation of the passivation layer; their use may also possibly lead to stable SEI layers in sodium-ion batteries. However, not much research has been done on that till now. Generally, these additives can be divided into two groups, depending on how the support the generation of the SEI[87]. The required concentration of the additive in the main solvent should be low. Usual additive concentrations are approximately 1% v/v or below[88].

2.1.2.3.1.1 Reduction-Type Additives

This type of additives exhibits a similar oxidation potential, but a higher reduction potential compared to the electrolyte solvent. The result is that these additives are preferentially reduced forming a solid insoluble product, which covers hereafter the surface of the negative electrode, before the electrochemical reduction of the main solvent starts. This kind of additives contains one or more C=C bonds in their structure. Examples are vinylene carbonate (VC, 1), fluoroethylene carbonate (FEC, 2) and vinyl ethylene carbonate (VEC, 3)[87].

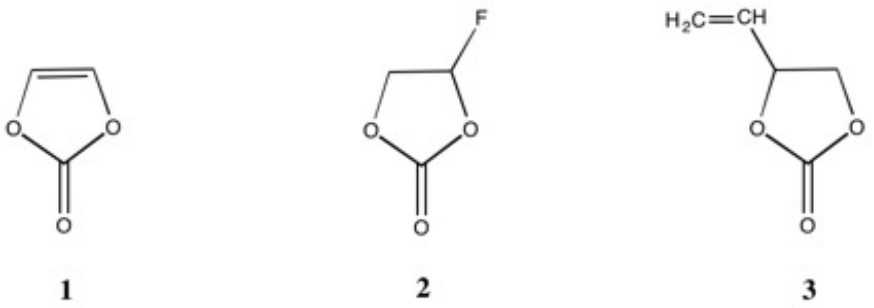

Fig. 3. Examples of chemical structures of reduction-type additives

An electrochemically induced polymerization constitutes the basis of the mechanism[87]:

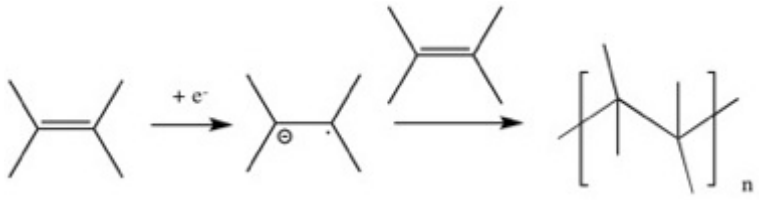

First, the reduction of the vinyl group takes place, generating a radical anion. Then, this anion has the possibility to react with the main solvent, the electrolyte salt, other vinylene compounds or with all of them, resulting in solid insoluble products as a temporary SEI nuclei, on which reduction products from other components of the electrolyte can then grow. This leads to a SEI layer consisting of polymerization as well as reduced products[88]. The activity of these polymerizable additives depends on the strength of the adhesion of the polymer on the electrode surface and the efficiency of the reductive polymerization[87].
Fluoroethylene carbonate, however, does not contain a reducible vinyl group in its structure. But by the loss of a HF molecule, FEC is converted into a vinylene carbonate molecule that can then participate in the polymerization mechanism, as shown below[87]:

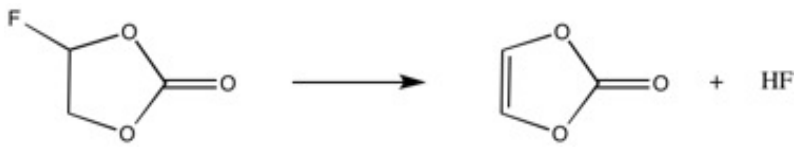

2.1.2.3.1.2 Reaction-type Additives

This kind of additives do not undergo any reduction processes in contrast to the previously described additives, but they can either eliminate intermediates of the electrolyte solvent reduction, such as radical anions or can react with final products, such as alkoxides and dicarbonates resulting in more stable SEI products. Examples are halogenated aromatic isocyanate compounds, such as 4-fluorphenyl isocyanate (4) and 2,3,4-trifluorophenyl isocyanate (5)[87].

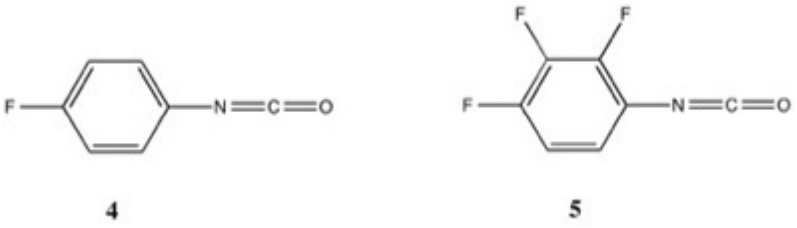

Fig. 4. Examples of chemical structures of reaction-type additives

These isocyanates are in fact multifunctional additives, as they can fulfil several functions. First, the isocyanate molecules can react with oxygen groups (such as carboxyl and phenol) that are chemisorbed on the surface of the negative electrode forming more stable products as below[89]:

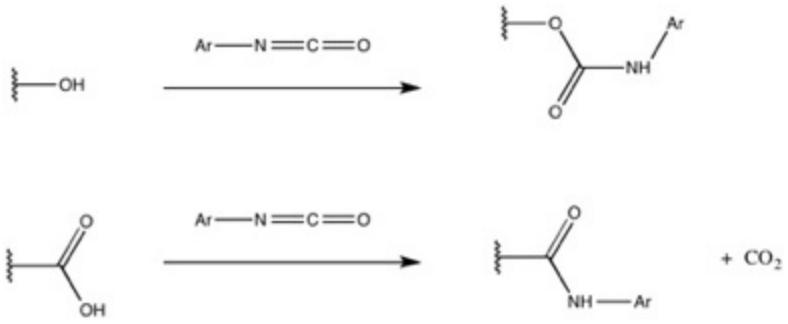

Since these have a higher affinity for the occurring electrolyte decomposition products, nucleation and growth of the SEI is promoted and further solvent reduction is inhibited. Second, the isocyanate group shows a high reactivity to acidic HF and water in the electrolyte[89]:

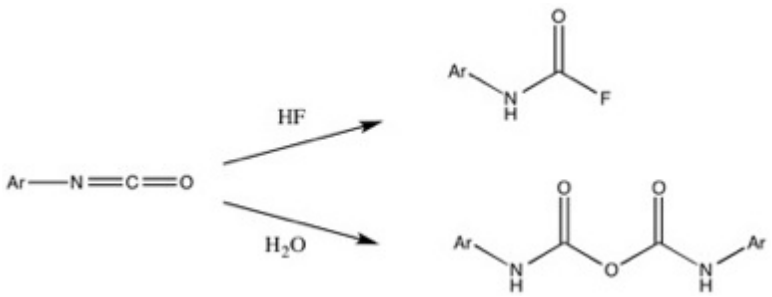

Given that these impurities are responsible for the dissolution of the positive electrode materials and the further decomposition of the SEI components, capacity fading can be thus minimized, when the isocyanate additives scavenge them[89].

2.1.3 Operation Principle of a Sodium-Ion Battery

The operation principle of a sodium-ion battery is based on a so-called intercalation process. This means that the negative electrode material as well as the positive electrode act as an intercalation host, where the sodium ions, referred to as the guest-ions, can be reversibly inserted or removed. When a sodium-ion cell is charged, the electrons flow through the external circuit from the positive electrode, which is oxidized, to the negative electrode, where reduction takes place. At the same time, sodium-ions are de-inserted/removed from the positive material and migrate through the electrolyte towards the negative material, where they are inserted. On discharge the process reverses. The positive electrode is now reduced and the negative electrode oxidized, resulting in a de-insertion process of the Na^+ ions from the negative material and in an incorporation of the same species in the positive material[33]. The charge-discharge process is graphically illustrated in Fig. 5.

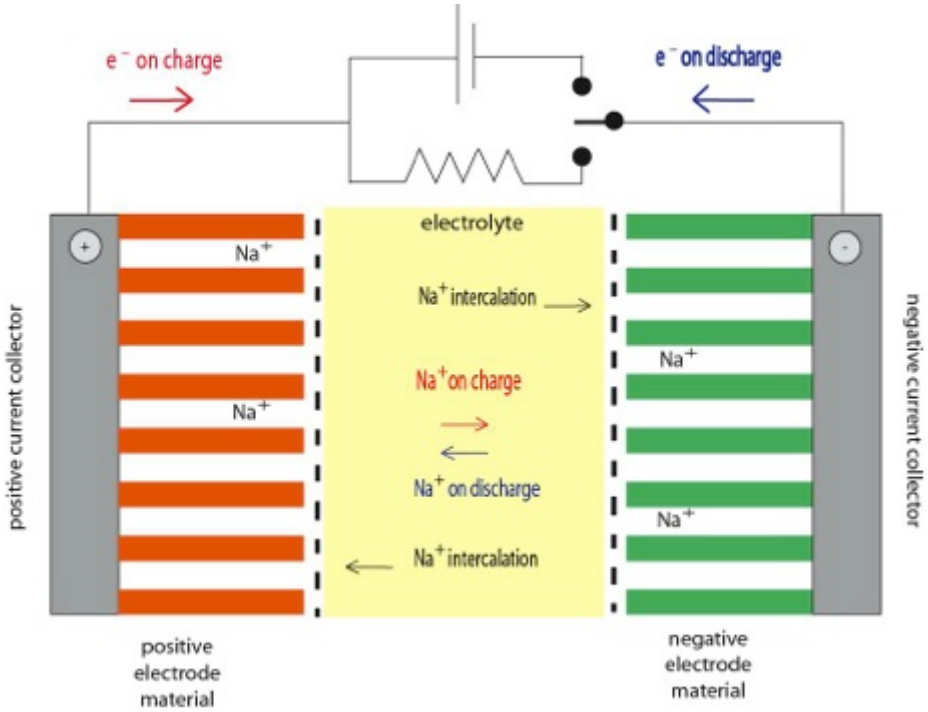

Fig. 5. Schematic of insertion/de-insertion processes in sodium-ion batteries taking place at the positive and negative electrodes.

2.2 TiO_2-Nanotubes

2.2.1 General

In the last decades, one-dimensional nanostructured materials (nanowires, nanofibers, nanorods and nanotubes) have attracted a great deal of attention in science and technology due to the combination of extraordinary geometrical features and exciting properties. For instance, much effort has been invested in the formation of carbon nanotubes, which may play an important role in microelectronic applications. In the context of advanced materials research and development, the synthesis and characterization of transition metal oxide nanostructures become more and more important, opening unmatched opportunities towards photochemical, electronical, biomedical and environmental applications[90]. In particular, TiO_2 nanotubes have attracted significant interest. These nanotubular structures, that usually feature a large surface area and a highly defined geometry[91], possess unique properties such as non-toxicity, high oxidative power, resistance to corrosion, potential photocatalytic activity, environment-friendliness and even biocompatibility characteristics[90,92]. Moreover, it is possible to modify and tune these properties, resulting in a wide range of already proven applications including self-cleaning coatings[93], dye-sensitized solar cells[94], gas sensing[95], switching electrochromic devices[96], rechargeable batteries[25], electrocatalysis[97], photocatalysis[98] and biomedical applications[99].

Among various routes that have been developed to fabricate nanotubular TiO_2 systems such as sol-gel processes[100], soft- or hard-templating approaches[101] or hydro/solvothermal methods[102], electrochemical anodization in fluoride-containing electrolytes seems to be most effective to produce self-organized TiO_2 nanotube layers[90,103]. Under optimized conditions, highly ordered, vertically aligned and closely packed tubes can be formed[104]. Furthermore, simple fabrication techniques and low costs constitute important advantages of this technique[105].

2.2.2 Formation and Growth of TiO_2 Nanotubes by Anodic Oxidation

As mentioned above, self-organized TiO_2 nanotubes can be obtained by anodic oxidation of metallic Ti in fluoride-containing electrolytes. Today, organic electrolytes, such as ethylene glycol or glycerol that contain both ammonium fluoride as a F^- ion source and small amounts of water, have been proven and are commonly used[106]. The anodization process is carried out at constant voltage in a simple electrochemical configuration as shown in Fig. 6.

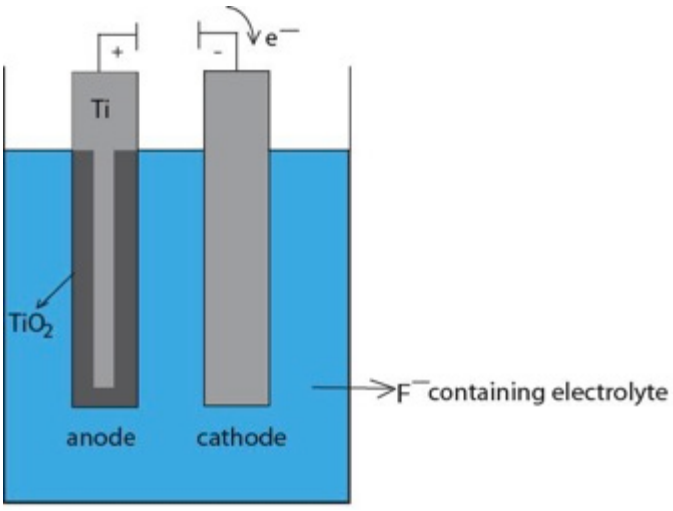

Fig. 6. Experimental set-up for the anodization process.

This leads to the oxidation of the Ti metal [Eq. (1)] and the formation of a compact oxide film [Eq. (2)] as initiation layer on the titanium substrate due to the reaction of the formed Ti^{4+} ions with the O^{2-} ions provided from the water in the electrolyte. Parts of this initial layer can sometimes be found on the tube tops after anodization[90].

$$Ti \rightarrow Ti^{4+} + 4e^{-} \quad (1)$$

$$Ti^{4+} + 2O^{2-} \rightarrow TiO_2 \quad (2)$$

After this initiation step, further growth of the oxide layer takes place, controlled by the high-field transport of the mobile Ti^{4+} and O^{2-} ions through the oxide film. Since the migration of these ionic species happens simultaneously, growth of new oxide occurs at both the metal/oxide and the oxide/electrolyte interfaces, depending only on the rate of migration of the involved ions. At the interface between metal and oxide the inward migrating O^{2-} ions react with the Ti metal [Eq. (3)][106], resulting in the formation of a compact and stable TiO_2[90], while at the oxide/electrolyte interface reaction between the outward migrating titanium ions and water occurs [Eq. (4)][106] and a less-dense oxide layer is formed[90].

$$Ti(s) + 2O^{2-} \rightarrow TiO_2(s) + 4e^{-} \quad (3)$$

$$Ti^{4+} + 2H_2O(l) \rightarrow TiO_2 + 4H^{+} \quad (4)$$

In Fig. 7 the processes during oxide growth are schematically shown:

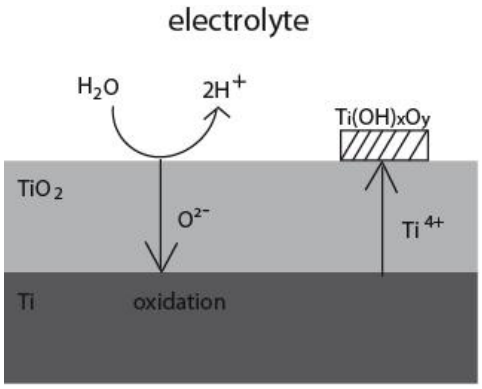

Fig. 7. Schematic representation of the high-field transport of the mobile Ti^{4+} and O^{2-} ions through the oxide film and the resulting oxide growth.

The as mentioned anodic reactions often go along with oxygen evolution at the anode [Eq. (5)], in which the amount of oxygen evolved depends on the water content in the electrolyte[106]:

$$H_2O(l) \rightarrow O_2(g) + 4H^+ + 4e^- \quad (5)$$

Simultaneously, as counter reaction, evolution of hydrogen takes place at the cathodic side [Eq. (6)][106]:

$$2H_2O(l) + 2e^- \rightarrow H_2(g) + 2OH^- \quad (6)$$

Since anodization is carried out under a constant voltage, further growth of the oxide layer leads to a decrease of the involved electric field, making the process self-limiting. Hence, the applied voltage alone defines the final thickness of the initial compact oxide film[107].
While this first stage in the electrochemical formation of nanotubular structures is independent of the fluoride ions present in the electrolyte and can be compared with the growth of barrier-oxide layers observed for example on Al, the subsequent formation of the nanotubes can be directly related to the presence of F^- ions. These fluorides can affect the further anodization process in two ways. On one hand, they can form a water-soluble $[TiF_6]^{2-}$ complex with the Ti^{4+} ions arriving at the oxide/electrolyte interface [Eq. (7)] and on the other hand dissolution of the formed TiO_2 can occur. [Eq. (8)][106]

$$Ti^{4+} + 6F^- \rightarrow [TiF_6]^{2-} \quad (7)$$

$$TiO_2(s) + 6F^- + 4H^+ \rightarrow [TiF_6]^{2-} + 2H_2O \quad (8)$$

These two solvation mechanisms of the Ti^{4+} in the form of $[TiF_6]^{2-}$ complex ion prevent further formation of new oxide at the oxide/electrolyte interface and ensures a permanent chemical etching of the formed TiO_2 at a rate dependant on the F^- concentration[108]. As a result, an initial nanoporous structure on the surface is obtained[106]. Henceforward, chemical dissolution occurs faster at the pore bottoms, making them gradually deeper[109]. Another important factor that has to be mentioned is that the F^- ions are small and can therefore be transported through the oxide layer in competition with the migrating oxygen ions. Since the migration rate of the F^- ions is twice as high as for the oxygen species, an accumulation of the fluoride ions at the metal/oxide interface can be observed, leading to the formation of a fluoride-rich layer there[90,110]. Fig. 8 illustrates the transport processes that occur during this phase of anodization:

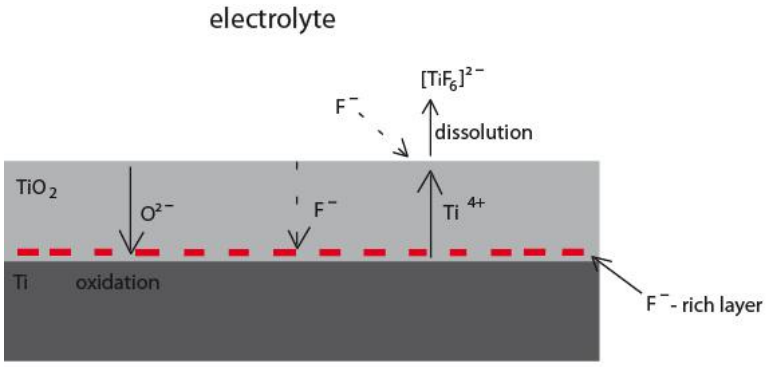

Fig. 8. Schematic representation of the transport processes in the presence of fluorides.

Finally, the transition from the initially formed nanoporous structure to the tubular structure takes place. It has to be noted here that, by the conversion of the titanium metal into the corresponding oxide, a volume expansion (Pilling-Bedworth ratio of 2.43) occurs that leads in combination with electrostrictive forces, originating from the high electric field intensity, to the generation of localized stress at the interface between metal and oxide. This stress induces a so-called plastic flow, which pushes the oxide material up the pore walls, so that newly formed oxide grows vertically from the surface of the metal. All this happens in such a way that the originally formed oxide layer at the oxide/electrolyte interface builds up now the inner-tube wall of the generated nanotube and the fluoride rich layer, that was initially located at the metal/oxide interface, can now be found at the outer

wall[106]. Additionally, further accumulation of fluoride ions at the cell boundaries between neighbouring tubes occurs, since the same flow also pushes the inward-migrating F^- ions towards these interfaces[90]. During the formation of these tubular structures the resulting tubes still stick together, containing a fluoride-rich layer between them and hence showing hexagonal shapes. But since this fluoride species, which can be found at the tube bottom and along the complete tube length, are sensitive to chemical dissolution, etching of the cell boundaries occurs, leading to the separation into individual tubes[106]. From now on the length of the formed nanotubes increases until a steady-state situation is achieved, where the growth rate of the tubes is identical to their dissolution rate[108]. All the stages from initiation to growth are summarized in Fig. 9:

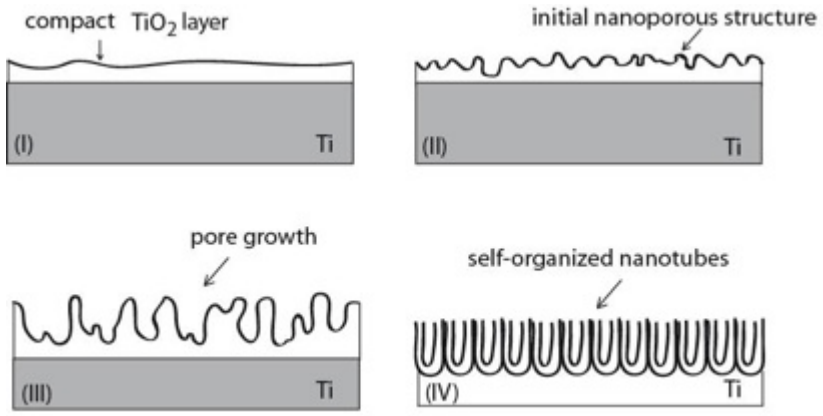

Fig. 9. Successive steps leading to the formation of the self-organized nanotubular structure.

The stages that are passed through during the anodization process can also be recognized and described on current-time characteristic curves as illustrated in Fig. 10. This curve can be divided into three regions, marked with I-III. In the first region (I) exponentially decay of the current occurs corresponding to the formation of the initial compact oxide layer. Afterwards (region II), the current increases again due to the generation of a nanoporous structure and their transformation into the nanotubular form, resulting in a larger active area and hence in an increased current. Finally, the progressive growth of the nanotubes can be seen in region III. Here the current is shared between the growing tubes, while the total electrochemical reaction front at the metal-oxide interface is constant, thus leading to a constant current value[106–108].

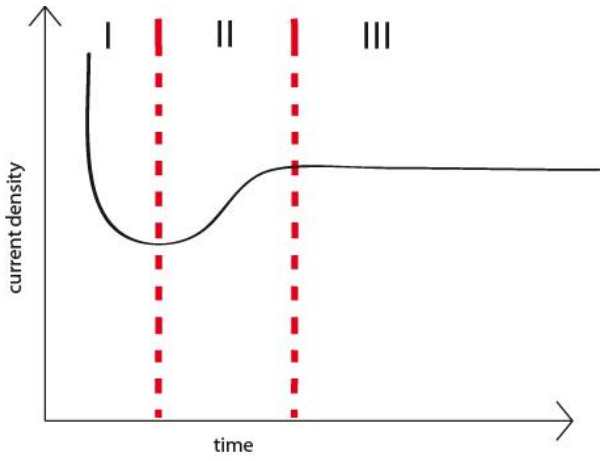

Fig. 10. Characteristic current-time curve for the anodization process.

2.2.3 Influence on Geometry, Morphology and Composition of the Tubes

The geometry and morphology of the formed TiO_2 nanotubes can be influenced by the anodization conditions including applied voltage, anodization time, fluoride concentration, used electrolyte and the water content[107]. The key factor that has an impact on the diameter of the tubes is the anodization voltage. A linearly diameter dependence on the applied potential can be observed[106]. This can be explained by the more intense etching of the oxide layer at higher voltages leading to larger pores in the nanoporous structure[111]. Another geometric feature that can also be affected by the applied voltage is the length of the nanotubes[107]. Since the growth of the oxide layer is determined by a high-field mechanism with a growth rate of 2-2.5 nm TiO_2/V, thicker nanotubular layers can be obtained, when higher potentials are applied[112]. However, at a constant voltage, the tube length is basically defined by the anodization time[107] for short to medium anodization durations. In the case of long-lasting anodizations, the maximum length of the tubes is limited and it is achieved, when the stationary state between TiO_2 electrochemical formation and its chemical dissolution is reached[90]. Furthermore, an inhomogeneous structure at the nanotube tops can be observed at extended times resulting from a more progressive etching of the tubes, as they are exposed to the fluoride containing electrolyte for a longer period of time. This inhomogeneous top structure is often referred to as “nanograss”[106]. However, some ways have been developed to prevent such extensive etching of the tube tops[91,113,114].

Depending on the concentration of fluorides in the electrolyte, different morphologies can be obtained on the titanium substrate. At low concentrations (≤ 0.05 wt%) a compact oxide film is formed, since insufficient F^- ions are present in the electrolyte and the

chemical dissolution of the formed oxide cannot be initiated. If the fluoride content is high (≈ 1 wt%), all of the formed Ti^{4+} is immediately solvated as $[TiF_6]^{2-}$ and thus no oxide layer is formed. Only for fluoride concentrations between these values nanotube formation takes place[90].

A dissimilar morphology and composition of the nanotubes can be observed during anodization in different electrolytes. Tubes that are formed in aqueous electrolytes show a non-uniform shape with sidewall ripples at the tubes and a length of only a few micrometers. This effect is related to the large amount of water contained in these electrolytes, since water accelerates the etching of the TiO_2 compared to its formation, resulting in shorter tubes and larger distances between the tube walls[106]. Furthermore, also a V-shaped morphology is obtained in aqueous electrolytes due to the permanently thinning of the tube tops[90]. On the contrary, anodization in organic viscous electrolytes[103], because of their low water content[115], leads to smooth tube walls as well as long tubes, as chemical dissolution is much slower in them[106]. The used electrolyte also influences the composition of the nanotubes, since the contained ions can be easily incorporated into the oxide of the tube walls[107]. As a result, an inner carbon-rich layer can be found, when organic electrolytes are used, while in aqueous electrolytes more hydroxides are found on the inner than on the outer tube wall[90].

2.2.4 Properties of the Nanotubes

TiO_2 nanotubes show several unique and outstanding properties making them very interesting for many applications. In the following section some relevant properties are addressed.

2.2.4.1 Crystallographic Structure

TiO_2 can naturally occur in three different crystalline phases, namely rutile, anatase and brookite. In addition, also an amorphous form can be obtained, when TiO_2 nanostructures are synthetized at room temperature using different methods, such as anodic oxidation or sol-gel techniques[90]. Moreover, some high-pressure titania polymorphs[116] and a synthetic phase, named $TiO_2(B)$[27,117], exist. Among all these crystal structures rutile presents the highest stability in the bulk phase, while anatase is considered to be thermodynamically most stable at nanoscale, because the lower surface energy of anatase determines a better phase stability in this range[90].

Regarding TiO_2 nanotubes, which are typically amorphous after electrochemical formation, a conversion into crystalline rutile and anatase phases can be observed, if the anodization is carried out at extended times or higher voltages[90,118,119]. The influence of the annealing process on the obtained crystallographic structure will be precisely outlined in 2.2.5.1[90].

2.2.4.2 Electrical and Optical Properties

Due to the amorphous TiO_2 nanotubes relatively wide band-gap of 3.2-3.5 eV[120–123], the electrical as well as the optical properties can be strongly influenced by present defects that create additional electronic states in the band-gap either near to the conduction band or the valence band. Particularly, the formation of Ti^{3+} species (e.g. during heat treatments in reducing atmosphere) near to the surface region plays an important role, as they can provide additional states close to the conduction band of TiO_2[90]. As a result, a high density of charge carriers (10^{18}-10^{19} cm^{-3})[124] can be achieved, a property that is responsible for the enhanced conductivity and higher photoresponse[90].

Compared to conventional TiO_2 nanoparticles, the transport of charge carriers is much lower in TiO_2 nanotubes due to the higher density of the above mentioned bulk states[90]. However, the diffusion length for electrons under UV illumination is 30 times higher in the nanotubes based on a reduced surface recombination probability[90,125].

Another optical feature that attract attention is the high refractive index of the nanotubes in the crystalline anatase (n= 2.5)[126] and rutile (n= 2.9)[126] form, making them very interesting for the creation of photonic meta-materials[90,127].

2.2.4.3 Reactivity

TiO_2 nanotubes show a relatively high reactivity that can be explained by their high surface area, the directionality of the tubes, the presence and high density of structural and electronic defects and the possibility to stabilize particular crystal phases and orientations[90]. Hitherto, high activity toward CO_2, CO, H_2 and alkane adsorption has been demonstrated[90]; recently, it also has been shown that adsorption of oxygen[128], a requirement for many surface reactions, on crystalline anatase TiO_2 nanotubular layers may be possible – a remarkable attribute not observed on other pure crystalline rutile and anatase materials until now[108].

One important reactivity feature related to electrochemistry is the ability of titania nanotubes to insert small cations, when an external reduction potential is applied, a process occurring simultaneously with the reduction of Ti^{4+} to Ti^{3+} in the TiO_2 lattice [Eq. (9)][90].

$Ti^{4+}O_2 + e^- + Y^+ \rightarrow Ti^{3+}O_2Y$ (9)

(Y= H^+, Li^+, Na^+)

Since the formation of Ti^{3+} leads to additional electronic states in the band-gap, as already mentioned in section 2.2.4.2, changes in optical properties and conductivity can be observed, such as the blackening of the tubes. Given that this process is reversible, TiO_2 nanotubes can be exploited for applications in the field of electrochromic devices and rechargeable batteries[108].

The TiO_2 nanotubular system also proves beneficial, when it is used as substrate in noble metal catalysis. On one hand the nanotubular structure can prevent aggregation of the catalyst on the surface leading to higher specific reaction rates and reactivity, accompanied with a reduced loading of the expensive catalyst, while on the other hand, a high overpotential for the O_2 evolution reaction can be induced thus bringing forth more facile and faster catalytic reactions[90].

2.2.5 Modification of the Nanotube Properties

Modifications are necessary to adapt the TiO_2 nanotubes for various applications that depend on specific chemical, optical and electronic properties. This can be done by (i) annealing, (ii) doping, (iii) filling and decoration and (iv) attachment of monolayers[90].

2.2.5.1 Annealing

TiO_2 nanotubes are typically amorphous after electrochemical formation, but conversion into anatase or rutile can be achieved via heat treatments either under oxidizing (O_2 or air) or reducing (N_2 or Ar) conditions[104,129,130]. When annealed at lower temperatures (< 350 °C), the transition from the amorphous to the crystalline anatase phase takes place[131], since anatase is thermodynamically more stable due to its lower surface energy in this temperature range[129]. However, the temperature at which the phase transformation starts, also depends on the used annealing atmosphere. While under oxidizing conditions anatase is already present at 250 °C, transition into anatase is much slower in argon or nitrogen[131]. With further increasing annealing temperature the crystalline rutile phase starts to form, with the result that the TiO_2 nanotubes are completely converted into rutile at 900 °C. It is interesting to say that at higher temperatures also thermal oxidation of the titanium substrate underneath the tubes can appear, resulting in a thin rutile layer there. This thermal oxide layer is the thicker, the more oxidizing the atmosphere and the higher the annealing temperature is[90]. Furthermore, when annealed at temperatures > 450 °C, cracks in the tube walls start to emerge caused by stress occurring during annealing. Both

effects, the rutile layer as well as the cracks have a negative impact on the conductivity of the tubes, when annealed above 450 °C, since cracks result in larger diffusion lengths and also rutile shows lower electron mobility than the crystalline anatase phase[130]. It should be noted that annealing time and heating rate also have an influence on the resulting crystal structure. For long-standing annealing processes, collapsing of the tubes can be observed, for instance when they are heated above 650 °C[90].

Fluoride and carbon species as well as hydroxide groups, that are incorporated into the tube wall during anodization, can also be driven out to an amount < 1% by annealing. Since fluoride ions are corrosive, toxic and have a detrimental impact on optical and electronic properties, their elimination positively influences the properties[129].

In conclusion, one can say that annealing processes at lower temperatures are carried out to improve conductivity and enhance the optical features, since anatase is more conductive than the amorphous phase and annealing introduces additional states in the band-gap that are necessary for an adequate photoresponse[90].

2.2.5.2 Doping

Due to its wide band-gap of approx. 3.2 V, TiO_2 can only absorb UV light[90] and thus its direct application in the field of solar energy is limited[107]. Therefore, additional species that are electronically active - so-called dopants - have to be introduced in the structure to decrease the band-gap, resulting in a considerable response to visible light. Several methods have been developed to get doped TiO_2 nanotubes, amongst others (i) ion implantation, (ii) thermal treatment in an atmosphere containing the doping species as a gas, (iii) using an alloy as a substrate for anodic oxidation of the nanotubes and (iv) treatment of the tubes in a melt/solution of the dopants[90].

At the moment, nitrogen proves to be the best dopant for TiO_2 nanotubular structures, since it decreases the band-gap by introducing an additional state near to the valence band. However, some more elements such as Cr, Mn, Fe, V or C and S have been explored as possible doping species[90].

2.2.5.3 Filling and Decorating

Filling and decoration of the TiO_2 nanotubes with a secondary material such as metals, polymers or semiconductors, result in tubes with enhanced or rather additional properties. For example, deposition of TiO_2 nanoparticles outside the tube wall improves efficiency of solar cells due to the increased surface area, while Fe_3O_4 deposited into the tubes introduces additional magnetic properties. Generally, modification by filling and decoration can have the following beneficial effects: (i) improved charge transfer due to surface plasmon effects, (ii) introduction of suitable states in the band-gap to simplify charge

injection and (iii) catalysis for charge-transfer reactions[90]. At the moment, electrodeposition seems to be an adapted method to decorate or fill TiO_2 nanotubes[132].

2.2.5.4 Attachment of Monolayers

A condensation reaction between the hydroxyl groups on the TiO_2 surface and silanes, phosphonates or carboxylates leads to a covalent attachment of these groups on the surface. This is done (i) to get biochemical and chemical sensors, (ii) to obtain modified biocompatibility and (iii) to change the wettability of the surface[90].

2.2.6 Used Methods and Techniques

2.2.6.1 Cyclic Voltammetry (CV)

Cyclic voltammetry is a versatile and convenient electroanalytic method to gain qualitative information about electrochemical reactions including electron-transfer reactions, redox and adsorption processes. For instance, the transfer coefficient, the rate constant as well as the location of the redox potential can be determined using this technique[133]. Generally, the CV consists of scanning the potential, applied to the WE, with a constant scan rate from an initial value E_1 to a defined limit E_2 (switching potential), where the scan is reversed, sweeping back the potential to the value of E_1 (see Fig. 11)[134]. This potential sweep can be done once or repeated many times. The scan rate as well as the values for the initial and switching potential can be varied after each cycle. It is also possible to apply a delay at the vertex potentials, include open-circuit periods etc[135]. The current response to the applied voltage is obtained and recorded. This can be displayed in a so-called cyclic voltammogram[133].

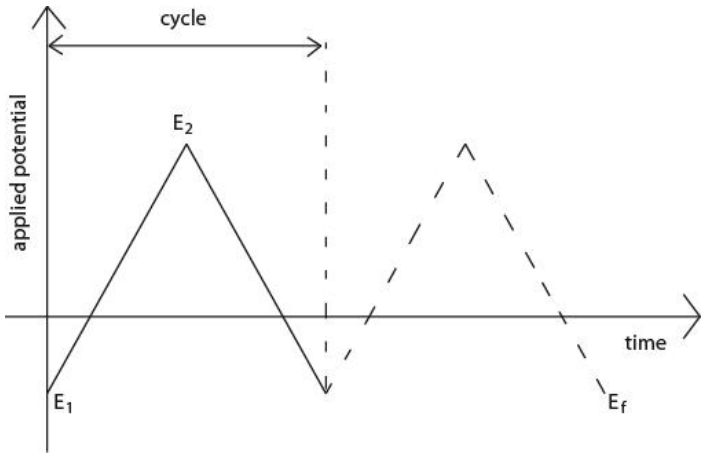

Fig. 11. Potential as a function of time for a CV experiment.

2.2.6.2 Galvanostatic Cycling with Potential Limitation (GCPL)

Galvanostatic cycling with potential limitation represents a technique used to investigate the behaviour of a battery electrode during the intercalation/de-intercalation process. The experiment is carried out by applying a constant current (expressed as current intensity per mass of active material (mA/g) or using the C-rate convention) within predetermined potential range limits. The charge or the discharge of the material takes place alternately depending on the sign of the imposed current[133]. The current is switched from oxidizing to reducing current and vice-versa upon reaching the pre-set potential limits and this cycle can be repeated many times. This technique provides information about the specific capacities of electrode materials, their initial and subsequent irreversible capacities as well as the capacity fading during long term cycling or over a large number of cycles. Also, useful information about the insertion/de-insertion overpotentials at various kinetic rates (determined by the value of the applied current) can easily be obtained by observing the polarization effects during charge and discharge.

2.2.6.3 Chronoamperometry (CA)

Chronoamperometry is an electrochemical method that measures the current response of an electrochemical system, when a potential pulse is applied. CA is carried out by changing the potential of the WE from an initial value E_i to a potential E_1, at which a faradaic process (charge transfer through the electrified interface) takes place, and holding this value for a period of time t_1 [136]. In addition to this single potential step, the potential can also be returned to a final potential E_f followed by a time period t_2, resulting in a double potential step experiment (Fig. 12, left side). The resulting current is recorded as a function of time (Fig. 12, right side)[137].

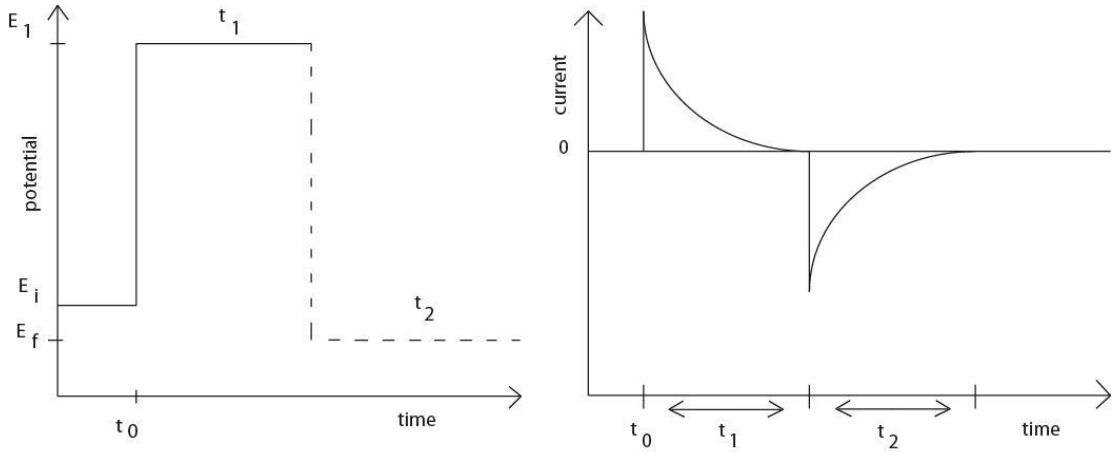

Fig. 12. (left) Potential and (right) current as a function of time for a CA experiment.

In the first few ms of the experiment the capacitive current[137], that represents only the charge/discharge behaviour of the electrode's electrical double layer without involving any chemical reactions there, is the dominant phenomenon[136], resulting in a current decay with 1/t dependence[137]. On the other hand, at longer times the faradaic current, that results from charge-transfer reactions at the surface of the electrode, prevails. The current–time dependence in this region can be described using the Cottrell equation[136],

$$i = \frac{nFAc_0\sqrt{D_0}}{\sqrt{\pi t}} \qquad (1)$$

where n is the number of electrons transferred, F is the Faraday's constant (96485 C/mol), A is the electrode area (cm^2), c_0 is the concentration of the electroactive species (mol/m^3), D_0 is the diffusion coefficient (cm^2/s) and t is the time (s)[137]. As a result, the current decays in diffusion controlled processes as a function of $t^{-1/2}$ in this region[136].

By using this relation it is possible to determine either the diffusion coefficient (from the slope of i versus $t^{-1/2}$)[136] of electroactive species or the electrode surface area, when the other parameters are known[137]. Chronoamperometry can also be used to study mechanisms of electrode processes.

2.2.6.4 Electrochemical Impedance Spectroscopy (EIS)

Electrochemical impedance spectroscopy is a powerful tool for the characterization of electrochemical systems. Information can be obtained about electrode-electrolyte interfaces, their structure and the electrochemical reactions taking place there. This technique measures the impedance (Z) of an electrochemical cell by applying a sinusoidal ac (alternating current) perturbation at the working electrode, usually in the form of an alternating potential and analysing the ac current response as a Fourier series. Since electrochemical impedance is normally carried out at small ac signals, a pseudo-linear response is obtained, meaning that the resulting current is also sinusoidal with similar frequency, but phase shifted[138].

The applied potential signal has the general form

$$E_t = E_0 \sin(\omega t) \qquad (2)$$

where t is the time, ω represents the radial frequency, E_0 is the amplitude and E_t is the potential at t[138].

The resulting current signal I_t is phase shifted (ϕ) and has a maximum amplitude I_0[138].

$$I_t = I_0 \sin(\omega t + \phi) \tag{3}$$

When now an expression similar to the Ohm's law is used, the impedance (Z) can be expressed as:

$$Z = \frac{E_t}{I_t} = Z_0 \frac{\sin(\omega t)}{\sin(\omega t + \phi)} \tag{4}$$

where Z_0 represents the magnitude[138].
With the Euler's relationship,

$$\exp(j\phi) = cos\phi + jsin\phi \tag{5}$$

the impedance can then be represented as a complex function consisting of a real and an imaginary part[138]:

$$Z(\omega) = \frac{E_t}{I_t} = \frac{E_0 \exp(j\omega t)}{I_0 \exp(j\omega t + \phi)} = Z_0(cos\phi + jsin\phi) \tag{6}$$

Impedance data are often graphically presented in the so-called Nyquist and Bode plots[139]. While in the Nyquist plots the imaginary part is plotted versus the real part of the impedance, the Bode plot shows the modulus of the impedance as a function of the log frequency[138]. The Nyquist representation has the great advantage that the shape of the resulting curves delivers insight into possible mechanisms, although no information about the frequency is shown[139]. On the contrary, in the Bode plots the frequency dependence is clear and immediately visible[138]. Therefore, in practice, both plots are used.
To evaluate the processes and electrochemical phenomena taking place at the working electrode, electrical equivalent circuits are usually used to model the impedance response of the electrode being investigated. This is done by constructing at first an electrical circuit composed of elements such as ideal resistors (R), capacitors (C) and inductors (L)[139] connected in series or in parallel, since, in most cases, the EIS data cannot be fitted using a single circuit element[139]. In order to account for real systems that mostly do not behave like common RLC circuit elements, special virtual circuit elements such as the constant phase element (CPE) and the Warburg element (Z_w) can also be introduced. In such an equivalent circuit model, the resistor may for instance represent the resistance to charge

transport, a capacitor may model the ideal behaviour of an electrical double layer, while an inductor may model adsorption and desorption at the electrode surface as well as the formation of a passivation layer[139]. The Warburg element is used to depict diffusion or mass transport at the electrode. After choosing a suitable equivalent circuit that can account for the physical and chemical phenomena taking place in the electrochemical cell, the impedance response data is fitted to this circuit in order to determine the specific parameters associated with the circuit elements used. With a validated equivalent circuit, information about the resistance of the electrolyte, the capacitance of the double layer, the diffusion coefficient of electroactive species etc. can be determined.

2.2.6.5 X-Ray Diffraction (XRD)

XRD analysis is a powerful nondestructive method to obtain information about crystalline materials including phases, structures, and crystal orientations as well as other structural parameters such as crystallinity, amorphicity, crystallite size and crystal defects. Since crystalline solids are built up of planes of atoms that are separated by a distance d, diffraction of incident x-rays in specific angles at each set of atomic planes can occur[140]. As a result an x-ray diffraction pattern is obtained that is specific for each crystalline material and can therefore be used as fingerprint for its characterization.

3 Experimental Part

3.1 Formation, Modification and Characterization of TiO_2 Nanotubes

3.1.1 Synthesis of the Tubes by Anodic Oxidation

Titanium foils (Sigma Aldrich) with a thickness of 0.25 mm and a purity of 99.7% were used as substrates for the anodic growth of the TiO_2 nanotubes. These foils were cut into small square pieces of 12.5 mm x 12.5 mm and ultrasonically cleaned in acetone, isopropanol and methanol, in this order, for 10 minutes, in each of the above-mentioned solvents. Subsequently, these samples were rinsed with distilled water and dried with compressed air.

For anodization, an electrochemical cell in a two-electrode configuration having the titanium foil as working electrode and a stainless steel plate as counter electrode was used (Fig. 13). In this cell, the sample was pressed against a copper or brass ring to ensure a good electrical contact, while leaving a surface area of approx. 0.708 cm^2 of the titanium exposed to the anodization bath, which consisted of 0.4% NH_4F, 2% distilled water and 97.6% ethylene glycol. In order to dissolve the ammonium fluoride crystals completely in the ethylene glycol/water mixture, the solution was stirred over night before used.

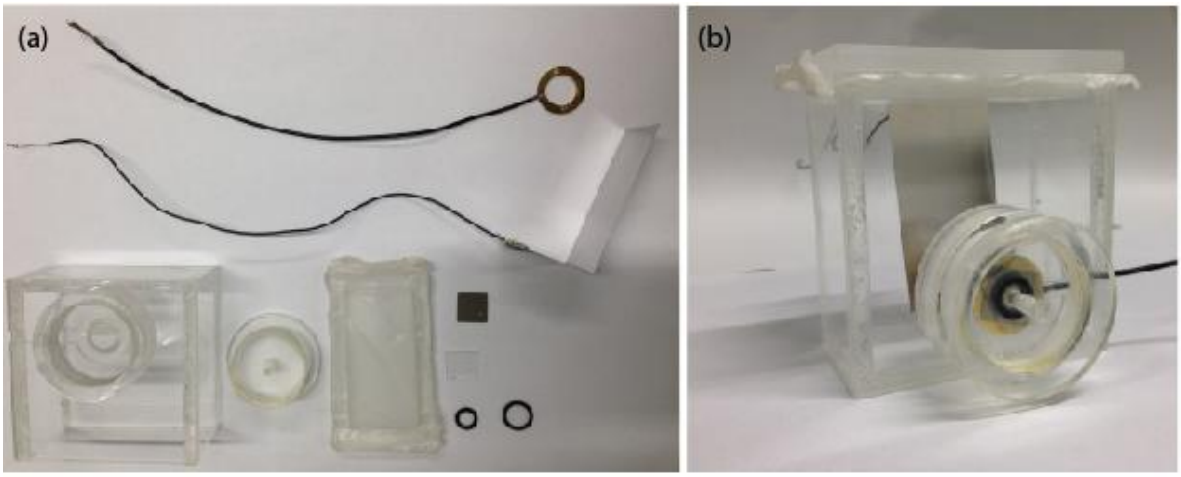

Fig. 13. Photographs of the electrochemical cell in a two-electrode configuration used for anodization with the titanium foil as working electrode and a stainless steel plate as counter electrode. (a) Components needed for the assembling of the cell. (b) Assembled electrochemical cell.

For the experiments the cell was connected to a precision dc power supply (Agilent E3610A) and anodization was carried out at several constant potentials (30, 40, 50 and 60 V) and for various time intervals (30 min, 1 h and 2 h). After the anodization step, various cleaning procedures were used on the as-anodized samples depending on the applied voltage. Those anodized at 50 and 60 V were only rinsed with distilled water followed by carefully drying with compressed air, while the samples anodized at 30 V were cleaned following one of the two treatments explained below. They are either rinsed with distilled water and EtOH alternately and then dried with compressed air; this cleaning method was denoted as A1. Or, they were first rinsed with distilled water and dried with compressed air and then, after a waiting time of 20 min, ultrasonically cleaned in distilled water for 15 sec and dried again. This is described as cleaning procedure A2. The samples prepared at 40 V were subjected to one of the five following treatments. Method one (B1) corresponds to the cleaning applied to the samples anodized at 50 or 60 V. Cleaning technique B2 is similar to B1, however rinsing was carried out with distilled water and EtOH alternately before drying. For the third approach (B3), the samples were first rinsed with distilled water and EtOH alternately and dried with compressed air and then, after 20 minutes, ultrasonically cleaned in distilled water for 15 seconds and dried again with compressed air. In the fourth method (B4) compared to B3, rinsing was carried out only with water and the subsequent cleaning in the ultrasonic bath was extended to one minute. For the last approach (B5) the anodized samples were rinsed with distilled water, then immersed in EtOH for one hour and finally dried on air. All the cleaning methods mentioned above are summarized in Table 1.

Table 1. Cleaning procedures used for the samples after anodization depending on the applied voltage.

anodization voltage	cleaning treatment after anodization
30 V	**treatment A1:** 1. rinsing with distilled water 2. drying with compressed air 3. waiting for 20 minutes 4. ultrasonically cleaning in distilled water for 15 seconds 5. drying with compressed air **treatment A2:** 1. rinsing with distilled water/EtOH alternately 2. drying with compressed air

40 V	**treatment B1:** 1. rinsing with distilled water 2. drying with compressed air **treatment B2:** 1. rinsing with distilled water/EtOH alternately 2. drying with compressed air **treatment B3:** 1. rinsing with distilled water /EtOH alternately 2. drying with compressed air again 3. waiting for 20 minutes 4. ultrasonically cleaning in distilled water for 15 seconds 5. drying with compressed air again **treatment B4:** 1. rinsing with distilled water 2. drying with compressed air 3. waiting for 20 minutes 4. ultrasonically cleaning for 1 minute 5. drying with compressed air **treatment B5:** 1. rinsing with distilled water 2. immersing in EtOH for 1 h 3. drying on air
50 V and 60 V	1. rinsing with distilled water 2. drying with compressed air

Furthermore, also a two-step anodization mechanism was accomplished. For this, one titanium sample was anodic treated at 40 V for 2 hours and cleaned by rinsing with water and drying with compressed air. Then, the nanotube layer on the surface was removed using an adhesive scotch tape (see section 3.1.2.) and the same titanium foil, after ultrasonically cleaning in acetone, isopropanol and methanol for 10 minutes, was anodized again, in the same conditions. Finally, the as-prepared samples were rinsed with distilled water and dried with compressed air. All the experiments were carried out at room temperature at approximately 24 (±1) °C.

3.1.2 Mass Determination of the Nanotube Layers

The anodized samples used for mass determination were just cleaned by rinsing with water and drying with compressed air. A scotch tape from 3M was employed to determine the mass of the nanotubes on the surface. The procedure was as follows: In the first step a small piece of the scotch tape was weighed out using a microbalance. Then the adhesive side of the tape was pressed onto the surface of the anodized titanium foil. Finally, the adhesive strip was peeled off from the surface and with the nanotube layer sticking on it, weighted again. The whole procedure is graphically illustrated in Fig. 14. However, mass determination has to be carried out directly after drying, otherwise it is not possible to remove the nanotube layer.

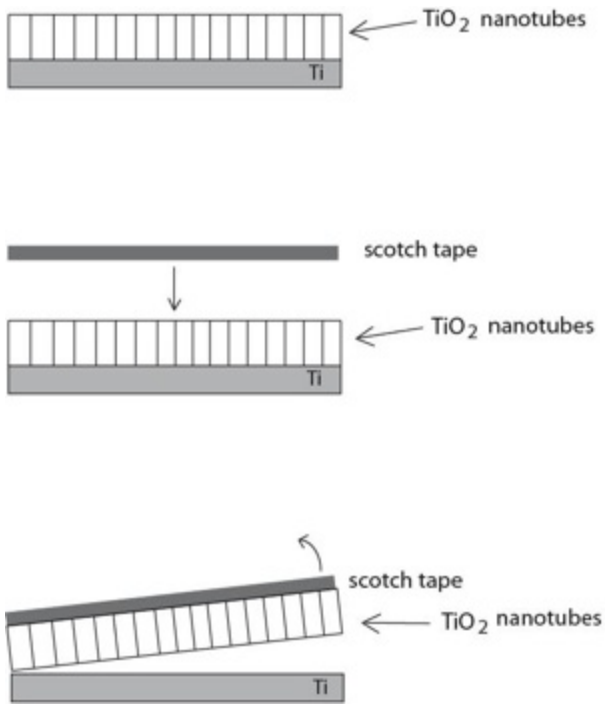

F**ig. 14.** Schematical representation of the mass determination using a scotch tape. First, a small piece of a scotch tape was weighted. Then, this tape was pressed with its adhesive side on the nanotube layer. Finally, the scotch tape with the nanotube layer on it was peeled off from the surface of the titanium foil and weighted again.

3.1.3 Heat Treatment of the "as-grown" Nanotubes

To study the influence of heat treatments on the structure of the as-anodized samples, annealing was carried out in a horizontal pipe furnace at different temperatures (100 °C, 200 °C, 300 °C and 350 °C) for 1 hour or 2 hours either in air or under argon flow with a heating rate of 5 °C/min. For the experiments done in argon the furnace was first evacuated for about 30 minutes and then streamed with argon gas to obtain a pure atmosphere for the subsequent annealing process.

3.1.4 Structural and Morphological Characterization

Scanning electron microscopy (Oxford Instruments, INCA X-act PentaFET Precision TESCAN) was employed for the morphological characterization of the pristine TiO_2 nanotubes. In order to obtain cross-sectional and bottom-view images of the nanotube layers, samples were scratched at the surface prior to characterization.
To examine the amorphous or crystalline nature of the as-anodized as well as the annealed samples, x-ray diffraction analysis was performed. For the heat-treated ones, XRD measurements were done after each annealing temperature.

3.2 Pouch Cells

3.2.1 Assembling of Pouch Cells

In order to study the electrochemical performance of the anodized TiO_2 nanotubes as negative electrode material in sodium-ion batteries, they were assembled in so-called pouch cells.
For the set-up of such a cell, the following components were required:

- A rectangular piece of a pouch foil (approximately 10.5 mm x 4.5 mm)
- Square pieces of a sealing material (six units per cell)
- Two pieces of a separator material (Freudenberg FS 2190)
- Copper foil (Goodfellow, 0.0175 mm thick, purity 99.9%), cut into a L-shape used as current collector for the counter electrode
- Two stripes of the same copper foil needed to wire the working and the reference electrode

All the above-mentioned components are graphically shown in Fig. 15 (a) and (b).

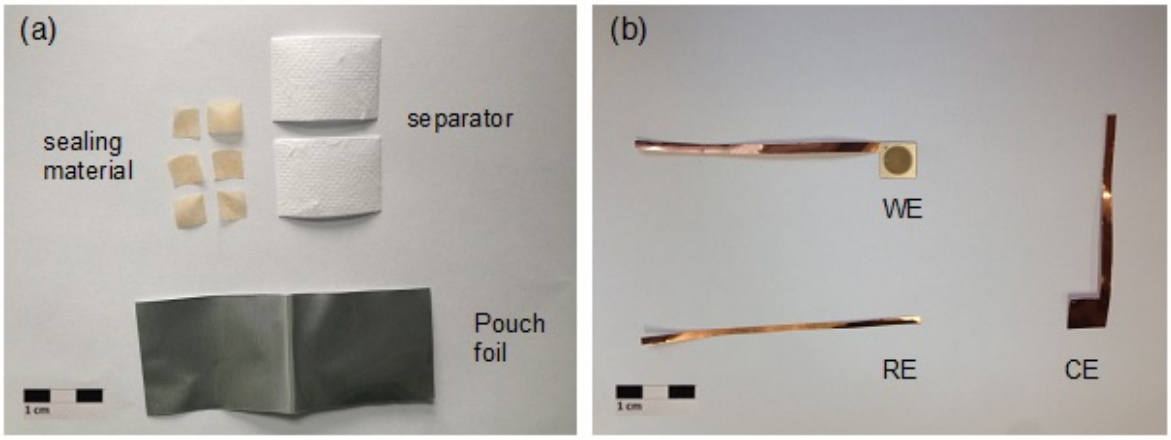

Fig. 15. Components needed for assembling of pouch cells.

First, spot-welding was performed to contact the electrochemical treated titanium sample with the copper current collector. Afterwards, the cut pouch foil was folded in half, creating a pocket, in which the working electrode (WE, titania nanotube sample supported onto titanium foil) was embedded and fixed by heat-sealing of the top. A special sealing material was used at the hot-seal level in order to avoid a short-circuit of the current collectors through the pouch metallic foil. After this, the two pieces of separator were placed above the working electrode in the cell. The pre-assembled cell as well as the current collectors for the counter and the reference electrodes were dried in a Büchi oven at 60 °C under vacuum over night. Further assembling was carried out in a glove box under argon atmosphere with O_2 and H_2O vapour concentrations lower than 1 ppm. For the preparation of Na counter electrode (CE), a small piece of Na metal was put on the L-shaped copper current collector and rolled between two sheets of transparent Mylar film until the Na was spread over the entire Cu current collector surface. Excess Na metal, which was protruding over the edges of the current collector, was cut away. For the reference electrode, a small piece of sodium was placed at the end of the copper stripe and fixed by folding the stripe onto the Na metal. Then, the Na-loaded CE was directly positioned above the WE and the separator in the cell, while the RE was placed between the two sheets of separator next to the counter and the working electrode. In order to fix their position, hot-sealing was also performed on the bottom side. The separator was then soaked with approximately 600µl of the electrolyte solution (either 1 M $NaClO_4$ in PC or 0.6 M $NaPF_6$ in an EC:DMC 3:7 mixture) using an automatic pipette and closed by hot-sealing of the last side. A schematic representation of the stacking of the individual components can be seen in Fig. 16.

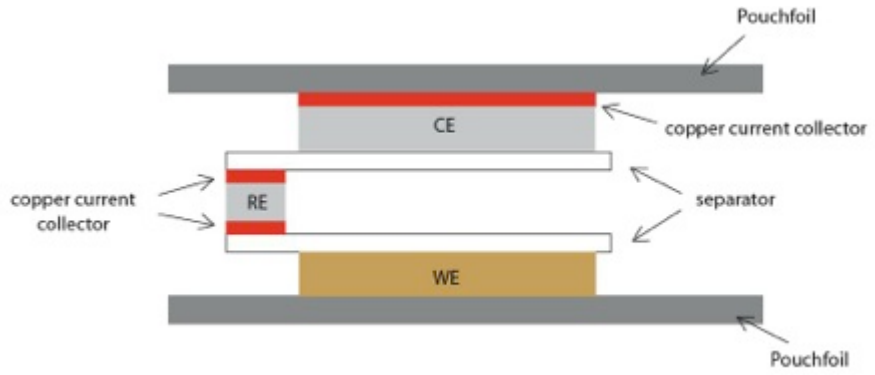

Fig. 16. Stacking of the individual components in the Pouch cell.

Finally, in order to get a good contact between the electrodes, the cell was opened by cutting one edge away, evacuated for 20 seconds and sealed again. This last step was performed outside the glove box. All steps of the above-mentioned assembling process are graphically summarized in Fig. 17. Prior to electrochemical characterization, the as-prepared pouch cell was tested for short-circuits and the cell voltage was measured using a digital multimeter (Fluke 87).

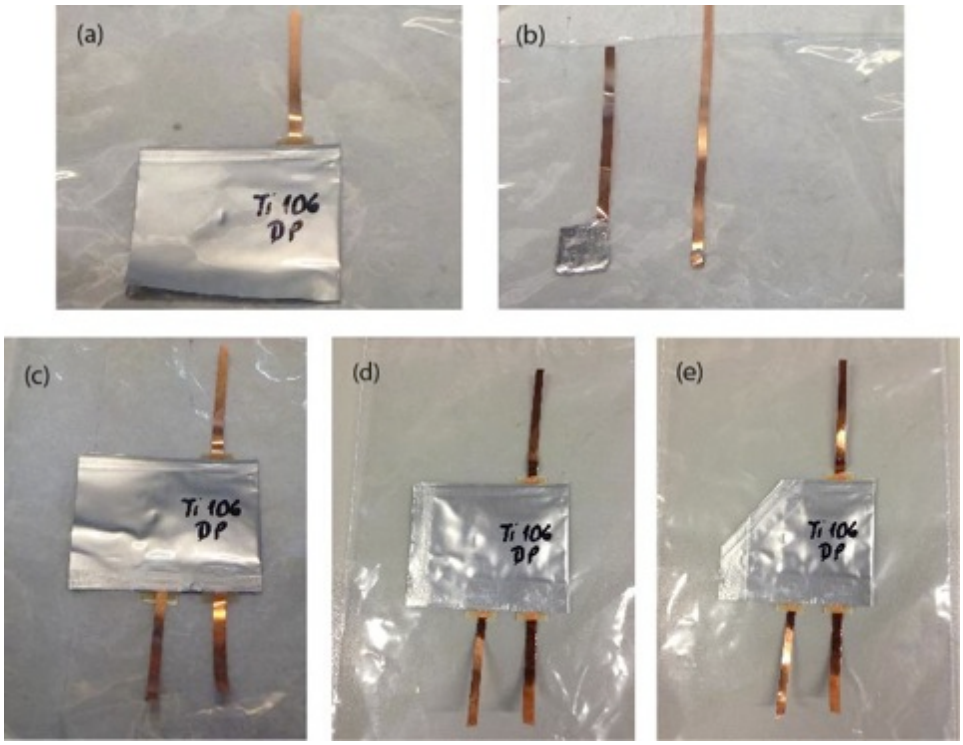

Fig. 17. Steps for assembling of a pouch cell. (a) Placing of the WE and the separator into the pouch foil and heat-sealing of the top side. (b) Putting cleaned sodium metal on the current collector of the RE and CE (c) Placing of the counter and reference electrode into the cell and heat-sealing of the bottom side. (d) Filling with electrolyte and heat-sealing of the last side. (e) Opening the cell by cutting one edge away, evacuating the cell and sealing it.

3.2.2 Electrochemical Characterization

Electrochemical measurements of the pouch cells were performed directly after assembling of the cells. Cycling voltammetry as well as galvanostatic cycling was carried out utilizing a multichannel MPG-2 potentiostat from Biologic Science Instruments (Software EC-LAB VIO-34). For the cycling studies the GCPL-technique (Galvanostatic Cycling with Potential Limitation) was selected. The charge/discharge experiments were always started with a resting time of 12 hours followed by cycling primarily at 50 mA/g for 100 times continued at 25 mA/g for 100 or rather 200 times. The potential limits were set either between 0.8-2 V vs. Na^+/Na or 0.1-2 V vs. Na^+/Na. To obtain information about the capacity retention and evaluate the self-discharge characteristic of the titania nanotubes, another cycling experiment was performed. For that purpose, the pouch cell, after a resting time of 12 hours, was cycled at 25 mA/g for 10 times followed by doing a half cycle in order to reach the charged state and resting at this state for 6 hours. After this resting step, the cell was charged again and the cycle was completed by subsequently discharging. This procedure was repeated several times, however the resting time was extended to 12, 24, 48, 120 and 240 hours, namely in this order. Between the last three resting steps cycling was only done for five times. The potentials were set between 0.8-2 V vs. Na^+/Na in this experiment. The capacity retention determination was carried out on one cell that had already been cycled for 300 times with the former mentioned program and on one freshly assembled cell.

For the cyclic voltammetry experiments the CVA technique (Cyclic Voltammetry Advanced) was selected. After a resting time of 12 hours, the potential of the working electrode was scanned between 0.1-2 V at different scan rates (0.05, 0.1, 0.2, 0.5, 1, 2, 5 and 10 mV/s). The initial E_i and the final potential E_f were set to 1.5 V. For each scan rate, two cycles were acquired.

3.2.3 Compositional, Structural and Morphological Characterization

The galvanostatic cycled samples had to be cleaned prior to characterization. This was done by cutting the pouch cell open in the glovebox (Ar atmosphere with an O_2 and H_2O concentration smaller than 1 ppm) and by removing the cycled samples from the other cell components. The nanotubes on the titanium foil were then rinsed with propylene carbonate several times and immersed in PC for 15 minutes. This cleaning step was repeated twice. For the final rinsing diethyl carbonate was used.

X-ray diffraction experiments were carried out to determine the crystallinity of the cycled samples. The composition and the morphology of the nanotube layers were obtained

using a scanning electron microscope equipped with an EDX-detector (ZEISS Ultra 55). SEM cross-section images were taken from samples that were intentionally scratched just before placing the sample into the SEM vacuum chamber.

3.3 Swagelok Cells

3.3.1 Analysis of Electrolytes Additives on Passive Layer Formation using EIS

Two-electrode symmetrical Swagelok cells with sodium metal as both working and counter electrode separated by two disks of Whatman GF/B glass fibers were assembled in a glovebox under argon atmosphere with an O_2 and H_2O concentration smaller than 1 ppm. A set-up of such a Swagelok cell as well as a finally assembled one are graphically outlined in Fig. 18.

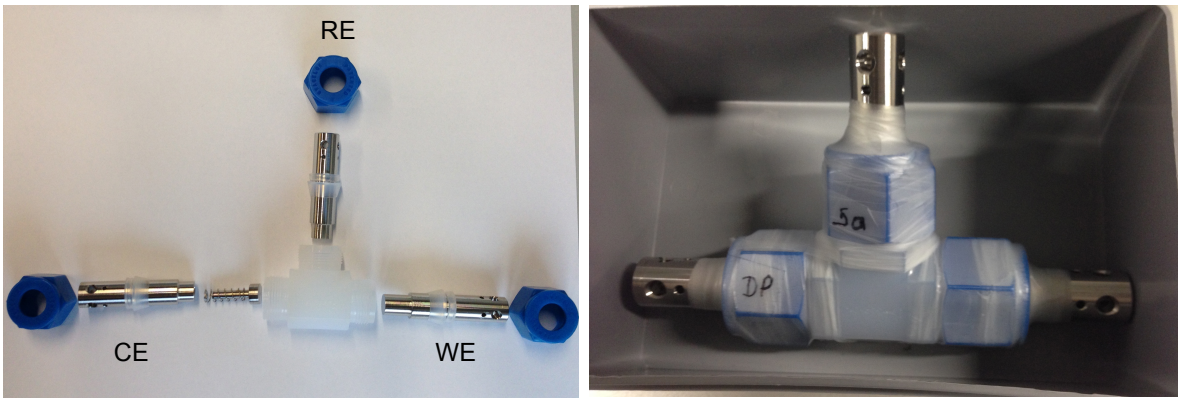

Fig. 18. Photographs of the cell parts as well as a finally assembled three-electrode Swagelok cell. In this case only the CE and WE is used. The third connection just serves as a closing plug.

For the first experiment, a 1 M solution of $NaClO_4$ in propylene carbonate as well as a 0.6 M solution of $NaPF_6$ in a mixture of EC:DMC (3:7 by wt%) were used as electrolytes, filling each cell with 800 µl of the respective electrolyte solution. In order to study the influence of additives on the formation of a passivation layer on the Na metal, the $NaClO_4$ as well as the $NaPF_6$ based electrolyte were mixed with 1% of one of the following additives: vinyl carbonate, fluoroethylene carbonate, 4-fluorophenyl isocyanate, 2,3,4-trifluorophenyl isocyanate and 4-vinyl-1,3-dioxolan-2 one. For each electrolyte/additive combination one Swagelok cell was prepared adding 800 µl of the respective solution.

Potentiostatic EIS measurements were carried out at 20 minutes, 1 hour, 3 hours, 10 hours, 1 day, 2 days, 3 days, 4 days and 5 days after preparation using the Parstat MC

potentiostat (Software: Versa Studio). For the experiments done at 20 minutes and 1 hour after assembling, the frequency range was set from 500000 to 0.1 Hz with an amplitude of 20 mV. For the further measurements the frequency range was extended to 0.01 Hz using the same value for the amplitude.

3.3.2 Determination of the Diffusion Coefficient

Swagelok cells in a three-electrode configuration with sodium metal as counter and reference electrode were assembled in a glovebox under argon atmosphere with an O_2 and H_2O concentration smaller than 1 ppm. For the experiment a copper disk (Goodfellow, thickness: 0.0175 mm, purity: 99.9%) was used as working electrode. Prior to assembly, the copper disk was cleaned by sonication in acetone, isopropanol and methanol for ten minutes followed by rinsing with distilled water and carefully drying with compressed air. The cell was filled with 800 μl of a 1 M solution of $NaClO_4$ in PC and two Whatman GF/B separator disks were placed between the counter and the working electrode. Additionally, a third separator was sided above the WE-CE stack.
Chronoamperometry was carried out utilizing a multichannel MPG-2 potentiostat from Biologic Science Instruments (Software EC-LAB VIO-34). For the CA studies a potential of -0.1 V versus reference electrode was applied in one step for 20 seconds.

3.4 Sn/TiO_2 Composites

3.4.1 Preparation of Sn-filled Nanotubes using Electrodeposition

Nanotubes grown by anodic oxidation at 40 V for 2 hours using the procedure described in section 3.1.1. were employed in the electrodeposition process. After anodization the samples were rinsed with distilled water, dried with compressed air and then, after 20 minutes, ultrasonically cleaned in distilled water for 15 seconds and finally dried with compressed air again. In order to carry out electrodeposition, the as-cleaned samples were fit in an electrochemical cell (the same one that was already used for the anodization process) so that the whole nanotube layer was exposed to the solutions used for Sn electrodeposition. This time a platinum gauze served as counter electrode and a calomel electrode (SCE) as reference. All experimental steps were performed using the Parstat MC potentiostat (Software: Versa Studio). Different approaches were explored in order to get the nanotubes filled with Sn.
In the first experiment, filling of the tubes was attempted in the following way: Primarily reduction of the nanotubes was carried out in 1 M $(NH_4)_2SO_4$ by applying a potential of

-1.5 V versus SCE. After this, the sample was immersed with several drops of a diluted $SnCl_2$ sensitizer solution (0.85 g $SnCl_2$ in 200 ml distilled H_2O) for 5 minutes and then rinsed with distilled water. Subsequently, the nanotubes were soaked in an initiator solution (0.7 g $AgNO_3$ in 50 ml distilled H_2O) for 5 minutes and washed with distilled water. Finally, Sn electrodeposition was carried out using a pulsing approach with a cathodic current pulse (-10 mA/cm^2 for 100 ms) followed by an anodic pulse (+1 mA/cm^2 for 10 ms) and a resting time (0 mA/cm^2 for 3 sec) in a $SnCl_2$/sodium citrate solution. The electrodeposition solution was prepared by mixing a $SnCl_2$ (3.5 g $SnCl_2$ in 100 ml distilled H_2O) and a sodium citrate solution (0.5 M in 100 ml distilled water). The above-mentioned pulsing approach is repeated 300 times. Afterwards, the sample was rinsed with distilled water and carefully dried with compressed air.

The second experiment was performed in the same way, however the $SnCl_2$/sodium citrate solution was stirred at 500 rpm during the Sn electrodeposition step.

In the third approach, filling of the nanotubes was carried out without soaking the sample in the initiator solution.

In the fourth experiment the pulsed Sn electrodeposition step was directly applied after the reduction step. No sensitizer and initiation solution was used in this approach.

All experiments were carried out under room temperature at approximately 24 (±1) °C.

3.4.2 Morphological Characterization

Scanning electron microscopy (Oxford Instruments, INCA X-act PentaFET Precision TESCAN) was employed for the morphological characterization of the TiO_2 nanotubes that were subjected to the electrodeposition process. In order to obtain cross-sectional and bottom-view images of the nanotube layers, samples were scratched at the surface prior to characterization.

3.4.3 Electrochemical Characterization

To study the cycling behaviour of the modified TiO_2 nanotubes as negative electrode material in sodium-ion batteries, pouch cells were assembled utilizing the procedure explained in section 3.2.1. The galvanostatic cycling experiments were performed directly after assembling using a multichannel MPG-2 potentiostat from Biologic Science Instruments (Software EC-LAB VIO-34). For the cycling studies the GCPL-technique (Galvanostatic Cycling with Potential Limitation) was selected. The charge/discharge experiments were started with a resting time of 12 hours followed by cycling primarily at

50 mA/g for 50 times continued at 25 mA/g for 100 times. The potential limits were set between 0.1-2 V vs. Na^+/Na.

4 Results and Discussion

4.1 Masses of the Nanotube Layers

Anodization of the Ti foils was carried at different voltages and for different times, as explained in the experimental part. To determine the masses of the nanotube layers that are formed on the Ti samples under the specific anodization conditions, the method explained in section 3.1.2 was used. In Table 2 the determined masses as well as the corresponding anodization conditions are summarized. It can be seen that an extension of the anodization time from 1 hour to 2 hours at the same applied voltage does not result in a doubled mass, since etching of the tube tops is more advanced at longer anodization times. However, the determined masses have to be regarded with caution, because the nanotube layer was peeled off with the Scotch tape directly after the cleaning and drying process. Therefore, it is possible that remnants of the electrolyte or small amounts of water from the cleaning procedure are still present in the nanotubes leading to higher masses. A very precise determination of the masses using this method was not possible. When the nanotubes on the Ti foils were subjected to an extended drying process at 120 °C under vacuum over night in order to remove volatile rests, the adhesion of the nanotubes on the Ti foil becomes significantly stronger. The result is that the nanotube layers cannot be peeled off with the Scotch tape any more.

Table 2. Masses of the nanotube layers formed on the Ti foils under specific anodization conditions.

anodization voltage	anodization time	mass (mg)
30 V	2 h	0.56
40 V	1 h	0.84
40 V	2 h	1.14
50 V	1 h	1.69
50 V	2 h	2.28
60 V	30 min	1.72
60 V	1 h	2.77

4.2 SEM Images and EDX Analysis

4.2.1 Pristine Samples

As described in the experimental section, TiO_2 nanotube layers were formed by anodization of a Ti foil in a mixed electrolyte containing 97.6% ethylene glycol, 2% distilled water and 0.4% NH_4F at different voltages for different durations. Fig. 19 shows selected SEM images of the resulting TiO_2 nanotubes in the cross-sectional (a) and top-view (b-d). It can clearly be seen that anodization leads to the formation of compact, parallel-aligned nanotubes with smooth tube walls that are closed at the bottom and opened on top. However, from the top view in Fig. 19 (d) it can be observed that the tube tops do not show a well-ordered structure over the entire surface, but form some kind of bundled nanotubes. This bundling of the NTs could be produced during the drying process with compressed air, since the long nanotubes could stick together due to capillary forces acting between adjacent tubes. From the SEM image in Fig. 19 (b) it can be seen that the surface of the nanotubes are partially covered with a compact layer. These are remnants of the initiation layer that is formed in the first stage of tube growth, as mentioned in section 2.2.2. However, the formation of bundled nanotubes as well as the presence of debris of the initial layer can have a negative impact on the intercalation of sodium ions into the nanotubes, since fewer tubes are available for the insertion process. Therefore, different cleaning methods were applied to the anodized samples in order to remove surface debris as described in the experimental part in section 3.1.1. The influence of the cleaning procedure on the intercalation process is discussed in section 4.4.2.1 in more detail.

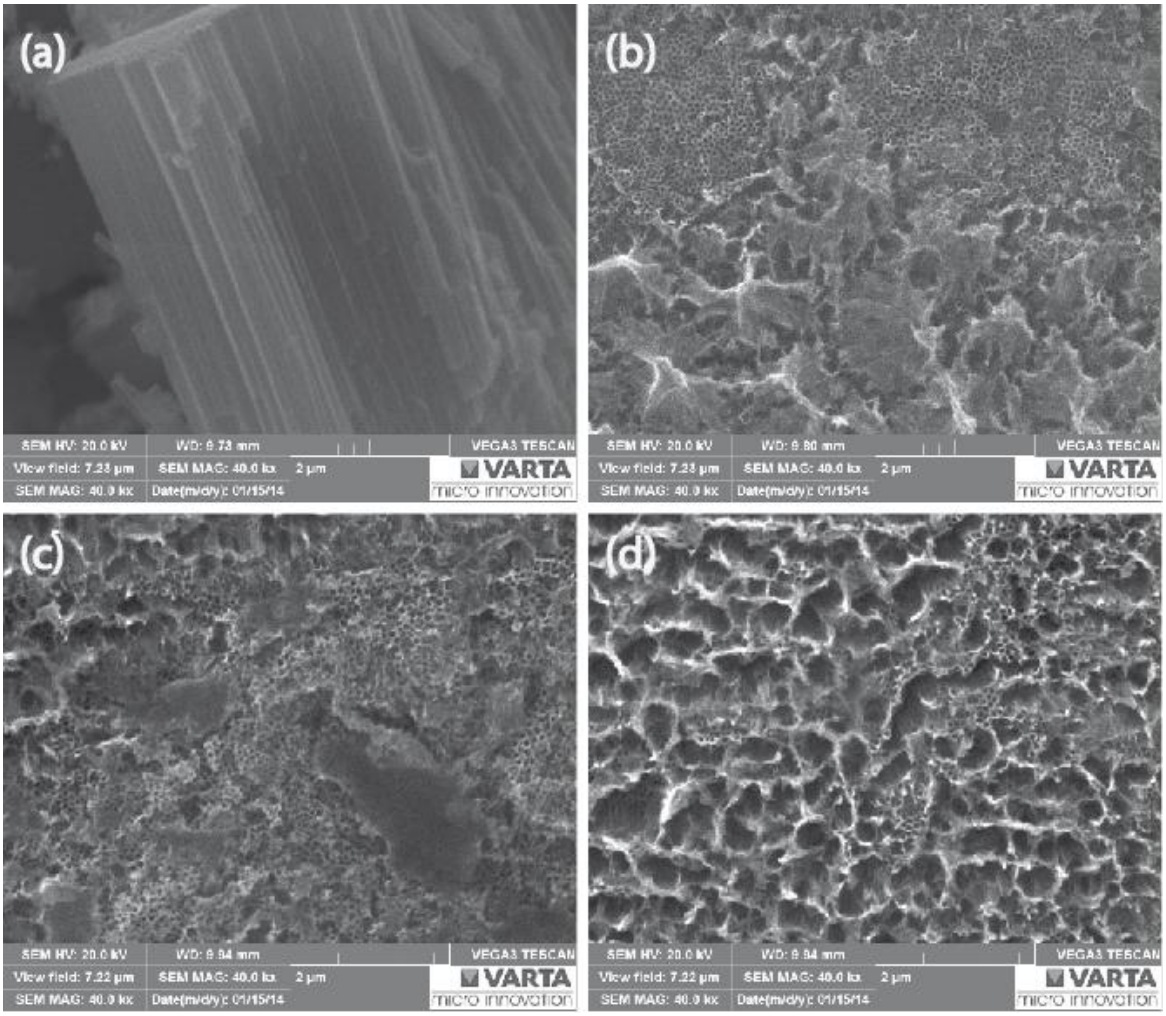

Fig. 19. Selected SEM images of self-organized TiO_2 nanotubes formed by anodization in a mixed electrolyte containing 97.6% ethylene glycol, 2% distilled water and 0.4% NH_4F at different voltages and for different durations. (a) Cross-sectional view of a nanotube layer grown at 50 V for 1 h. (b) Top-view of nanotubes produced by anodization at 30 V for 2 h. (c) and (d) Top-views of the tubes formed during a 2 h anodization at 40 V. The nanotubes formed at 30 and 40 V were ultrasonically cleaned in distilled water for 15 seconds after anodization.

Fig. 20 (a)-(d) shows SEM images of nanotube layers after anodization at 30, 40, 50 and 60 V. Left images are cross-sectional views of the tubes; right sides show the same image, however at higher magnification. From these SEM pictures it can be concluded that the length of the nanotubes increases with the applied voltage at a certain anodization time ranging in thicknesses from ~4.1 μm at 30 V to ~15.1 μm at 40 V for a 2 h anodic oxidation and from ~10,2 μm at 50 V to ~16,9 μm at 60 V, when anodization was done for 1 h. Also, larger diameters of the tubes can be observed at higher voltages indicating that intensified etching of the oxide layer occurs at higher potentials, leading to larger pores in the nanoporous structure during the tube formation process.

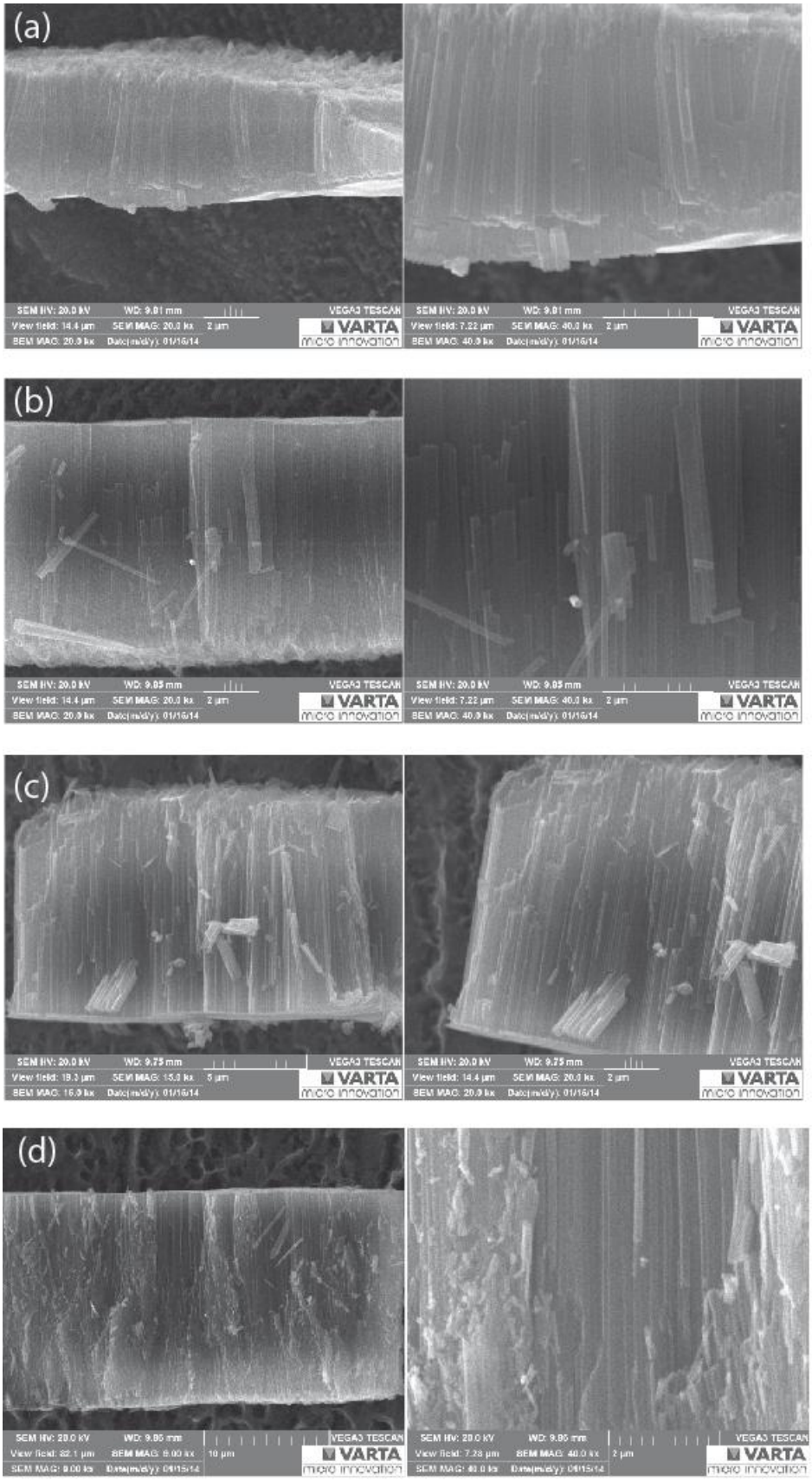

Fig. 20. SEM cross-sectional images of samples anodized at (a) 30 V for 2 h, (b) 40 V for 2 h, (c) 50 V for 1 h and (d) 60 V for 1 h. Left images show the whole cross-sectional of the nanotube layer; right sides show the same image, however at higher magnification.

4.2.2 Cycled Samples

Fig. 21 (a)-(c) shows SEM images of nanotube layers anodized at different voltages for different durations after galvanostatic cycling in a sodium half-cell using 1 M $NaClO_4$ in propylene carbonate as electrolyte. Left images are cross-sectional views; on the right side, the tube tops of the cycled samples can be observed. Fig. 21 (a) shows nanotubes produced by anodization at 30 V for 2 h after cycling first at 50 mA/g for 100 times and at 25 mA/g for 200 times between 0.8-2 V vs. Na^+/Na followed by sodiation/de-sodiation (cycling) at 50 mA/g and 25 mA/g, in each case for 100 times, in the potential range from 0.1-2 V vs. Na^+/Na. In Fig. 21 (b) SEM images of a nanotube layer formed during a 2 hour anodization at 40 V and galvanostatic cycled between 0.8-2 V vs. Na^+/Na at 50 mA/g for 100 times and at 25 mA/g for 200 times can be seen. From Fig. 21 (c) nanotubes obtained from anodization at 60 V for 30 minutes after cycling at 50 mA/g and 25 mA/g, in each case for 100 times, in the potential range from 0.8-2 V vs. Na^+/Na can be observed. The cycling process was finally stopped in the charged state for all three samples. As it can be seen in Fig. 21 (a) and (b), the length of the nanotubes increased from 4.159 μm to 15.11 μm with increasing applied potential from 30 V to 40 V using the same anodization time. For the sample prepared at 60 V only a layer thickness of 12.91 μm was determined, as shown in Fig. 21 (c). In this case, shorter nanotubes were obtained in spite of the high-applied voltage, since anodization was only carried out for 30 minutes. From the cross-sectional views it can clearly be seen that there is also a large effect of the applied potential on the tube diameters ranging from approximately 70 nm at 30 V, to 100 nm at 40 V and to 130 nm at 60 V.

From the cross-sectional view in Fig. 21 (a) it can be noticed that a thick layer is present on the tube tops. Since this sample was additionally galvanostatic cycled between 0.1-2 V vs. Na^+/Na, electrolyte decomposition could occur in this potential range, resulting in decomposition products that tip on the surface of the nanotube layers. Furthermore, degradation of the electrolyte and hence the formation of such a layer could also be caused by ageing of the electrolyte after extensive cycling of this sample over 500 times. A thin layer can also be observed on the surface of the nanotubes shown in Fig. 21 (b), however this layer is not that pronounced as in Fig. 21 (a).

From the SEM images in Fig. 21 (a)-(c) it can also be observed that intercalation of sodium ions into the tubes does not destroy the nanotubular structure.

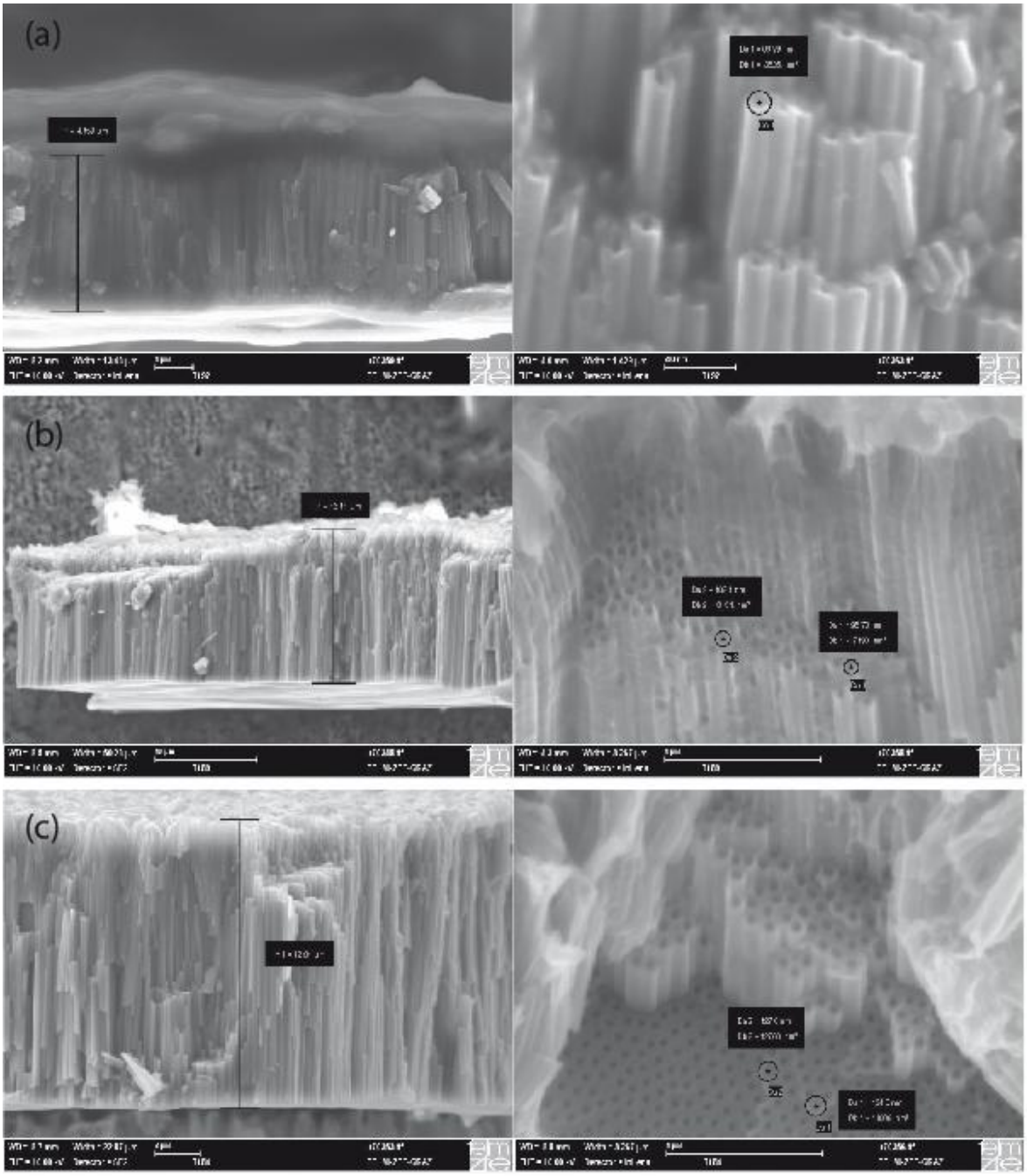

Fig. 21. SEM images of nanotube layers anodized at different voltages for different durations after galvanostatic cycling in a sodium half-cell using 1 M $NaClO_4$ in propylene carbonate as electrolyte. (a) Nanotubes produced by anodization at 30 V for 2 h after cycling first at 50 mA/g for 100 times and at 25 mA/g for 200 times between 0.8-2 V vs. Na^+/Na followed by sodiation/de-sodiation at 50 mA/g and 25 mA/g, in each case for 100 times, in the potential range from 0.1-2 V vs. Na^+/Na. (b) Nanotube layer formed during a 2 hour anodization at 40 V and galvanostatic cycled between 0.8-2 V vs. Na^+/Na at 50 mA/g for 100 times and at 25 mA/g for 200 times. (c) Nanotubes obtained from anodization at 60 V for 30 min after cycling at 50 mA/g and 25 mA/g, in each case for 100 times, in the potential range from 0.8-2 V vs. Na^+/Na. The cycling process was finally stopped in the charged state for all three samples. Cross sectional images on the left side indicate the thickness of the nanotube layers. From the images on the right side the diameter of the tubes can be obtained.

As seen in Fig. 22 (a)-(c) on the left side, EDX analysis were performed at the same three samples at different points along the nanotubes. Additionally, EDX spectra were recorded from the surface of the nanotube layers during the top-view observation of the sample. The results obtained from these analyses are listed on the right side in Fig. 22 (a)-(c). Clearly it can be seen that the amount of sodium detected decreases, when moving from the top to the bottom of the nanotubes, suggesting that most of the sodium is inserted in the top parts of the tubes, while the bottom parts are probably under-used. It is very likely that a fully sodiated state is not reached at the bottom of the nanotubes at these cycling rates. By comparing the three samples, nearly the same amount of Na can be found in the NTs. Thus, it can be concluded that sodium ions can also intercalate in small diameter tubes and not only in larger diameter tubes as previously reported in the literature (see Ref. [25]).

Also, the nanotubes have a certain fluorine content. This finding is consistent with the assumption that a fluoride rich layer is formed between the nanotubes in the early stage of tube growth as mentioned in section 2.2.2. Chlorine in the top parts of the tubes as well as on the surface of the nanotube layer could only be detected for the samples, on which a post-cycling thick layer is present on the tube tops, as shown in Fig. 22 (a). Moreover, a larger amount of sodium was proven on this surface compared to the other samples. This could indicate that decomposition of the electrolyte, that consists of $NaClO_4$ in propylene carbonate, occurs and that the degradation products accumulate on the nanotube tops forming this thick layer, when galvanostatic cycling was carried out in the potential range from 0.1-2 V vs. Na^+/Na and for more than 500 cycles. This is a remarkable result that points toward the existence of a sodium-based SEI on the nanotubular electrode. So far, electrolyte decomposition in Na-ion cells has been known to produce mostly soluble products and no appreciable SEI was formed. This is one of the first indications that, in some conditions, it would appear possible to form a stable SEI. The fact that the layer appears, when cycling is done down to low electrochemical potentials of the titania electrodes, goes in line with the SEI formation mechanism by the decomposition of electrolyte. However, further study would be required in order to evaluate the stability and the properties of this layer and positively identify it as a SEI-type film.

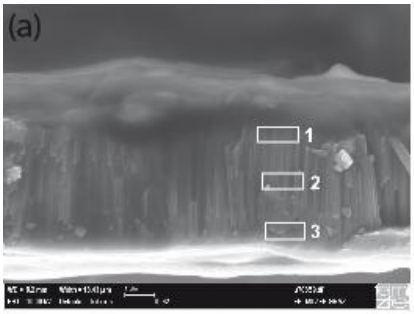

	elements (at%)				
	O	F	Na	Cl	Ti
position 1	62.30	4.41	18.76	0.56	13.97
position 2	55.94	6.26	17.02	0.19	20.59
position 3	53.21	7.06	14.08	-	25.65
surface	61.07	1.75	30.29	0.95	5.93

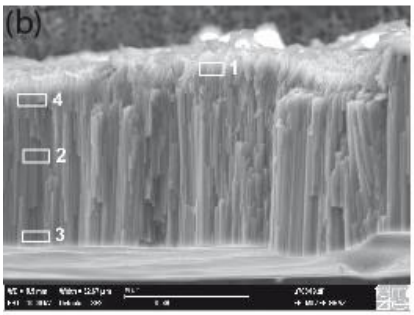

	elements (at%)				
	O	F	Na	Cl	Ti
position 1	61.08	5.07	24.94	-	8.90
position 2	55.75	7.04	16.14	-	21.07
position 3	57.71	7.12	13.44	-	21.72
position 4	63.06	5.19	18.58	-	13.17
surface	57.92	4.87	23.44	-	13.77

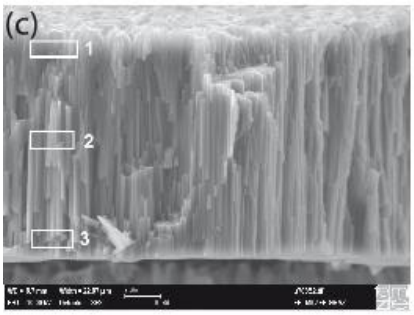

	elements (at%)				
	O	F	Na	Cl	Ti
position 1	61.64	4.24	20.83	-	13.30
position 2	60.88	7.26	15.43	-	16.43
position 3	61.06	8.91	13.42	-	16.62
surface	60.86	4.71	22.08	-	12.36

Fig. 22. Cross-sectional SEM images of nanotube layers anodized at (a) 30 V for 2 h, (b) 40 V for 2 h, (c) 60 V for 30 minutes after galvanostatic cycling. The numbered rectangels indicate the areas from which EDX spectra were recorded. The results obtained from these analyses are given in the tables on the right side.

4.2.3 Nanotubes modified with Sn

As explained in the experimental section, filling of the nanotubes was attempted by electrodeposition of tin according to four different approaches (1-4). Fig. 23 (a)-(c) shows SEM images of the nanotube layers after Sn was electro-deposited following the first three approaches. Left images are top-views of the tubes; right sides show the same image, however at higher magnification. From the top-view images in Fig. 23 (a) it can be seen that a reduction of the nanotubes followed by an immersion of the sample in a sensitizer and initiator solution (approach 1) leads to an electrodeposition of tin with a worm-like structure. When the solution is stirred during the Sn deposition step (approach 2), larger Sn particles as well as conglomerates of such particles can be found on the surface of the nanotube layer, as shown in Fig. 23 (b). From Fig. 23 (c) it can be observed that an

application of the third approach, where no initiator solution is used, leads to the deposition of tin in form of small particles.

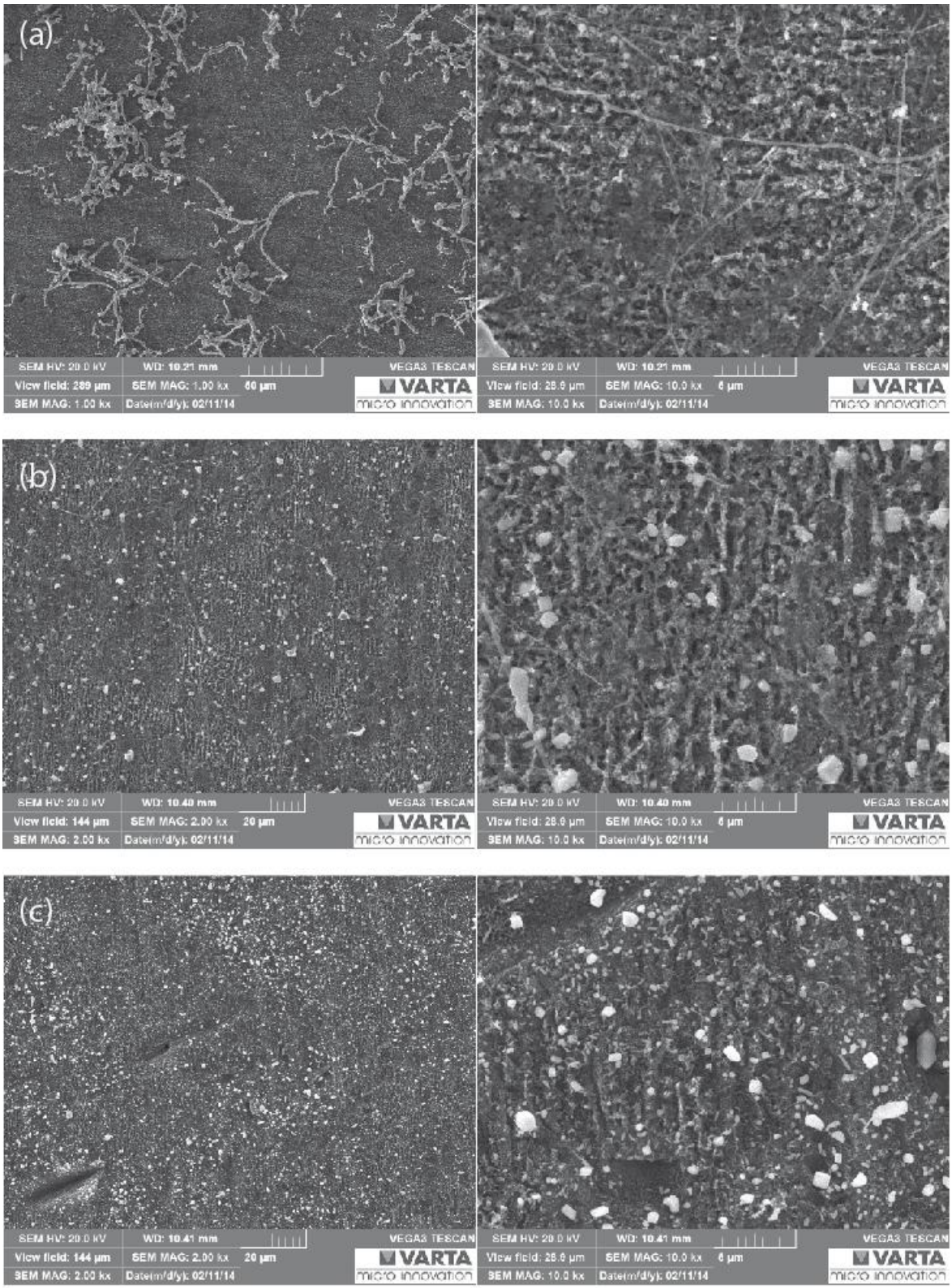

Fig. 23. SEM images of samples anodized at 40 V for 2 h after electrodeposition of tin using three different approaches (1-3). Left images are top-views of the tubes; right sides show the same image, however at higher magnification.

Fig. 24 (a)-(c) shows SEM cross-sectional images of the same samples. Additionally, a nanotube layer in cross-sectional view after Sn was deposited using approach 4, where only reduction of the tube bottoms and the Sn electrodeposition step was carried out, can be seen in Fig. 24 (d). From this image it can be observed that the tin particles deposited on the surface of the nanotube layer are much bigger than the diameter of the tubes. Therefore, it seems that no filling of the tubes was achieved by this approach. From the cross-sectional views in Fig. 24 (a)-(c) it is apparent that no Sn can be found in the nanotubes leading to the conclusion that electrodeposition of tin using the above-mentioned approaches is not suitable for the filling of the tubes with Sn.

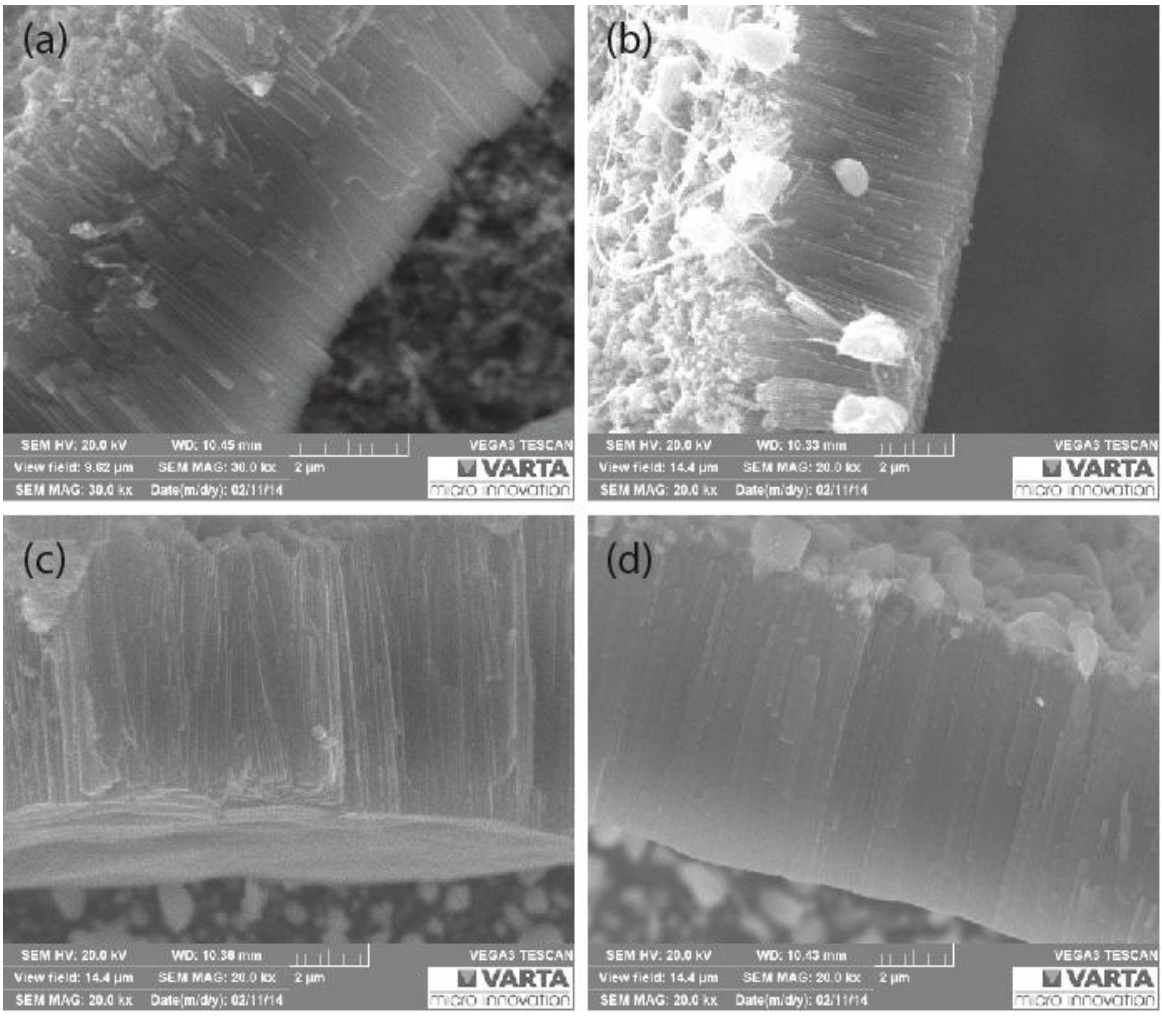

Fig. 24. Cross-sectional SEM images of the nanotube layers after Sn was electro-deposited following approach (a) 1, (b) 2, (c) 3 and (d) 4, as mentioned in section 3.4.1.

4.3 XRD analysis

4.3.1 Pristine Samples

The XRD patterns of nanotube layers grown by anodic oxidation at 30 V, 40 V and 50 V in each case for 2 h and at 60 V for 1 h are presented in Fig. 25. For comparison also the XRD spectrum of the pure Ti foil without nanotubes on it is shown. Only peaks from the underlying Ti substrate can be seen in the XRD patterns of the pristine samples. From these XRD analyses it is also apparent that the nanotubes are of an amorphous nature after anodization, as indicated by a broad “hump” seen in the 2 θ range between 20° and 32°. It has to be mentioned that the intensity of signal of the amorphous phase measured on the different nanotube layers cannot be compared directly, since also the lengths of the nanotubes increase with the applied voltage. Consequently, most of the amorphous phase signal can be detected for the sampled produced by anodization at 60 V for 1 h, while for the other samples the signal has lower intensity. Finally, from the XRD patterns shown in Fig. 25 no correlation between the crystallinity or amorphicity and the anodization voltage can be observed.

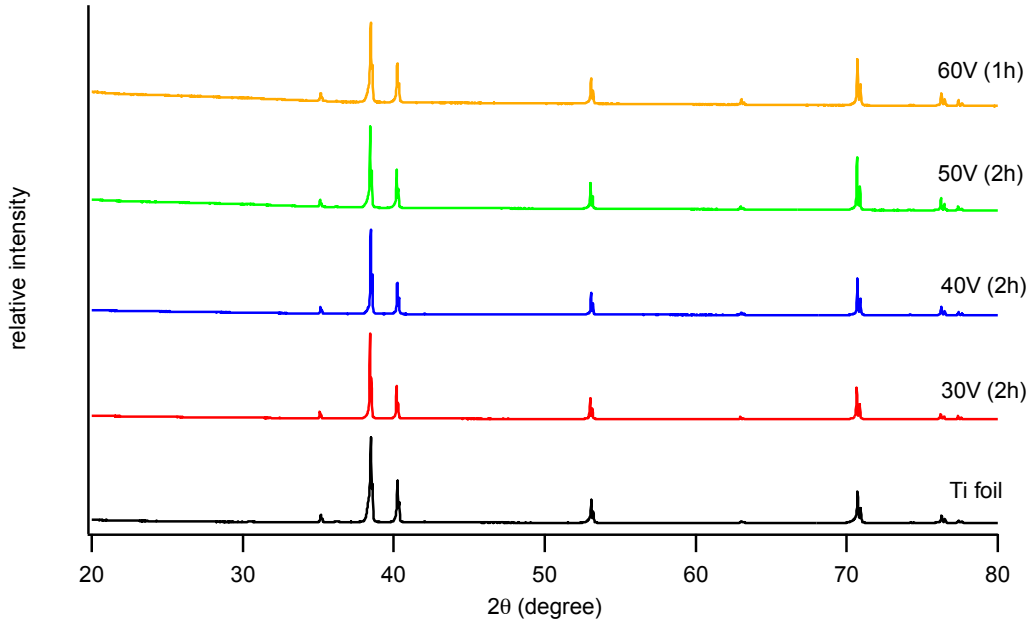

Fig. 25. XRD patterns of TiO_2 nanotube layers grown by anodic oxidation at 30 V, 40 V and 50 V in each case for 2 h and at 60 V for 1 h. For comparison also the XRD spectra of the pure Ti foil without nanotubes on it is shown.

Fig. 26 shows the X-ray diffraction patterns of TiO_2 nanotubes produced by anodization at 40 V for 2 h recorded one day (b), 10 days (c) and 100 days (d) after preparation. For comparison also the XRD spectrum of the Ti substrate (a) without nanotubes on it can be seen. From these XRD patterns it can be observed that the amorphous sample does not crystallize in time.

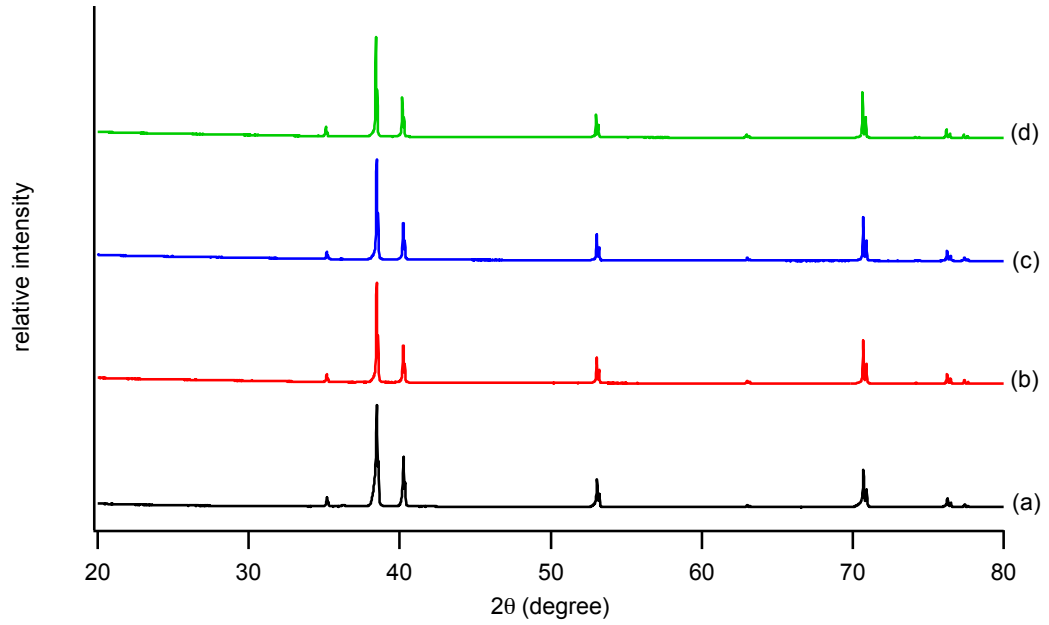

Fig. 26. X-ray diffraction patterns of TiO_2 nanotubes produced by anodization at 40 V for 2 h recorded (b) one day, (c) 10 days and (d) 100 days after preparation. For comparison also the XRD spectrum of the Ti substrate (a) without nanotubes on it can be seen.

4.3.2 Annealed Samples

TiO_2 nanotube layers grown by anodization at 40 V for 2 h were annealed at 100 °C, 200 °C, 300 °C and 350 °C in argon as well as in air for 1 h in order to study the effect of heat treatment upon the crystallinity of the samples. Furthermore, the influence of the used gas on the annealing process was studied. XRD patterns of the samples before and after heat treatment are shown in Fig. 27 and in Fig. 28. As already mentioned in the previous section, the as-anodized samples are amorphous in its nature. Amorphous material is still present up to an annealing temperature of 200 °C. After annealing at 300 °C in air as well as in argon phase transition from amorphous to anatase can be observed. This crystallization to anatase is particularly apparent from the peak, which appears at 2 θ= 26° in the XRD patterns of the annealed samples. Further crystalline anatase peaks can be detected at 37°, 48°, 54° and 55° in the XRD spectra of both heat-treated samples. The same results can be obtained from the XRD diffraction patterns after annealing at 350 °C

for 1 h in argon as well as in air, as seen in Fig. 27 and Fig. 28. Summing up, the XRD results show that heat treatment of the nanotubes at 300 °C and 350 °C in argon as well as in air leads to a phase transition from the originally amorphous tubes to crystalline anatase structures. The used gas influences the preferential crystallographic orientation of the anatase formed, as the relative intensity of the peaks at 26° and 37° differs and depends by the sample being annealed in air or in argon. This effect opens the path towards the preparation of favourably oriented nanotubular layer by adjusting the oxygen partial pressure during the annealing step.

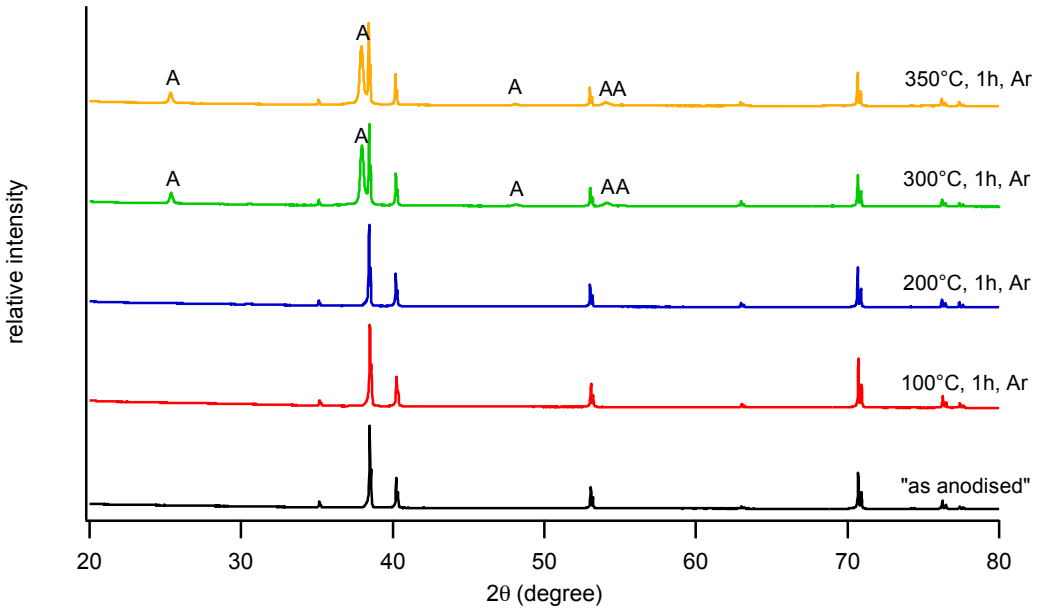

Fig. 27. XRD diffraction patterns of TiO_2 nanotubes produced by anodization at 40 V for 2 h before and after heat treatment in argon at different temperatures for 1 h. In the XRD pattern the peaks marked A correspond to anatase phase.

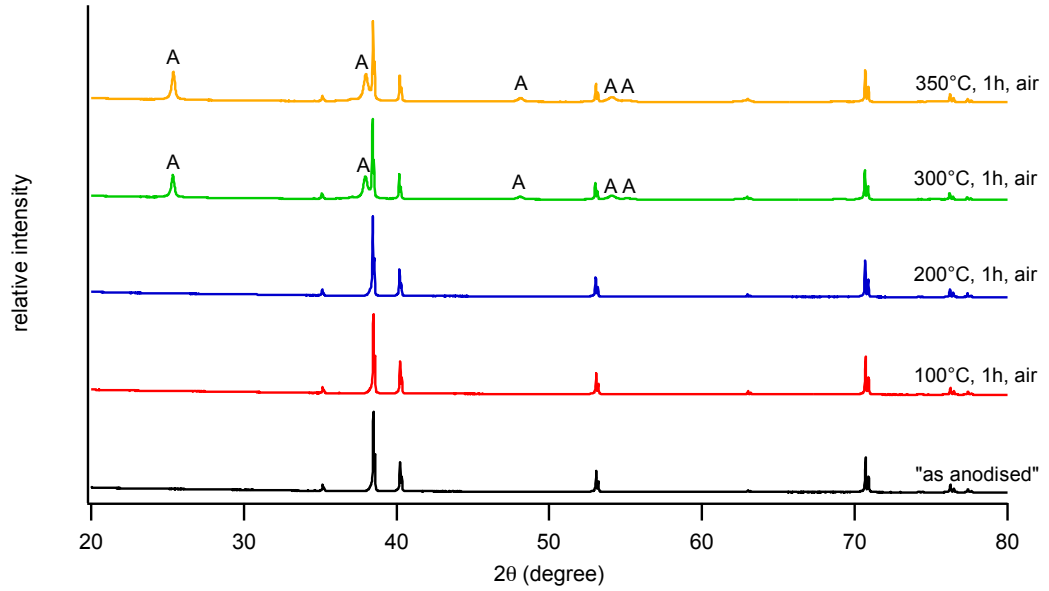

Fig. 28. XRD diffraction patterns of TiO_2 nanotubes produced by anodization at 40 V for 2 h before and after heat treatment in air at different temperatures for 1 h. In the XRD pattern the peaks marked A correspond to anatase phase.

Fig. 29 and Fig. 30 show optical images of TiO_2 nanotube layers before (a) and after heat treatment at 100 °C (b), 200 °C (c), 300 °C (d) and 350 °C (e) in argon (Fig. 29) and in air (Fig. 30) for 1 h. From Fig. 29 it is clear that phase transition from amorphous titania to anatase is accompanied by a blackening of the tubes, when annealing is carried out in argon. The reason for such behaviour is the formation of O^{2-} vacancies and the consequent reduction of Ti^{4+} to Ti^{3+} in the oxygen depleted atmosphere. Indeed, a pure argon atmosphere would correspond to have reducing conditions; the oxygen loss from the titania to the surrounding (argon) atmosphere is thermodynamically favourable. Some colour change can also be observed when the samples are annealed in air, as seen in Fig. 30. However, the tubes do not turn black after heat treatment at 300 °C in air, which leads to the conclusion that much more Ti^{3+} states are formed during annealing under low oxygen partial pressure than in air. From the optical images it can also be observed that the mechanical stability of the nanotube layers decreases with increasing annealing temperature leading to a partial detachment of the nanotubes from the Ti substrate mostly occurring at the edges of the anodized region.

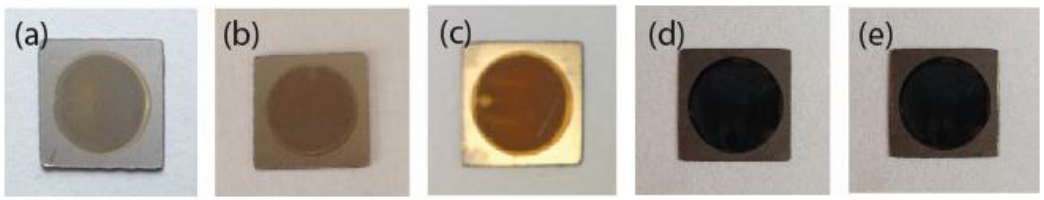

Fig. 29. Optical images of TiO_2 nanotubes before and after heat treatment in argon at different temperatures for 1 h: (a) as-anodized; (b) 100 °C; (c) 200 °C; (d) 300 °C; (e) 350 °C

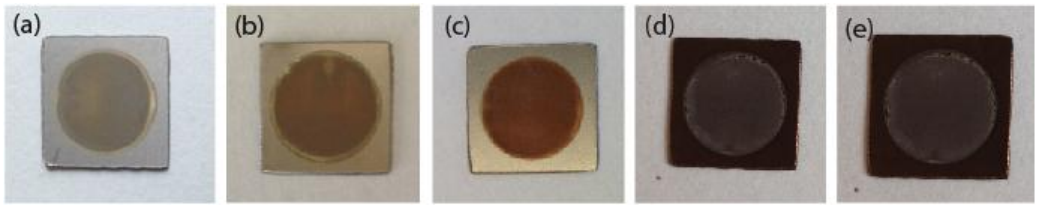

Fig. 30. Optical images of TiO_2 nanotubes before and after heat treatment in air at different temperatures for 1 h: (a) as-anodized; (b) 100 °C; (c) 200 °C; (d) 300 °C; (e) 350 °C

4.3.3 Cycled Samples

Post-mortem X-ray diffraction experiments were carried out on already cycled samples in order to study the effect of sodiation and de-sodiation on the amorphicity of the nanotubes. Fig. 31 shows XRD patterns of nanotube layers grown by anodization at 40 V for 2 h after galvanostatic cycling in a sodium half-cell using 1 M $NaClO_4$ in propylene carbonate as electrolyte. For comparison also the XRD spectrum of the pure Ti foil without nanotubes on it (Fig. 31 (a)) as well as the XRD pattern of a pristine sample (Fig. 31 (b)) is shown. Fig. 31 (c) shows the X-ray diffraction peaks of the nanotubes after cycling first at 50 mA/g for 100 times and at 25 mA/g for 100 times between 0.8-2 V vs. Na^+/Na followed by sodiation/de-sodiation at 50 mA/g and 25 mA/g, in each case for 100 times, in the potential range from 0.1-2 V vs. Na^+/Na. The cycling program was finally stopped so the samples were in the charged (sodiated) state. In Fig. 31 (d)-(e) XRD patterns of nanotube layers after cycling at 50 mA/g and 25 mA/g, in each case for 100 times, in the potential range from 0.8-2 V vs. Na^+/Na can be observed. However, for the sample in Fig. 31 (d) the cycling program was stopped in the charged state, while the nanotubes for Fig 31 (e) were obtained in the discharged (de-sodiated) state. From the XRD patterns it can be seen that the nanotubes remain amorphous upon cycling.

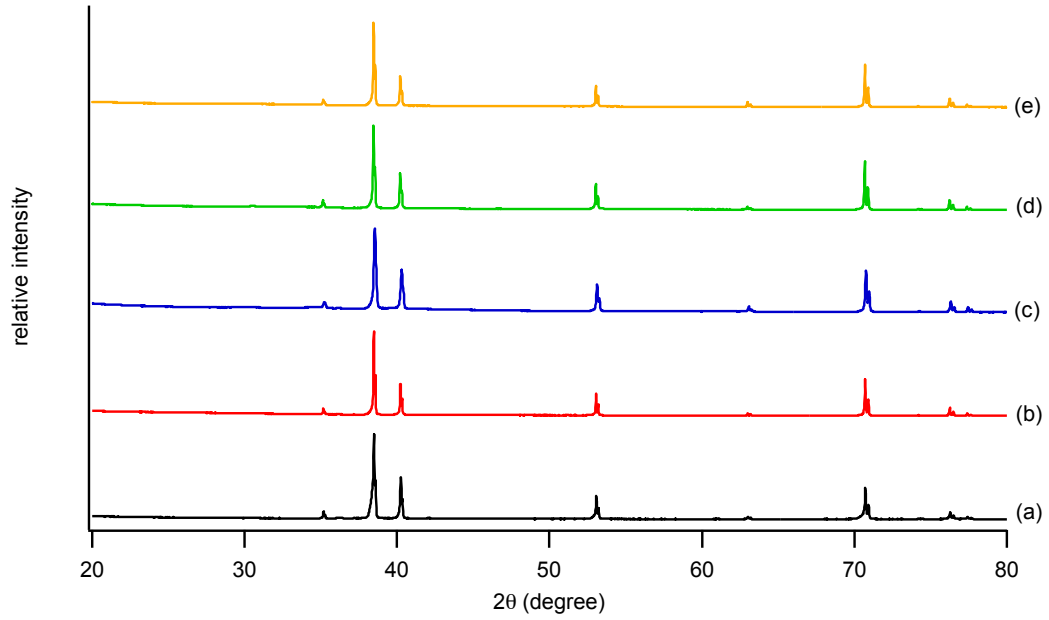

Fig. 31. XRD patterns of nanotube layers grown by anodization at 40 V for 2 h after galvanostatic cycling in a sodium half-cell using 1 M $NaClO_4$ in propylene carbonate as electrolyte. (c) X-ray diffraction peaks of the nanotubes after cycling first at 50 mA/g for 100 times and at 25 mA/g for 100 times between 0.8-2 V vs. Na^+/Na followed by sodiation/de-sodiation at 50 mA/g and 25 mA/g, in each case for 100 times, in the potential range from 0.1-2 V vs. Na^+/Na. The cycling program was finally stopped so the samples were in the charged (sodiated) state. (d)-(e) XRD patterns of nanotube layers after cycling at 50 mA/g and 25 mA/g, in each case for 100 times, in the potential range from 0.8-2 V vs. Na^+/Na. However, for the sample in (d) the cycling program was stopped in the charged state, while the nanotubes for (e) were obtained in the discharged (de-sodiated) state. For comparison also the XRD spectrum of the pure Ti foil without nanotubes on it (a) as well as the XRD pattern of a pristine sample (b) is shown.

4.4 Cyclic Voltammetry and Galvanostatic Cycling

4.4.1 Cyclic Voltammetry

Fig. 32 (a)-(c) shows cyclic voltammograms of TiO_2 nanotube layers grown by anodization at 30 V for 2 h (a), 40 V for 2 h (b) and 50 V for 2 h (c) in 1 M $NaClO_4$/PC in the potential range of 0.1-2 V vs. Na^+/Na at scan rates between 0.05 mV/s and 10 mV/s, respectively. As seen in Fig. 32 (a), the CV curve of the sample anodized at 30 V for 2 h at a scan rate of 0.05 mV/s displays a reduction peak in the range of 0.5-0.8 V vs. Na^+/Na in the first cycle, which can be attributed to electrolyte decomposition and hence to the formation of a passive layer on the nanotubes. The absence of this peak in the second cycle as well as the fact that no corresponding oxidation peak exists, indicates that this decomposition process is irreversible. This CV result is consistent with the findings of the SEM investigation on cycled samples, which show the presence of a layer on the nanotube tops, when galvanostatic cycling of the titania tubes was carried out below 0.8 V, as already explained in section 4.2.2. The above-mentioned reduction peak also appears in the CVs of the samples anodized at 40 V and 50 V in the first cycle at the same scan rate, however shifted to lower potentials and more pronounced. At voltages close to 0.1 V yet another reduction peak can be observed that is likely related to further decomposition of the electrolyte solution. However, this peak can only be found at lower scan rates between 0.05 mV/s and 0.5 mV/s.

Further, no definite peaks can be observed in the CV curves of all three samples, since TiO_2 nanotubes produced by anodization under this conditions are amorphous (see section 4.3.1). Thus a plurality of sites for Na-ion insertion exists, having (at least) different thermodynamic properties and hence showing a different and continuous electrochemical response. At higher potentials, slightly more accessible sites will be first occupied by sodium ions, while with decreasing voltage also sites that are more difficult to access will be available for the insertion of sodium ions, resulting in an increase of the reduction current with decreasing potential, as shown in Fig. 32 (a)-(c). Furthermore, a higher reductive current flow at lower potential values can be observed in the CV curves of the sample anodized at 50 V for 2 h compared to titania nanotubes grown by anodization at 30 V for 2 h at the same scan rate. Since nanotubes grow longer with increasing applied voltage at constant anodization time, it seems that more sites can be occupied by sodium in longer tubes leading to higher current values. This is also a strong indication that the nanotube walls present electrochemical activity over their surface and that electrochemical activity is not limited to the bottom or to the top of the nanotubes.

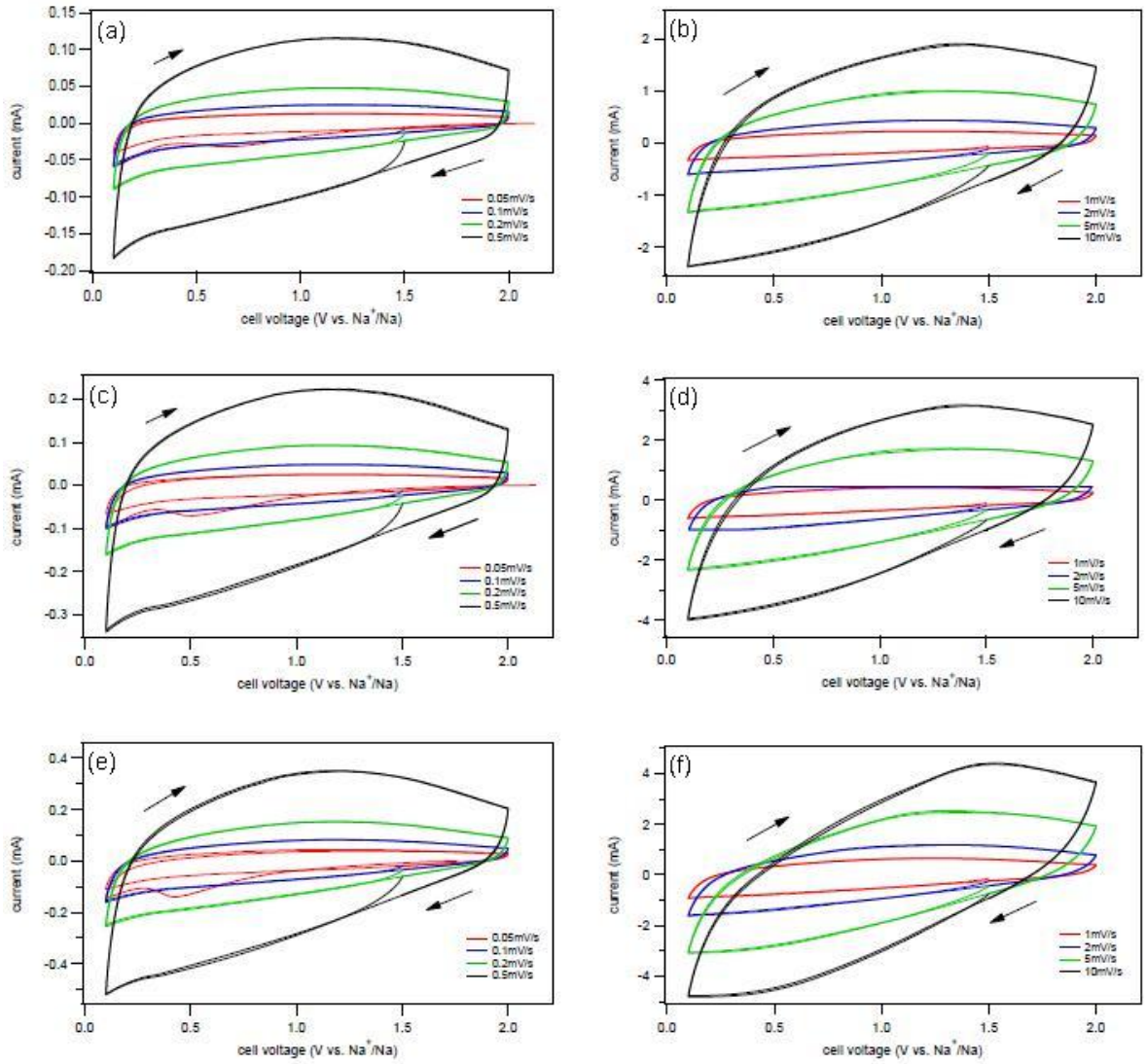

Fig. 32. Cyclic voltammetry data of TiO_2 nanotube layers grown by anodization at (a) 30 V for 2 h, (b) 40 V for 2 h and (c) 50 V for 2 h in 1 M $NaClO_4$/PC in the potential range of 0.1-2 V vs. Na^+/Na at different scan rates. On the left side CVs at scan rates of 0.05 mV/s, 0.1 mV/s, 0.2 mV/s and 0.5 mV/s are presented. Right side shows cyclic voltammograms of the tubes at 1 mV/s, 2 mV/s, 5 mV/s and 10 mV/s.

4.4.2 Galvanostatic Cycling

4.4.2.1 Influence of Anodization Voltage and Time

Electrochemical characterization of the TiO_2 nanotubes anodized at different voltages and for different durations as negative electrode material for sodium-ion batteries was done by means of galvanostatic cycling in a sodium half-cell using 1 M $NaClO_4$ in propylene carbonate as electrolyte. Fig. 33 shows potential-x in Na_xTiO_2 curves for selected cycles (1, 2, 5, 10, 50, 100, 150 and 200) for samples grown by anodization at 30 V for 2 h (a), 40 V for 2 h (b), 50 V for 1 h (c) and 2 h (d) and at 60 V for 30 min (e) and 1 h (f) after constant current cycling first at 50 mA/g for 100 times, then at 25 mA/g for the next 100 or

200 times in the potential range of 0.8-2 V vs. Na^+/Na. X represents the molar ratio of Na inserted into TiO_2, thus giving a sodiated compound with the general stoichiometry Na_xTiO_2.

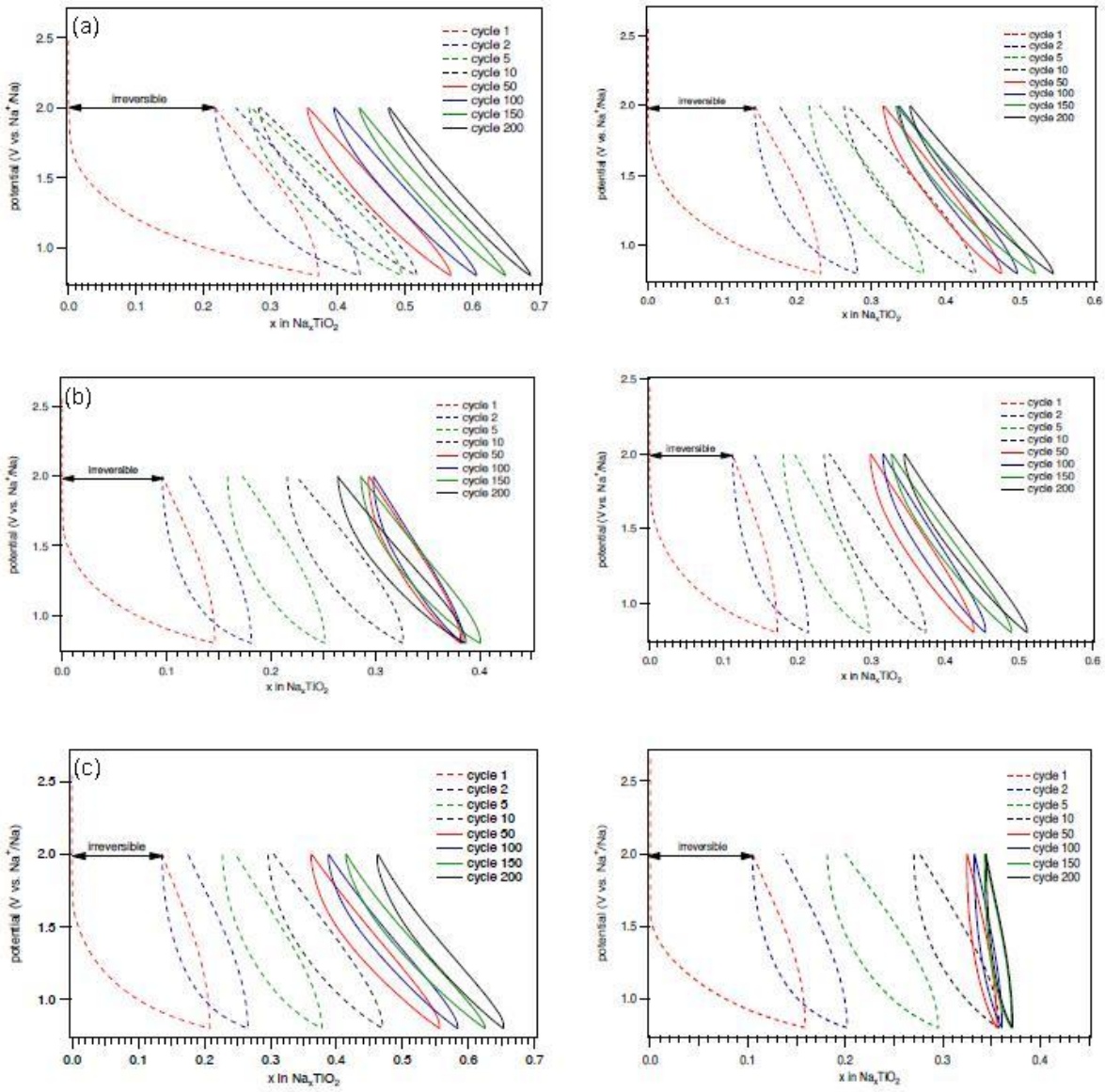

Fig. 33. Potential-x in Na_xTiO_2 curves for the 1st, 2nd, 5th, 10th, 50th, 100th, 150th and 200th cycle for samples grown by anodization at (a) 30 V for 2 h, (b) 40 V for 2 h, 50 V for (c) 1 h and (d) 2 h and at 60 V for (e) 30 min and (f) 1 h after constant current cycling first at 50 mAh/g for 100 times, then at 25 mAh/g for the next 100 or 200 times in the potential range of 0.8-2 V vs. Na^+/Na. X represents the molar ratio of Na inserted into TiO_2.

From these curves it is apparent that sodium intercalation into the nanotubes is not fully reversible in the first few cycles. This suggests that large irreversible reactions including reactions of Na with surface groups on the tubes as well as electrolyte decomposition may take place, particularly during the first charge/discharge process as indicated with a

double arrow in the respective curves. It can be seen that nanotubes grown by anodization at lower voltages trap irreversibly a larger amount of sodium than tubes produced at higher anodization voltages. Only from the 50th cycle fully reversible sodium ion uptake and release can be observed. The corresponding reversible reaction for sodiation and de-sodiation of the titania nanotubes is given by Eq. 9.

$$xNa^+ + xe^- + TiO_2 \leftrightarrow Na_xTiO_2 \quad (9)$$

The amount of Na reversibly cycled can also be obtained from the potential-x in Na_xTiO_2 curves shown in Fig. 33. Table 3 summarizes the anodization conditions for the nanotubes as well as the experimentally determined x-values, where x represents the molar fraction of sodium reversibly inserted and extracted according to equation 9.

Table 3. Molar fraction of sodium reversibly cycled for titania nanotubes grown by anodization under several specific conditions. The x values data were extracted from the 50th cycle corresponding to cycling at 50 mA/g as well as from the 150th cycle standing for the sodiation/de-sodiation process at 25 mA/g.

anodization voltage	anodization time	x (at 50 mA/g)	x (at 25 mA/g)
30 V	2 h	0.21	0.20
40 V	2 h	0.16	0.18
50 V	1 h	0.14	0.16
50 V	2 h	0.10	0.12
60 V	30 min	0.19	0.20
60 V	1 h	0.03	0.03

The areal capacity as a function of the cycle number for the same samples is graphically illustrated in Fig. 34. It can be seen that the values for the charge and discharge capacity for the first cycle are very different leading to high irreversible capacities. This fact is due to large irreversible reactions taking place during the first cycle, as already mentioned before. Thereafter, the areal capacity increases and stabilises finally at around 40 cycles. An exception is the sample anodized at 60 V for 1 h that shows a very large capacity fade after the first ten cycles leading to very low capacity values for the following ones. The reason behind this behaviour is difficult to identify unequivocally at this stage. One possible explanation might be related to the possible peeling off/detachment of the nanotube film from the current collector. Indeed, it was observed during the synthesis and

cleaning of the nanotubes (see chapter 3) that the titania nanotubes synthesized in these particular conditions (60 V, 1 h) have a tendency to detach from the substrate. The reason behind this was identified in the literature as the build-up of stress at the metal-oxide interface that occurs together with the accumulation of F^- ions. Since Na insertion is usually accompanied by some volume expansion of the host material, it is thus plausible to consider that some stress may develop in the oxide material during cycling that may, in some conditions, lead to the detachment of the nanotube layer. There might be, however, other mechanism related to this capacity loss that would require further study.

Furthermore, the charge/discharge curves show that the capacity values increase with the applied anodization voltage, when the anodization time is fixed. It has been previously shown that the higher the voltage, the larger the diameter of the anodic nanotubes. The typical anodization time for these experiments was 2 hours. This suggests that at larger titania nanotubes diameter more sites can be occupied by sodium. Comparing the two samples anodized at 50 V but for different anodization times (1 h and 2 h), it can be seen that nanotubes grown during a 2 h anodization show slightly higher capacity values for the first 15 cycles due to the longer tube length knowing that at a certain applied potential the length is determined by the anodization time. However, thereafter, the capacity fades to a certain extent reaching lower capacity values than the sample anodized for 1 h. One possible explanation for that can be that some parts of the nanotube layer peels off during cycling, since tubes grown under these conditions are not that stable and do not adhere that strong on the underlying titanium substrate. The highest areal capacity can be obtained for the sample produced by anodic oxidation at 60 V for 30 min. Though, the tubes are shorter than for the sample anodized at 40 V for 2 h, as shown in the SEM images in Fig. 21 discussed in section 4.2.2 and therefore lower capacity values are expected, higher capacities can be reached, since the large diameter of these tubes (the diameter increases with applied potential) also contribute to achieve higher areal capacities. In conclusion, not only the tube length, but also the diameter influences the accessible areal capacity values.

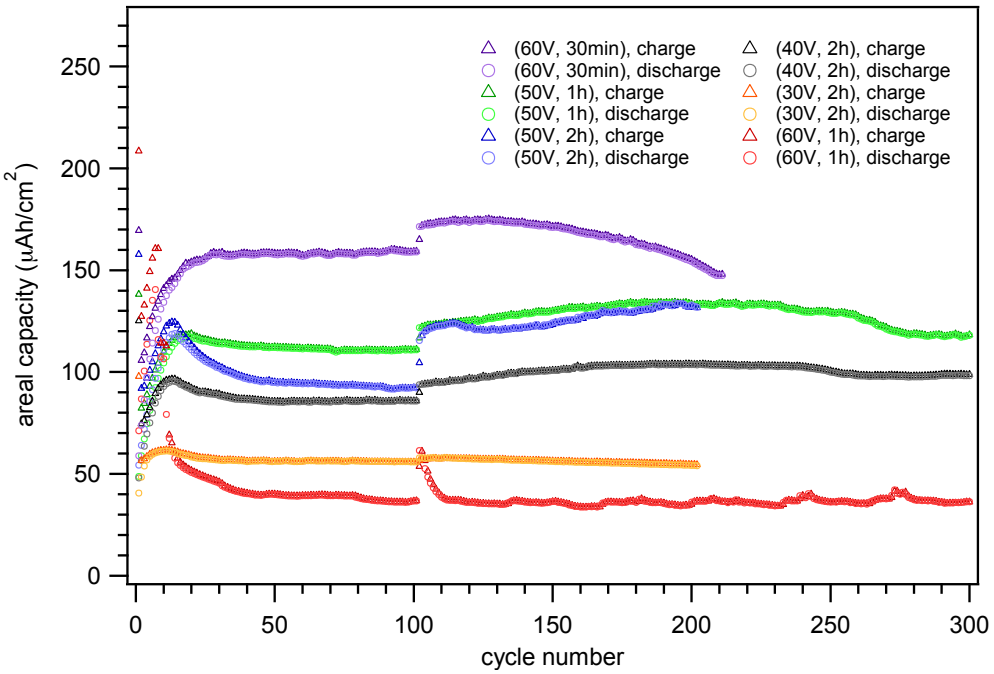

Fig. 34. Areal capacity as a function of the cycle number for titania nanotubes grown by anodization under different conditions. The tubes were cleaned by rinsing with distilled water and drying with compressed air after anodization. Galvanostatic cycling was done in sodium half-cells using 1 M $NaClO_4$ in PC as electrolyte at 50 mA/g for the first 100 times, followed by discharging/charging at 25 mA/g for the next 100 or 200 times in the potential range of 0.8-2 V vs. Na^+/Na.

The corresponding specific capacities of the cycled titania nanotubes are presented in Fig. 35. It can be seen that the highest specific capacity is obtained for the sample grown by anodization at 30 V for 2 h reaching 71.1 mAh/g at both 50 mA/g and 25 mA/g. However, this result is surprising, when compared to the findings illustrated in Fig. 34 that show the lowest areal capacity for this sample. It may be possible that a larger fraction of the nanotubes is effectively used, when they are short rather than long. Since the transport of sodium ions in solution is governed by diffusion, it can be expected that the shorter the nanotubes the shorter the diffusion length of Na ions to the bottom of the nanotubes. The geometry of the nanotubes (i.e. the diameter) may play a role: mass transport by diffusion in confined spaces, such as inside the nanotubes, might be hindered and slower than in the bulk of the electrolyte. In such a situation longer tubes, but with a larger diameter should present a similar behaviour. Indeed, the titania nanotubes produced at 60 V for 30 min deliver high reversible capacity values ranging from 65 mAh/g at a current of 50 mA/g to 70 mAh/g, when cycling is carried out at 25 mA/g. These specific capacities are very similar to the capacities of the 30 V sample. However, this cell shows a continuous capacity fade from the 150th cycle. The samples anodized at 40 V for 2 h exhibit great cycling stability over 250 cycles indicating a fully reversible Na ion uptake and release.

Only after 250 cycles the capacity decreases due to ageing of the cell and consumption of the electrolyte. The corresponding capacity values are 53 mAh/g at 50 mA/g and 62.6 mAh/g at a lower current of 25 mA/g. Comparing both samples anodized at 50 V but for different times, the nanotubes grown during a 1 h anodization delivers higher specific capacity value ranging from 45 mAh/g at 50 mA/g to 54.5 mAh/g for constant current cycling at 25mA/g compared to 29.5 mAh/g and 38.6 mAh/g for the sample anodized for 2 hours. As already mentioned above, nanotubes produced by anodic oxidation at 50 V for 2 h are not that stable and some parts of the layer might peel off after anodization. From Fig. 35 it can also be observed that upon decreasing the current from 50 mA/g to 25 mA/g the accessible capacities increase. This is probably because sodium ions have more time available for diffusion at these lower currents and can therefore penetrate deeper into the tubes.

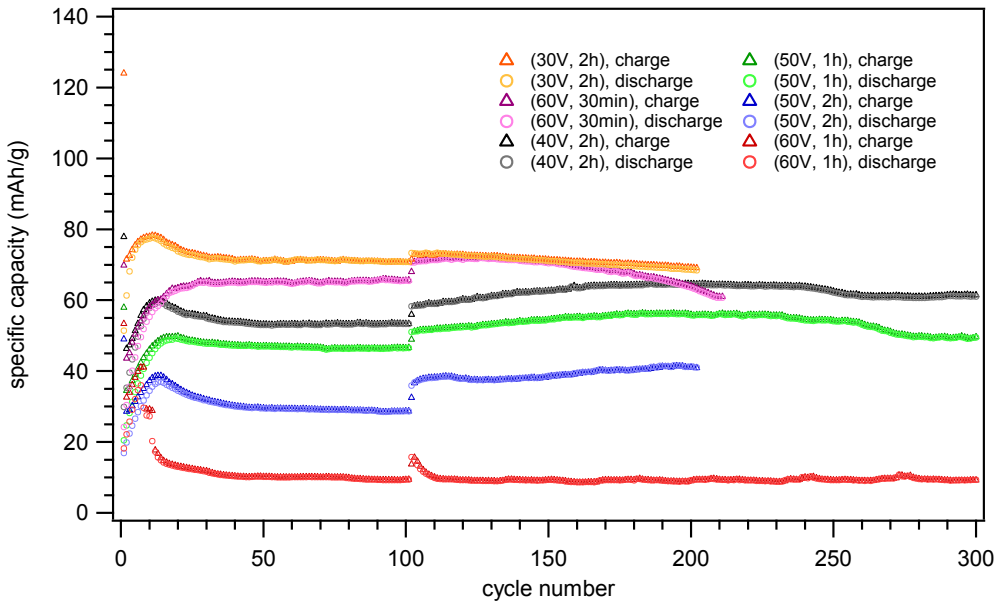

Fig. 35. Specific capacity as a function of the cycle number for titania nanotubes grown by anodization under different conditions. The tubes were cleaned by rinsing with distilled water and dried with compressed air after anodization. For the first 100 cycles sodiation/de-sodiation was done at 50 mA/g followed by cycling at 25 mA/g for the next 100 or 200 times. Potential range: 0.8-2 V vs. Na^+/Na.

Table 4 summarizes the experimentally determined specific capacity values for the samples grown by anodization under different conditions. The data were taken from the 50^{th} cycle representing cycling at 50 mA/g as well as from the 150^{th} cycle standing for the charging/discharging process at 25 mA/g.

Table 4. Experimental specific capacity values for constant current cycling at 50 and 25 mA/g for the samples grown by anodization under different conditions.

anodization voltage	anodization time	specific capacity at 50 mA/g (mAh/g)	specific capacity at 25 mA/g (mAh/g)
30 V	2 h	71.1	71.1
40 V	2 h	53	62.6
50 V	1 h	45	54.5
50 V	2 h	29.5	38.6
60 V	30 min	65	70
60 V	1 h	-	-

As a conclusion nanotubes grown by anodization at 40 V for 2 hours seems to be the best solution with respect to cycling stability over a wide potential range and with respect to specific capacity.

Fig. 36 shows the capacity retention and the low self-discharge behaviour of two test-cells. Within this experiment, the cells were stopped with the nanotubes in the reduced (sodiated) state and rested for variable durations. The remaining capacity was determined by measuring the anodic capacity (corresponding to de-sodiation) that the rested nanotubes were able to supply after the rest period. One cell has already been cycled for 300 times (100 cycles at 50 mA/g and 200 cycles at 25 mA/g) in the potential range of 0.8-2 V vs. Na^+/Na before this experiment, whereas the second one was tested directly after preparation. Both cells contain nanotubes produced by anodization at 40 V for 2 hours as negative electrode material. It can be seen that the capacity drops gradually with increasing resting time in both cases. However, the capacity loss is minimal, since the capacity retention still amounts 99.2% after 240 hours of storage time for the already cycled cell. The freshly prepared sample shows a slightly higher capacity loss with increasing resting time, but the difference to the cycled cell is minimal. No data were obtained for this cell after a resting time of 120 and 240 hours, since the program was stopped due to a power failure.

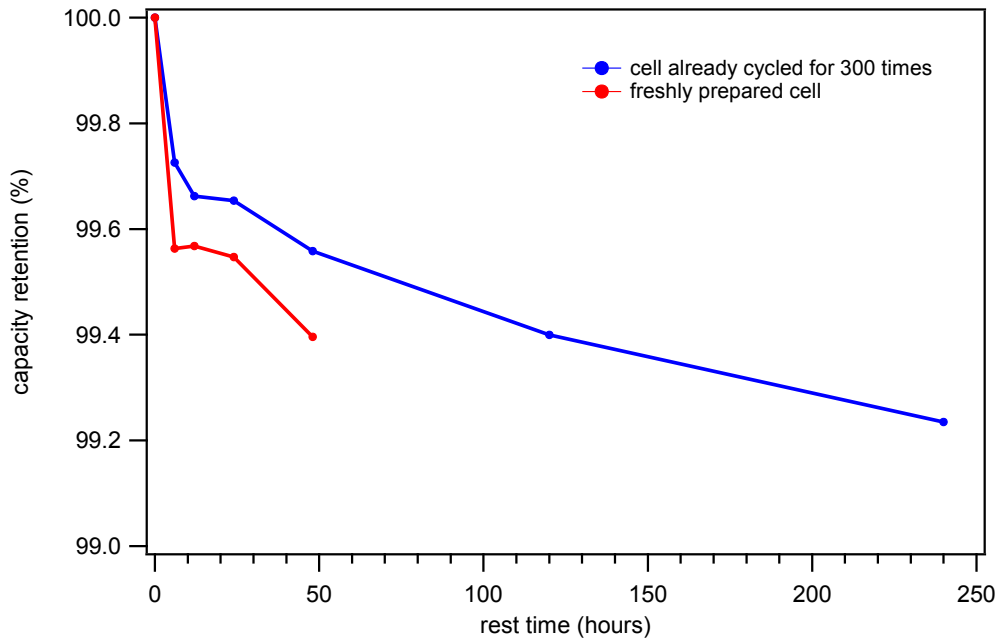

Fig. 36. Capacity retention as a function of resting time. The storage periods were 6, 12, 24, 48, 120 and 240 hours, separately. No data were obtained for the freshly prepared cell after a resting time of 120 and 240 hours, since the program was stopped due to a power failure.

The presence of remnants of the initial oxide layer on the tube tops has already been precisely outlined in section 4.2.1. In order to remove this surface debris different cleaning procedures were applied to the samples directly after anodization, as explained in the experimental part. Fig. 37 shows the cycling performance of these cleaned titania nanotubes grown by anodization at 40 V for 2 hours in a Na half-cell cycled between 0.8-2 V vs. Na^+/Na, first at a rate of 50 mA/g for 100 times, then at 25 mA/g for another 100 times. 1 M $NaClO_4$ in propylene carbonate was used as electrolyte. The poorest cycling performance in terms of accessible specific capacity at a rate of 50 mA/g can be observed for the tubes immersed in ethanol for 1 hour after anodization and dried on air (B5). This sample shows indeed higher capacity values, when cycling was carried out at a lower current, however no good cycling stability was observed. Not much of a difference in the achievable capacities at higher kinetics can be noticed, when the nanotubes were only rinsed with distilled water and ethanol alternately (B2) or when the sample was additionally ultrasonically cleaned for 15 seconds in distilled water (B3). Only at lower cycling rates slightly higher capacity values can be obtained for the ultrasonically cleaned sample. Longer ultrasonic treatment for one minute (B4), however, apparently leads to a partial removal of surface debris making more nanotubes available for the sodium intercalation process, because higher capacities can be reached. However, these titania nanotubes do not show fully reversible Na insertion for all cycles and the capacity values

also fade from the 130th cycle. Since this sample showed a partial separating of the marginal tubes from the underlying titanium substrate after extended ultrasonic treatment, it may be that this nanotube layer is not that stable upon cycling. As apparent from Fig. 37 rinsing only with distilled water (B1) is more effective than washing with distilled water and ethanol alternately (B2).

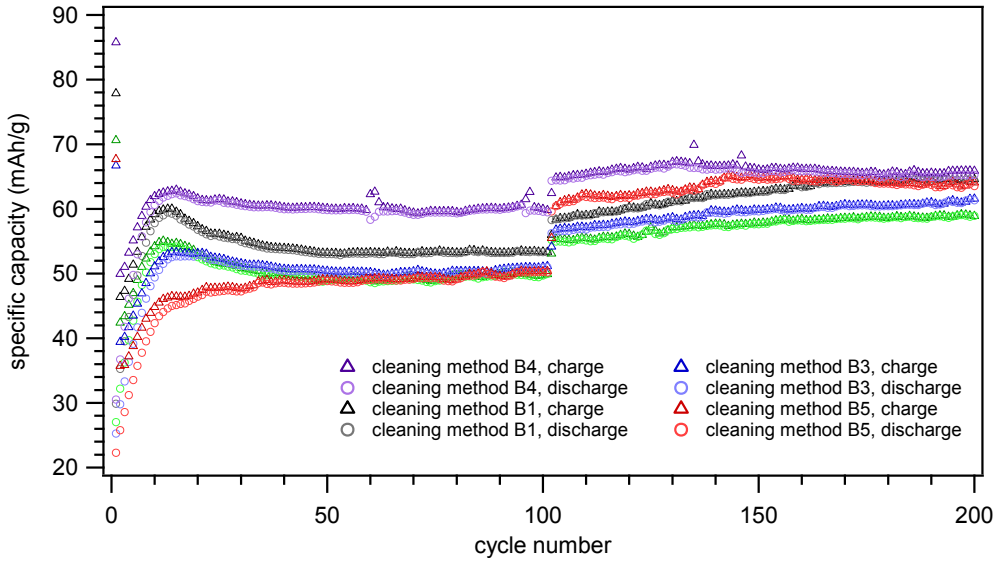

Fig. 37. Cycling performance of titania nanotubes grown by anodic oxidation at 40 V for 2 hours after different cleaning procedures have been applied. Cycling was done in a Na half-cell cycled using 1 M $NaClO_4$ in propylene carbonate as electrolyte first at a rate of 50 mA/g for 100 times, then at 25 mA/g for another 100 times in the potential range of 0.8-2 V vs. Na^+/Na.

Also a two-step anodization procedure was performed, as described in the experimental part. Fig. 38 shows the specific capacity as a function of the cycle number for samples grown by a one-step and two-step anodization after galvanostatic cycling in a sodium half-cell using 1 M $NaClO_4$ in PC as electrolyte, first at 50 mA/g for 100 times, then at 25 mA/g for the next 100 times in the potential range of 0.8-2 V vs. Na^+/Na. It can be seen that higher capacity values can be obtained by a repeated anodization of the titanium substrate. This sample also shows a continuous increase of the capacity values with proceeding cycle number at a current rate of 25 mA/g. According to the literature (see Ref. [92]), a two-step anodic oxidation of Ti leads to the formation of highly and regularly ordered as well as close-packed nanotubes throughout the layer. This improved quality of the tube structure may have a positive influence on the sodium intercalation process resulting in higher capacity values.

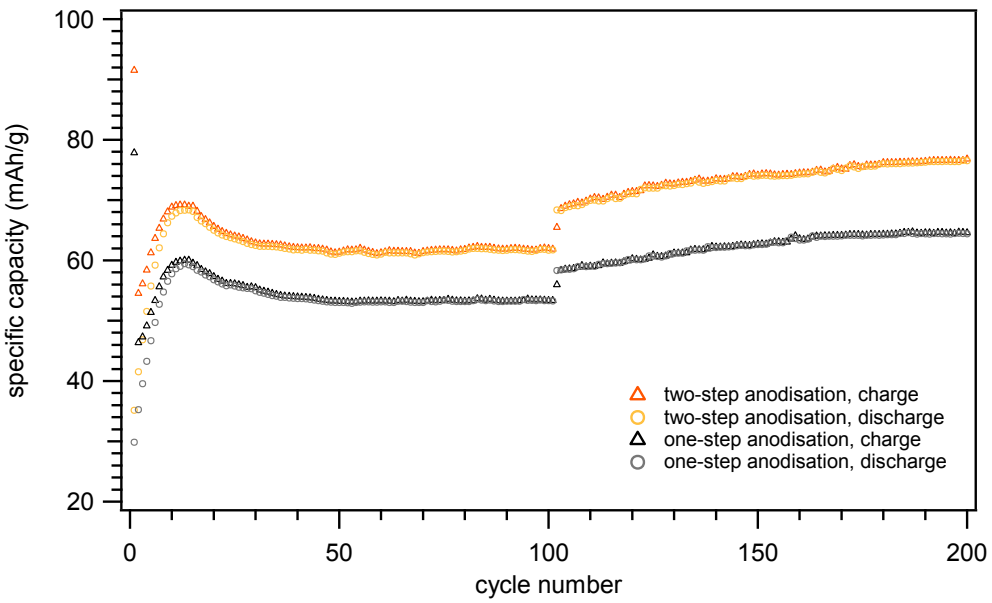

Fig. 38. Specific capacity as a function of the cycle number for samples grown by a one-step and two-step anodization after galvanostatic cycling in a sodium half-cell using 1 M $NaClO_4$ in PC as electrolyte first at 50 mA/g for 100 times, then at 25 mA/g for the next 100 times in the potential range of 0.8-2 V vs. Na^+/Na.

4.4.2.2 Influence of the Electrolyte

Since the electrochemical performance of a cell also depends on the used electrolyte composition, additional galvanostatic cycling experiments were carried out in a sodium half-cell using 0.6 M $NaPF_6$ in a 3:7 ethylene carbonate:dimethyl carbonate mixture as electrolyte. Fig. 39 illustrates the corresponding specific capacities as a function of the cycle number for titania nanotubes produced by anodization at different voltages and times after constant current cycling, first at 50 mA/g for 100 times, then at 25 mA/g for the next 100 times in the potential range of 0.8-2 V vs. Na^+/Na. Comparing the developing of the charge and discharge capacities for the first few cycles for the cells comprising 1 M $NaClO_4$ in PC (Fig. 35) and 0.6 M $NaPF_6$ in EC:DMC (3:7) as electrolyte, it can be seen that the irreversible reactions are more extended for the $NaPF_6$ in EC:DMC mixture. Moreover, no stabilisation of the specific capacity values can be observed, when cycling was done at a rate of 50 mA/g. Only at lower kinetics stable specific capacities can be obtained. As apparent from Fig. 39, also no significant capacities can be achieved for the titania nanotubes anodized at 60 V for 1 h using 0.6 M $NaPF_6$ in a 3:7 EC:DMC mixture. It can be observed that, for the TiO_2 nanotubes grown by anodic oxidation at 30 V and 40 V for 2 hours, higher values can be obtained in $NaPF_6$ in EC:DMC electrolytes when cycled at a rate of 25 mA/g. Capacities of 79.8 mAh/g for the 30 V anodization and 66.1 mAh/g for the 40 V were determined. However, at 50 mA/g the capacities are lower than for $NaClO_4$ in PC. For the sample anodized at 50 V for 2 h similar results can be observed,

27.3 mAh/g at 50 mA/g and 38.1 mAh/g at a current of 25 mA/g. Surprisingly, the titania nanotubes produced at 50 V for 1 h and 60 V for 30 min show the poorest electrochemical performance in terms of cycling stability and accessible specific capacities, when 0.6 M $NaPF_6$ in a 3:7 EC:DMC mixture instead of 1 M $NaClO_4$ in PC is used as electrolyte. The half-cell based on tubes anodized at 60 V for 30 min delivers just a reversible capacity of 31.9 mAh/g at 50 mA/g and 41.3 mAh/g at 25 mA/g compared to 65 mAh/g and 70 mAh/g at the same currents for the cell comprising $NaClO_4$ in PC as electrolyte. For the sample produced by anodization at 50 V for 1 h specific capacity values of 29.2 mAh/g at higher kinetics and 39.6 mAh/g at a rate of 25 mA/g can be reached, whereas the cell cycled in 1 M $NaClO_4$ in propylene carbonate offers capacities of 45 mAh/g and 54.5 mAh/g.

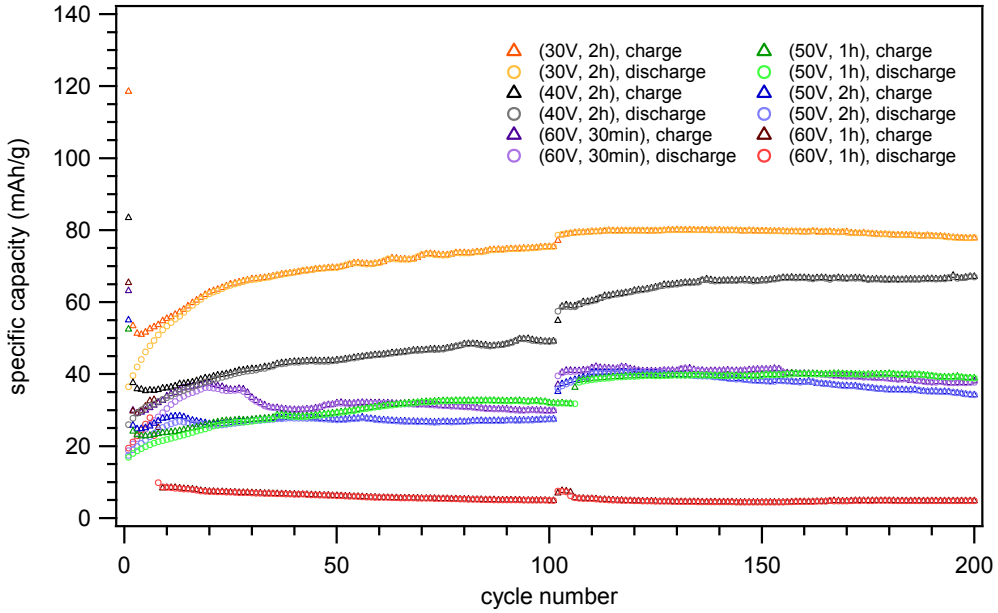

Fig. 39. Specific capacity as a function of the cycle number for titania nanotubes grown by anodization under different conditions. The tubes were cleaned by rinsing with distilled water and drying with compressed air after anodization. Galvanostatic cycling was done in sodium half-cells using 0.6 M $NaPF_6$ in a 3:7 ethylene carbonate:dimethyl carbonate mixture as electrolyte at 50 mA/g for the first 100 times followed by charging/discharging at 25 mA/g for the next 100 times in the potential range of 0.8-2 V vs. Na^+/Na.

Table 5 summarizes the achieved specific capacity values for the samples grown by anodization under different conditions after galvanostatic cycling in a Na half-cell using 0.6 M $NaPF_6$ in a 3:7 EC:DMC mixture as electrolyte. The data were taken from the 50^{th} cycle representing cycling at 50 mA/g as well as from the 150^{th} cycle standing for sodiation/de-sodiation at 25 mA/g.

Table 5. Achieved specific capacity values for constant current cycling at 50 and 25 mA/g for the samples grown by anodization under different conditions after galvanostatic cycling in a Na half-cell using 0.6 M $NaPF_6$ in a 3:7 EC: DMC mixture as electrolyte.

anodization voltage	anodization time	specific capacity at 50 mA/g (mAh/g)	specific capacity at 25 mA/g (mAh/g)
30 V	2 h	69.6	79.8
40 V	2 h	43.6	66.1
50 V	1 h	29.2	39.6
50 V	2 h	27.3	38.1
60 V	30 min	31.9	41.3
60 V	1 h	-	-

What also should be mentioned is that the cells swell upon cycling, when 0.6 M $NaPF_6$ in EC:DMC is used as electrolyte. This observation may be explained by a possible evaporation of the DMC component, since dimethyl carbonate is much more volatile than EC or PC. As a consequence, the contact between the electrodes may get lost resulting in potential cycling instabilities and losses for advanced cycle numbers.
As a conclusion, considering all results, 1 M $NaClO_4$ in PC seems to be a more attractive electrolyte for titania nanotubes-based sodium-ion negative electrode materials, when cycling was done at 50 mA/g and 25 mA/g in the potential range of 0.8-2 V vs. Na^+/Na.

4.4.2.3 Influence of the Potential Limits

To study the influence of lower potentials on the cycling performance of titania nanotubes in a Na half-cell using 1 M $NaClO_4$ in PC as electrolyte, galvanostatic cycling investigations were performed setting the sodiation cut-off potential to 0.1 V vs. Na^+/Na. Following the electrochemical cycling experiments between 0.8 and 2 V vs. Na^+/Na, cycling was done within the potential range of 0.1-2 V vs. Na^+/Na, first at 50 mA/g for 100 cycles, then at 25 mA/g for another 100 cycles utilizing the same cells (Fig. 40). It can be seen that much higher specific capacities can be obtained for the first few cycles, when the potential limit is set to 0.1 V vs. Na^+/Na in comparison to the values that can be achieved after galvanostatic cycling in the potential range of 0.8-2 V vs. Na^+/Na (see Fig. 35). The reason for that may be that at lower potentials more sites can be occupied by sodium, since also less accessible sites are available for the insertion of Na ions. This finding is in good agreement with the results observed by cyclic voltammetry (see section

4.4.1). However, these higher specific capacity values are reached at the expense of cycling stability and reversible sodium intercalation. It can be observed that the capacities fade gradually for the following cycles for tubes produced by anodization at 50 V for 1 h and 2 h and at 40 V for 2 h, while for the sample anodized at 30 V for 2 hours no significant capacity can be achieved after the 20th cycle. The reasons for the poor capacity retention, when the sodiation cut-off potential is set to 0.1 V vs. Na^+/Na, may be related to ageing of the cell (since the samples have already done 200 or 300 cycles), electrolyte decomposition and/or more irreversible reactions. Results from the SEM investigation on cycled samples showed the presence of a layer on the tube tops of the sample charged to a potential limit of 0.1 V vs. Na^+/Na. Furthermore, EDX analysis pointed out that this Na-rich layer probably consists of electrolyte decomposition products, as already mentioned in section 4.2.2. Moreover, the appearance of two reduction peaks, which are associated with electrolyte degradation and formation of a layer, could be observed by cyclic voltammetry (section 4.4.1). Considering all these findings it can be assumed that cycling between 0.1-2 V vs. Na^+/Na results in poor capacity retention and high irreversibility due to electrolyte decomposition and the resultant formation of a layer on the tube tops.

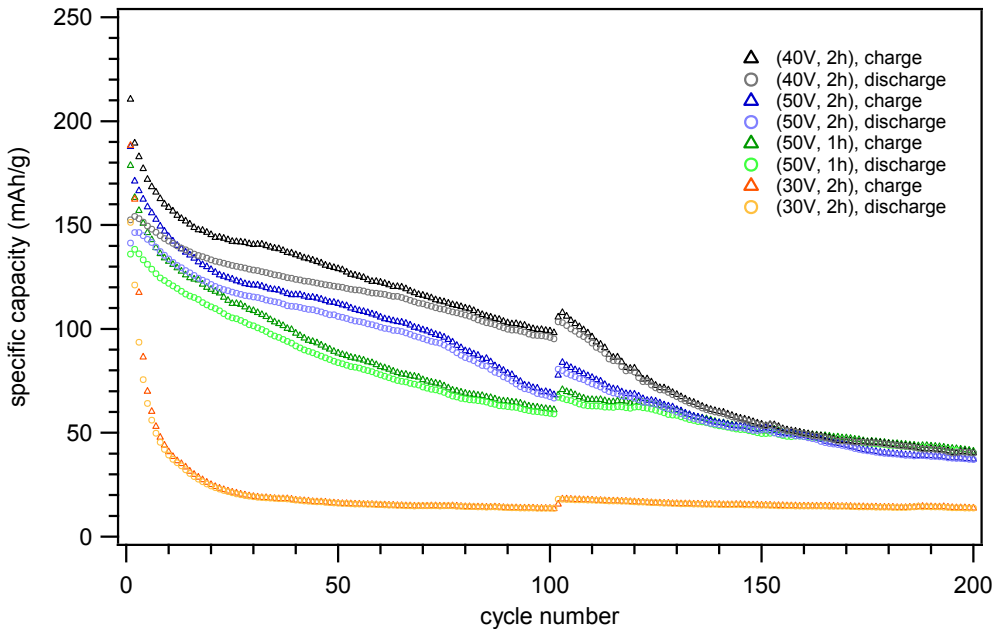

Fig. 40. Specific capacity as a function of the cycle number for titania nanotubes grown by anodization under different conditions. Galvanostatic cycling was done in sodium half-cells using 1 M $NaClO_4$ in PC as electrolyte at 50 mA/g for the first 100 times followed by discharging/charging at 25 mA/g for the next 100 times in the potential range of 0.1-2 V vs. Na^+/Na. The same cells were previously cycled for 200 or 300 times between 0.8-2 V vs. Na^+/Na.

To show the influence of the cell's ageing on the capacity fade, a galvanostatic cycling experiment to a lower potential limit of 0.1 V vs. Na^+/Na was also performed on a freshly assembled cell. Fig. 41 shows the corresponding cycling behaviour of the new cell (b) in comparison to a previously cycled one (a). It can be seen that the capacity also gradually decreases in case of the freshly prepared cell, however, much slower compared to the cell that has been already cycled for 300 times. This result indicates that electrolyte decomposition and irreversible reactions are primarily responsible for the capacity lost, but progressive ageing of the cell enhances the decrease of the capacity values.

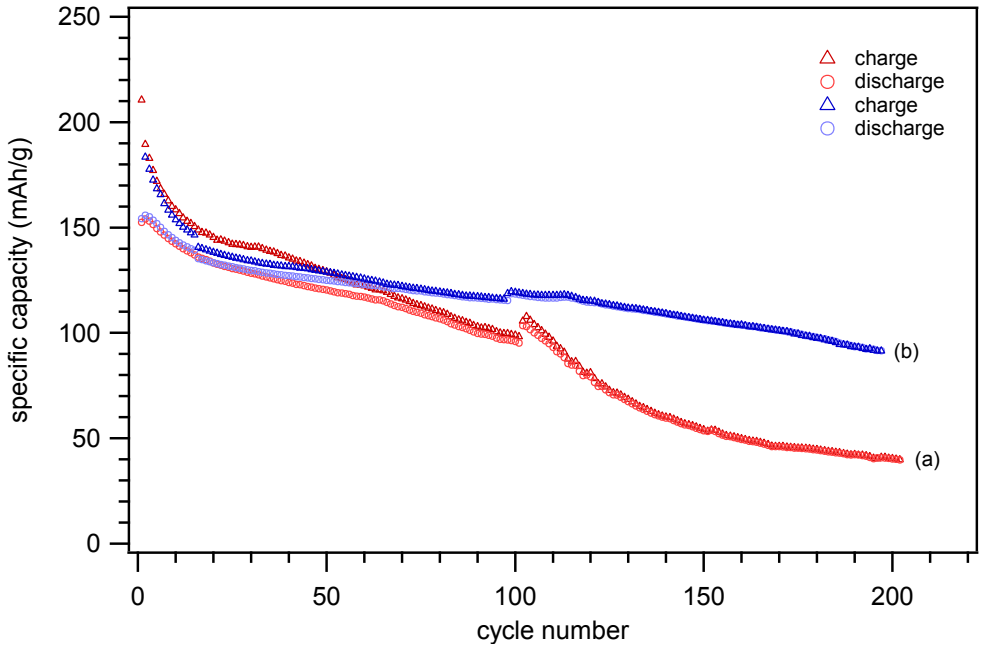

Fig. 41. Cycling performance of a freshly prepared (a) and a previously cycled cell (b) after galvanostatic cycling in a sodium half-cell using 1 M $NaClO_4$ in PC as electrolyte, first at 50 mA/g for 100 times, then at 25 mA/g for the next 100 times in the potential range of 0.1-2 V vs. Na^+/Na. Both cells contain nanotubes produced by anodization at 40 V for 2 hours.

The impact of a lower potential limit of 0.1 V on the cycling performance of titania nanotubes were also investigated for cells using 0.6 M $NaPF_6$ in a 3:7 EC:DMC mixture as electrolyte (Fig. 42). Also, in this case, higher specific capacities can be achieved at the beginning, however a capacity loss of more than 70% occurs within the next 50 cycles.

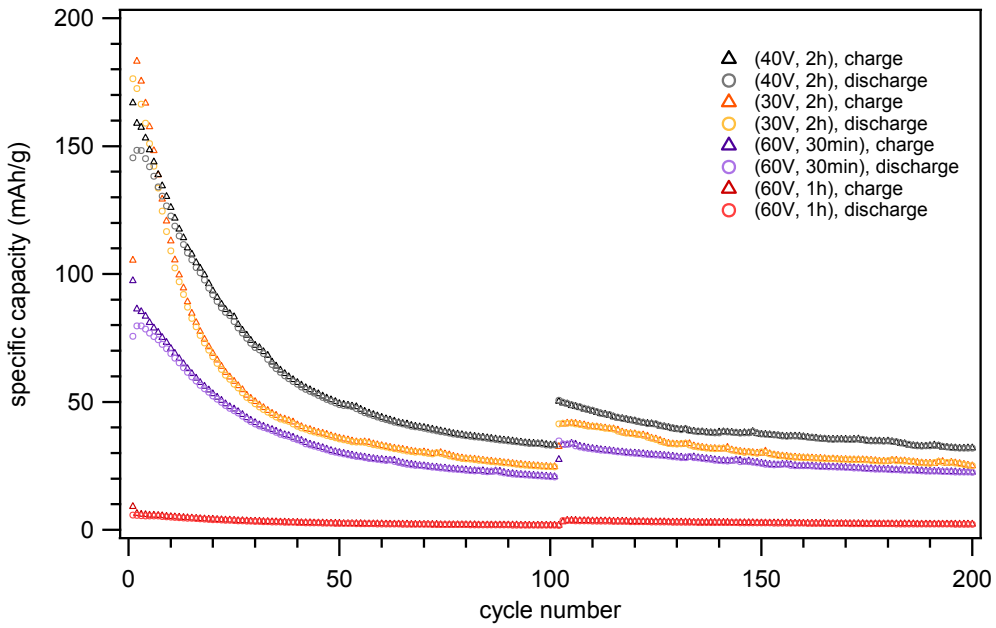

Fig. 42. Specific capacity as a function of the cycle number for titania nanotubes grown by anodization under different conditions. Galvanostatic cycling was done in sodium half-cells using 0.6 M $NaPF_6$ in a 3:7 EC: DMC mixture as electrolyte at 50 mA/g for the first 100 times followed by discharging/charging at 25 mA/g for the next 100 times in the potential range of 0.1-2 V vs. Na^+/Na. The same cells were previously cycled for 200 times between 0.8-2 V vs. Na^+/Na.

4.4.2.4 Influence of Annealed Nanotubes on the Cycling Performance

According to the XRD results shown in section 4.3.2, heat treatment of the nanotubes at 300 °C and 350 °C in argon as well as in air converts the originally amorphous tubes to crystalline anatase structures. The reversible Na ion intercalation in such anatase TiO_2 nanotubes was studied by means of galvanostatic cycling in a sodium half-cell at current rates of 50 mA/g, 25 mA/g and 12.5 mA/g in the potential range of 0.1-2 V vs. Na^+/Na and 0.8-2 V vs. Na^+/Na. 1 M $NaClO_4$ in propylene carbonate was used as electrolyte. Fig. 43 and 44 present the cycling performance of a sample annealed at 350 °C for 2 hours in argon compared to an as-anodized sample. It can be seen that no significant capacities can be achieved for the anatase nanotubes, neither in the potential range of 0.8-2 V vs. Na^+/Na (Fig. 43) nor between 0.1-2 V vs. Na^+/Na (Fig. 44). Based on this result it can be stated that crystalline anatase phases cannot undergo significant sodium ion intercalation and that amorphous nanotubes seem to be the best choice in terms of capacity.

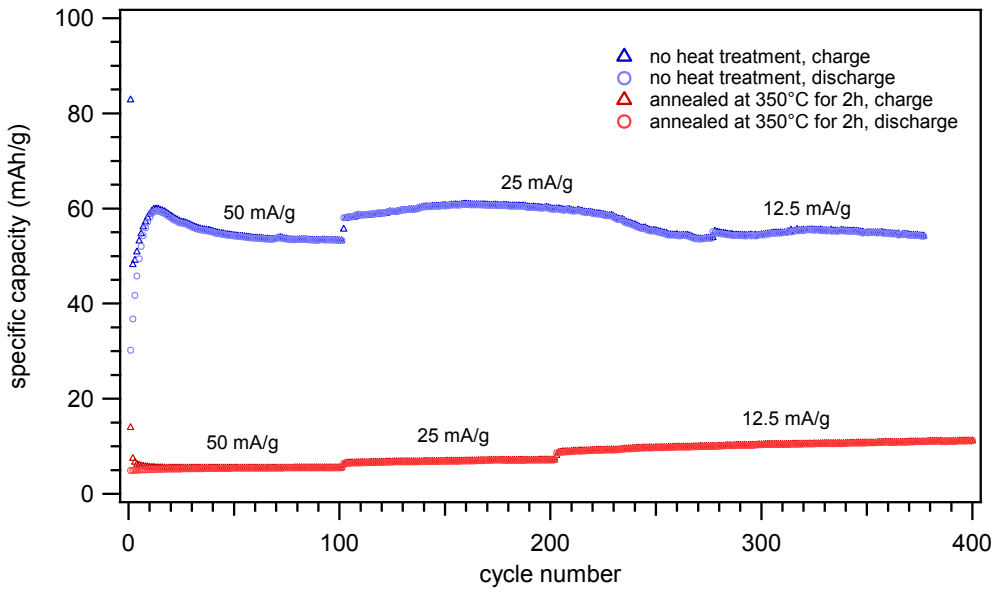

Fig. 43. Specific capacity as a function of the cycle number for a sample annealed at 350 °C for 2 hours in argon and an as-anodized sample after galvanostatic cycling in a sodium half-cell at current rates of 50 mA/g, 25 mA/g and 12.5 mA/g in the potential range of 0.8-2 V vs. Na^+/Na. 1 M $NaClO_4$ in propylene carbonate was used as electrolyte. The nanotubes formed at 40 V for 1 hour were ultrasonically cleaned in distilled water for 15 seconds after anodization.

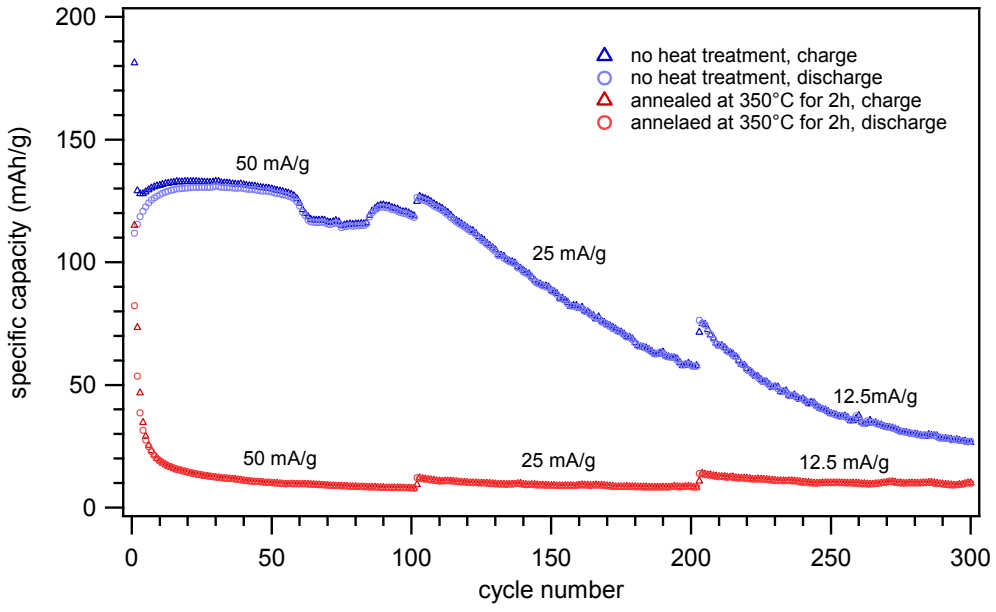

Fig. 44. Specific capacity as a function of the cycle number for a sample annealed at 350 °C for 2 hours in argon and an as-anodized sample after galvanostatic cycling in a sodium half-cell at current rates of 50 mA/g, 25 mA/g and 12.5 mA/g in the potential range of 0.1-2 V vs. Na^+/Na. 1 M $NaClO_4$ in propylene carbonate was used as electrolyte. The nanotubes formed at 40 V for 1 hour were ultrasonically cleaned in distilled water for 15 seconds after anodization.

4.4.2.5 Cycling Behaviour of Titania Nanotubes after Electrodeposition of Sn

From the SEM images in section 4.2.3 it is apparent that electrodeposition of Sn using approach 1-4 just results in a precipitation of tin particles on the surface of the nanotubes. Fig. 45 shows the electrochemical performance of these NTs after galvanostatic cycling between 0.1-2 V vs. Na^+/Na at a rate of 50 mA/g and 25 mA/g in a sodium half-cell using 1 M $NaClO_4$ in PC as electrolyte. Comparing these results with the findings shown in Fig. 41 no influence of tin in terms of achievable capacity and cycling stability can be observed. However, more research has to be done on this field in order to be on a competitive basis with the current Li-ion battery systems.

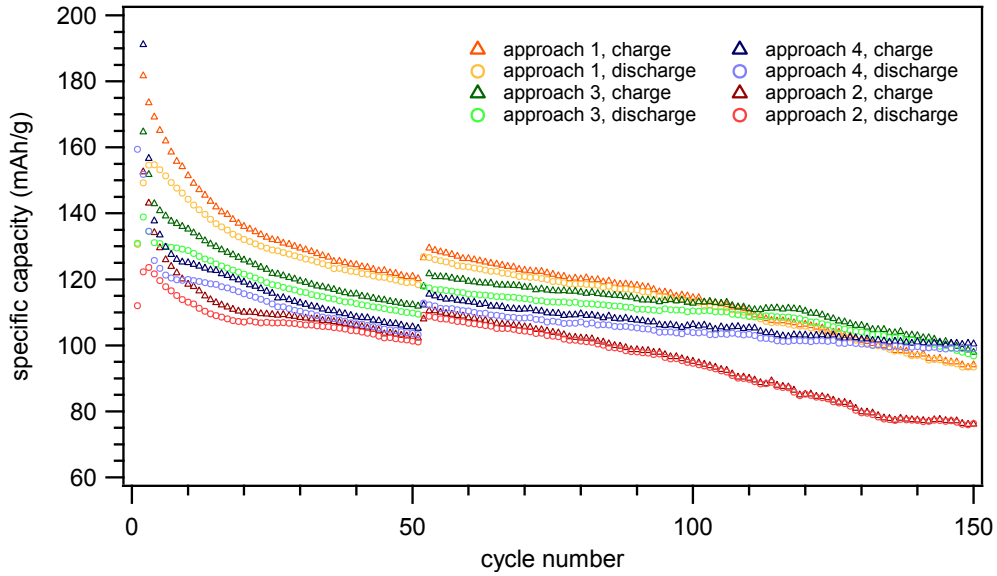

Fig. 45. Specific capacity as a function of the cycle number for titania nanotubes modified with Sn. Cycling was done in sodium half-cells using 1 M $NaClO_4$ in PC as electrolyte at 50 mA/g for the first 50 times followed by charging/discharging at 25 mA/g for the next 100 times in the potential range of 0.1-2 V vs. Na^+/Na. The nanotubes formed at 40 V for 2 hours were ultrasonically cleaned in distilled water for 15 seconds prior to electrodeposition of tin.

4.5 EIS Results

4.5.1 Effect of Electrolyte Additives on the SEI Layer Formation

As described in the experimental section, electrochemical impedance spectroscopy (EIS) experiments on symmetric Na/Na cells were carried out at various times (20 min, 1 hour, 3 hours, 10 hours, 1 day, 2 days, 3 days, 4 days and 5 days after preparation) in order to study the effect of different electrolyte additives on the formation of a passive layer on sodium metal. Fig. 46 shows the equivalent circuit models used to fit the resulting electrochemical impedance data. For the further discussion however only the values of the R1, CPE1 and R2 elements are examined. In these EECs, R1 comprises the electrolyte resistance and R2 is the charge transfer resistance. The capacitance of the double-layer is represented by the constant phase element CPE1.

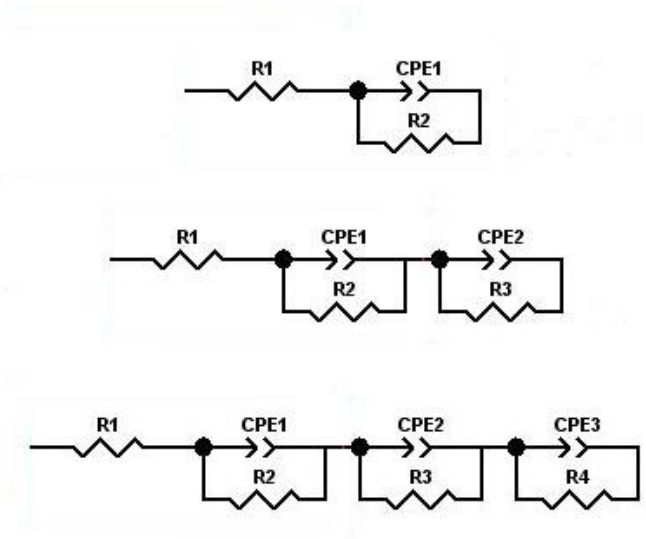

Fig. 46. Equivalent circuit models used to fit the electrochemical impedance data. Only the values of the R1, CPE1 and R2 elements are examined for the further discussion. In these EECs, R1 comprises the electrolyte resistance, R2 is the charge transfer resistance and CPE1 represents the constant phase element that is usually ascribed to the capacitance of the double electrical layer.

Fig. 47 presents the electrolyte resistance as a function of the time using 1 M $NaClO_4$ in PC as electrolyte without and with addition of 1% of the respective additive. It can be seen that all additives have an impact on the resistance of the electrolyte. While the reduction-type additives VC, FEC and VEC decrease R1 compared to no additive, higher values can be found in the case of the isocyanates. Using the carbonate additives the resistance initially increases, but stabilises after approximately 3 hours. The same behaviour can be observed, when no additive is added. The lowest electrolyte resistance and the best stability can be found for the vinylene carbonate additive. Comparing the reaction-type

additives 2,3,4-trifluorphenylisocyanate and 4-fluorphenylisocyanate it can be seen that R1, however initially lower than for no additive, gradually increases with time, when 1% of 4-fluorphenylisocyanate is added. For the 2,3,4-trifluorphenylisocyanate additive R1 varies within a certain range.

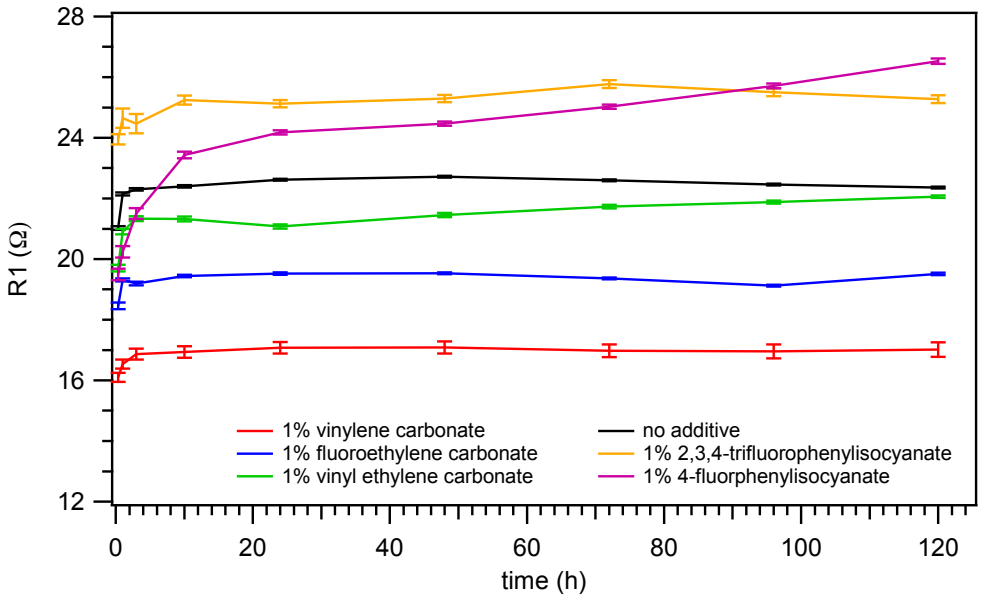

Fig. 47. Electrolyte resistance as a function of time using 1 M $NaClO_4$ in PC as electrolyte without and with addition of 1% of the respective additive.

From the constant phase element two parameters can be obtained, the CPE modulus (CPE1-T) and the CPE exponent (CPE1-P). Fig. 48 shows the variation of the modulus with time in a 1 M solution of $NaClO_4$ in PC with and without addition of additives. It can be seen that without the use of an additive the capacitance initially decreases, but gradually increases after 24 hours due to corrosion of the sodium metal that leads to an increased electrode surface area. In contrast, the addition of 1% of VC, FEC and 2,3,4-trifluorophenylisocyanate to the electrolyte leads to a constant CPE1-T values with time indicating the formation of a layer on the Na metal that inhibits the corrosion process. Using 4-fluorphenylisocyanate as additive the capacitance initially alternates, but stabilises after two days also due to passivation of the metal surface. When 1% of VEC is utilized CPE1-T decreases after 10 hours and stays constant over a short period owing to layer formation. However, after 72 hours a gradual increase of the capacitance can be observed indicating that the passivating film cracks and hence corrosion occurs. Based on these results it can be concluded that VC, FEC and 2,3,4-trifluorophenylisocyanate are effective corrosion inhibitors.

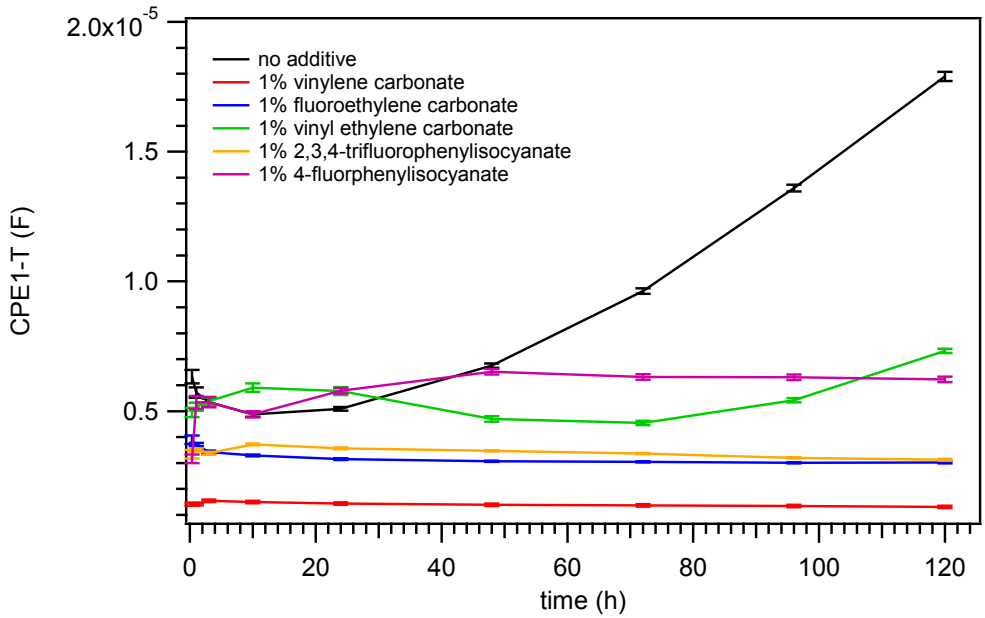

Fig. 48. CPE modulus as a function of time using 1M $NaClO_4$ in PC as electrolyte with and without addition of additives.

In Fig. 49 the corresponding CPE exponent as a function of the time can be observed. For a constant phase element the exponent is always less than one. Since the changes of the exponent values are small in each case, the above-mentioned assumptions concerning layer formation and corrosion can be thus confirmed.

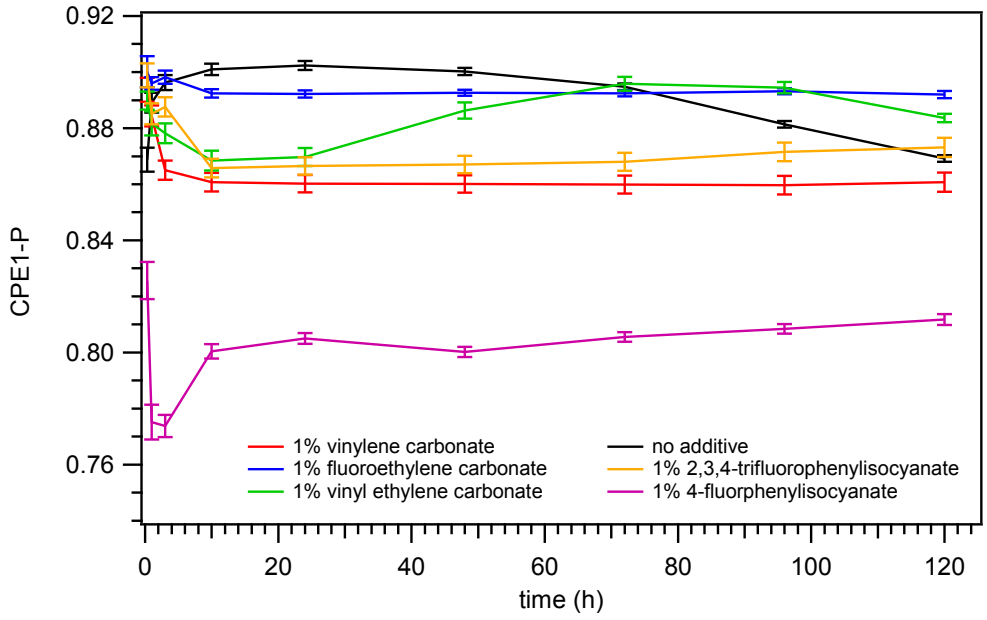

Fig. 49. CPE exponent as a function of time using 1M $NaClO_4$ in PC as electrolyte with and without addition of additives.

Fig. 50 demonstrates the effect of these electrolyte additives on the charge transfer resistance. From these results it is apparent that all additives used lead to an enhancement of the R2 values compared to the resistance without additive, whereupon the highest values can be found for VC. When 1% of VC, FEC or 2,3,4-trifluorophenylisocyanate is added, a remarkably increase of R2 can be observed in the initial period indicating the formation of a less conductive layer on the sodium surface. This correlates well with the above-mentioned findings. However after a period of 24 hours the curves flatten meaning that layer formation occurs mostly during the first day after assembling. The lowest impact on the charge transfer resistance can be observed, when 1% of VEC or 4-fluorphenylisocyanate is present.

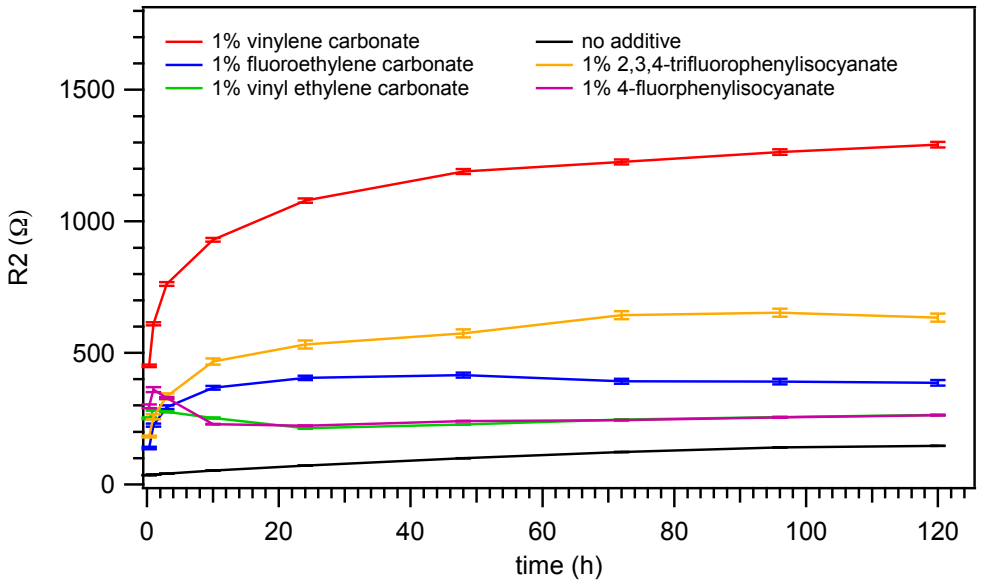

Fig. 50. Charge transfer resistance as a function of time using 1 M $NaClO_4$ in PC as electrolyte without and with addition of 1% of the respective additive.

The same EIS experiments were also investigated using 0.6 M $NaPF_6$ in a 3:7 EC:DMC mixture as electrolyte. Fig. 51 presents the electrolyte resistance as a function of the time without and with addition of 1% of the respective additive. It can be seen that all additives increase R1 compared to the cell containing no additive, whereupon the highest values can be found for the isocyanates. The lowest impact on the electrolyte resistance in contrast can be observed, when 1% of VC is present. Furthermore Fig. 51 shows a stabilisation of the R1 values at around 3 hours with the exception of the 4-fluorphenylisocyanate additive. In this case the resistance initially decreases showing a minimum at 24 hours and finally stabilises at 72 hours.

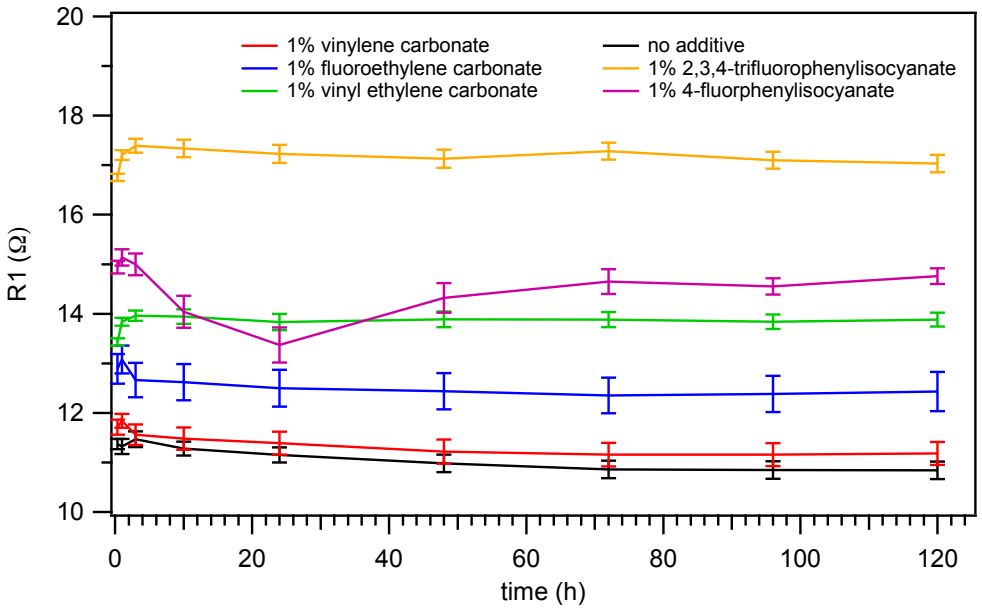

Fig. 51. Electrolyte resistance as a function of time using 0.6 M $NaPF_6$ in a 3:7 EC:DMC mixture as electrolyte without and with addition of 1% of the respective additive.

The variation of the CPE modulus with time can be seen in Fig. 52. Surprisingly the CPE1-T value initially decreases, but stabilises after 10 hours, when no additive is used. This result indicates that the electrolyte itself forms a passivating layer on the sodium metal preventing it from corrosion. Nearly the same behaviour can also be observed with addition of 1% of VC or FEC. Using vinyl ethylene carbonate as additive CPE1-T gradually increases and then stabilises after one day. These stable values as well as the low capacitance suggest that VEC strengthens the layer formed by the electrolyte due to the reduction of its double bond. In contrast in the presence of isocyanates no stable developing of the CPE1-T values can be observed indicating a worsening of the formed layer.

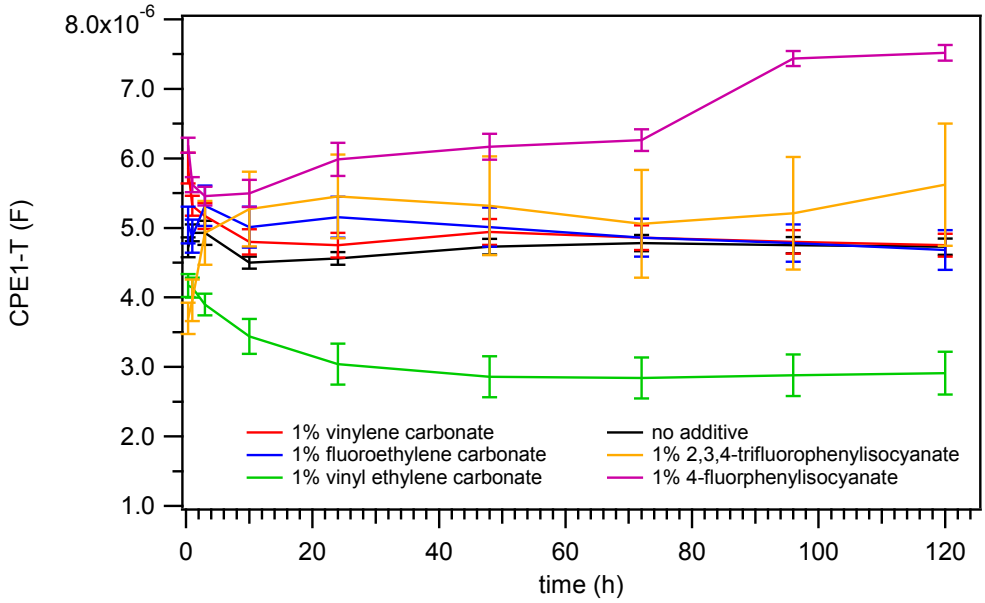

Fig. 52. CPE modulus as a function of time using 0.6 M $NaPF_6$ in a 3:7 EC:DMC mixture as electrolyte with and without addition of additives.

In Fig. 53 the corresponding CPE exponent as a function of the time is shown. The changes of the exponent values are also small in this case confirming that the equivalent circuit used to model the observed behaviour can be used throughout the whole experiment.

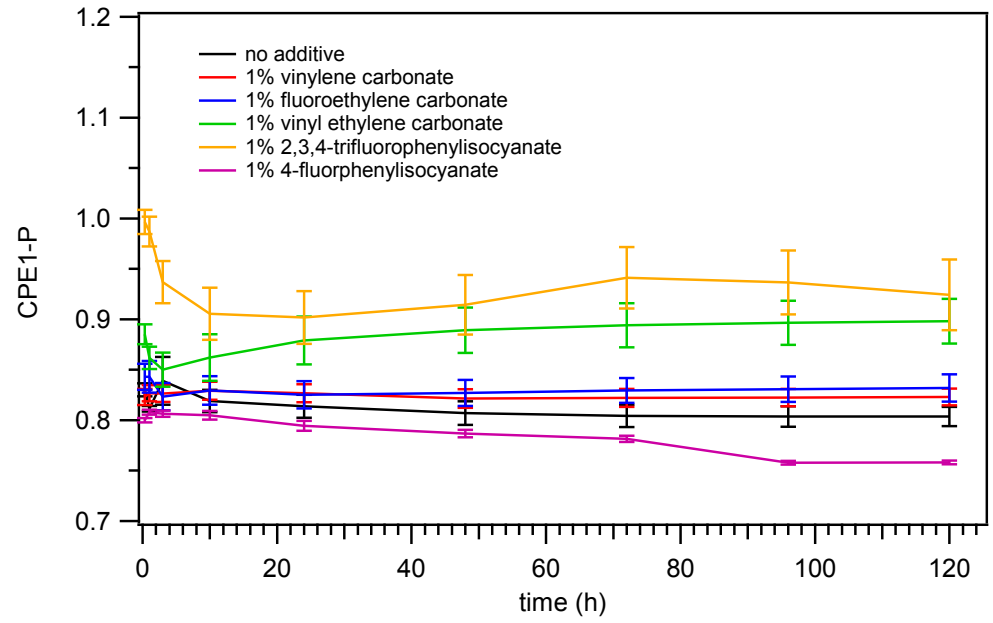

Fig. 53. CPE exponent as a function of time using 0.6 M $NaPF_6$ in a 3:7 EC:DMC mixture as electrolyte with and without addition of additives.

Fig. 54 presents the charge transfer resistance as a function of the time. It can be seen that the additives used have a different impact on the resistance. While FEC, VEC and 2,3,4-trifluoroisocyanate decrease R2 compared to the cell without an additive, higher values can be found in the case of VC and 4-fluorphenylisocyanate. When no additive is used the charge transfer resistance increases during the first 24 hours after assembling, but slightly decrease in the next four days. The same behaviour can be observed in the presence of 4-fluorphenylisocyanate, however higher values for R2 are achieved in this case. For FEC the resistance also increases in the initial period, but stabilises after one day. When 1% of VC is added, R2 gradually grow with time resulting in the highest resistance values. On the contrary, the lowest charge transfer resistance and the best stability can be found for vinyl ethylene carbonate and 2,3,4-trifluoroisocyanate.

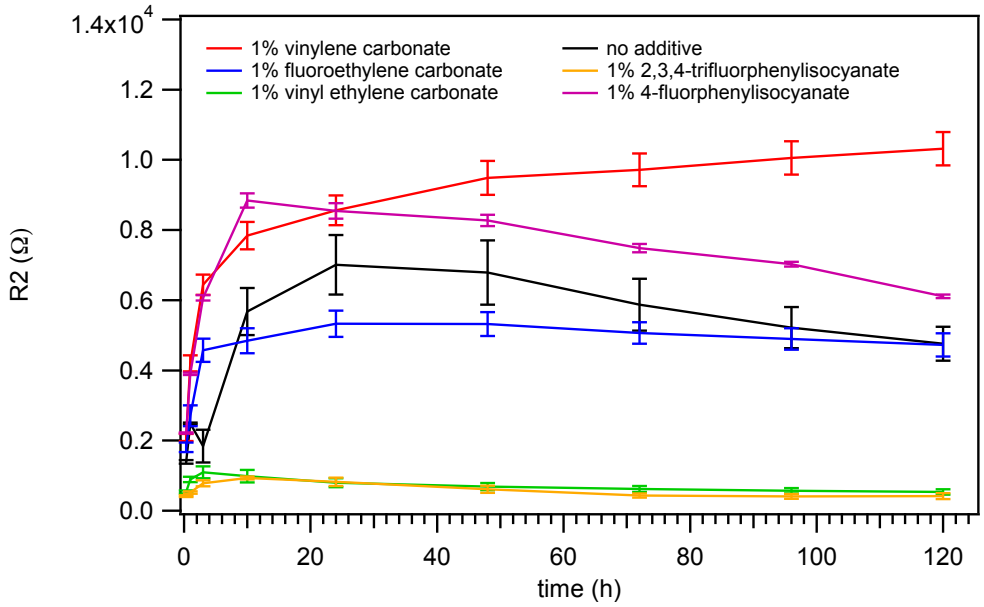

Fig. 54. Charge transfer resistance as a function of time using 0.6 M $NaPF_6$ in a 3:7 EC:DMC mixture as electrolyte without and with addition of 1% of the respective additive.

4.5.2 Chemical Diffusion Coefficient

As described in the experimental part the chemical diffusion coefficient was determined using Chronoamperometry and the corresponding calculations were carried out with the Cottrell equation. When the copper foil was employed as WE a value of $2.63*10^{-7}$ cm^2/s was obtained for the chemical diffusion coefficient.

5 Conclusion and Outlook

In the present work highly parallel self-assembled TiO_2 nanotube layers were successfully formed by anodic oxidation of a Ti foil in a mixed electrolyte containing 97.6% ethylene glycol, 2% distilled water and 0.4% NH_4F. SEM investigations showed that the length of these nanotubes increased with the applied potential at a certain anodization time ranging in thicknesses from ~4.1 μm at 30 V to ~15.1 μm at 40 V for a 2 h anodic oxidation and from ~10.2 μm to ~16.9 μm at 50 V and 60 V respectively when anodization was done for 1 h. Furthermore the applied voltage has also a large effect on the diameter leading to average tube diameters of approximately 70 nm at 30 V, 100 nm at 40 V and 130 nm at 60 V. It could also be seen that the tube tops are partially covered with remnants of the initial layer. Ultrasonic treatment for one minute seems to be most effective in order to remove this surface debris. XRD analysis of these as-anodized samples revealed that the nanotubes are of an amorphous nature after anodic growth and do not crystallize in time. Moreover, no correlation between crystallinity/amorphicity and the anodization voltage could be observed. Annealing of the NTs at 300 °C and 350 °C in argon as well as in air results in a phase transition from the originally amorphous tubes to crystalline anatase structures.

The insertion and extraction of sodium into/from amorphous titania nanotubes was investigated by galvanostatic cycling experiments between 0.8-2 V vs. Na^+/Na in Na half-cells using 1 M $NaClO_4$ in propylene carbonate as electrolyte. High irreversible capacities could be observed on the first cycle that have been attributed to non-reversible sodium intercalation during the first discharging/charging or the formation of a layer on the surface of the tubes. Furthermore, it was observed that the areal capacity depends on the length of the nanotubes. The longer the tubes, the more sites can be occupied by sodium resulting in higher values. Moreover, also a larger diameter contributes to achieve higher areal capacities. Maximum capacity values concerning both areal and specific capacities were obtained for the samples grown by anodization at 60 V for 30 min that showed 65 mAh/g and 70 mAh/g at 50 mA/g and 25 mA/g, respectively. However, taking also the cycling stability into account the best cycling performance can be observed for the tubes grown by anodic oxidation at 40 V for 2 hours delivering specific capacity values of 53 mAh/g at 50 mA/g and 62.6 mAh/g at a rate of 25 mA/g. This cell presents a stable cycling performance for over 300 cycles without significant capacity fade upon cycling. Even after a storage period of 240 hours the capacity loss due to self-discharge was less than 1%. Even higher capacities could be achieved, when these nanotubes were produced by a two-step anodization process due to the improved quality of the tube structure. Furthermore, it was shown that cycling to a potential limit of 0.1 V vs. Na^+/Na leads to

higher specific capacity values during the first few cycles, however at the expense of cycling stability and a loss of reversible sodium intercalation. Electrolyte decomposition as well as the formation of a surface layer consisting of electrolyte degradation products occurs at lower potentials resulting in poor capacity retention and high irreversibility. Galvanostatic cycling investigations were also performed using 0.6 M $NaPF_6$ in a 3:7 EC:DMC mixture as electrolyte. However, it was found that 1 M $NaClO_4$ in PC seems to be a more attractive and suitable electrolyte combination for titania nanotubes-based Na-ion electrodes in terms of cycling behaviour as well as cell stability and safety. Finally, it was figured out that crystalline anatase phases cannot undergo significant Na ion intercalation. SEM and XRD analysis of cycled samples revealed that intercalation of sodium ions into the tubes does not destroy the nanotubular structure and that the NTs remain amorphous upon cycling.

In the final part the effect of different electrolyte additives on the formation of a passivating layer on sodium metal was studied. EIS results demonstrated that the addition of 1% of VC, FEC and 2,3,4-trifluorophenylisocyanate to a 1 M solution of $NaClO_4$ in PC used as electrolyte inhibits corrosion of the Na metal due to formation of a layer on the metal surface. Using a 0.6 M solution of $NaPF_6$ in a 3:7 EC:DMC mixture, a passive layer is formed by the electrolyte itself without addition of an additive. However, in the presence of VEC a strengthening and stabilisation of the already formed layer could be observed.

The sodium chemical diffusion coefficient value determined from chronoamperometry experiments is in the range of $2.63*10^{-7}$ cm^2/s.

To summarize, titania nanotube layers showed good cycling performance when used as negative electrode material in sodium half-cells, but more research has to be done in order to identify the origin of the irreversible capacity losses and consequently evaluate the possibility of further enhancement of the practical specific capacities. One possibility may be the use of TiO_2 nanotubes/Sn composites, which can be fabricated by filling of the tubes with tin. Some preliminary tests on this field have already been carried out in the present work. Unfortunately, Sn-filled NTs could not be obtained so far. With respect to the experiments on additives, also long-term investigations have to be done in order to trace and evaluate the stability of the formed layer over time. Furthermore, the influence of these additives should also be tested in the future on real Na-ion full-cells.

References

1. Slater, M. D., Kim, D., Lee, E. & Johnson, C. S. Sodium-Ion Batteries. *Adv. Funct. Mater.* **23,** 947–958 (2013).

2. Ellis, B. L. & Nazar, L. F. Sodium and sodium-ion energy storage batteries. *Curr. Opin. Solid State Mater. Sci.* **16,** 168–177 (2012).

3. Palomares, V., Casas-Cabanas, M., Castillo-Martínez, E., Han, M. H. & Rojo, T. Update on Na-based battery materials. A growing research path. *Energy Environ. Sci.* **6,** 2312–2337 (2013).

4. Pan, H., Hu, Y.-S. & Chen, L. Room-temperature stationary sodium-ion batteries for large-scale electric energy storage. *Energy Environ. Sci.* **6,** 2338 (2013).

5. Delmas, C., Braconnier, J.-J., Fouassier, C. & Hagemuller, P. Electrochemical intercalation of sodium in NaxCoO2 bronzes. *Solid State Ionics* **3/4,** 165–169 (1981).

6. Lu, Z. & Dahn, J. R. In Situ X-Ray Diffraction Study of P2-Na2/3[Ni1/3Mn2/3]O2. *J. Electrochem. Soc.* **148,** A1225–A1229 (2001).

7. Kitajou, A. *et al.* Novel synthesis and electrochemical properties of perovskite-type NaFeF3 for a sodium-ion battery. *J. Power Sources* **198,** 389–392 (2012).

8. Lee, K. T., Ramesh, T. N., Nan, F., Botton, G. & Nazar, L. F. Topochemical Synthesis of Sodium Metal Phosphate Olivines for Sodium-Ion Batteries. *Chem. Mater.* **23,** 3593–3600 (2011).

9. Recham, N. *et al.* Ionothermal Synthesis of Sodium-Based Fluorophosphate Cathode Materials. *J. Electrochem. Soc.* **156,** A993–A999 (2009).

10. Moreau, P., Guyomard, D., Gaubicher, J. & Boucher, F. Structure and Stability of Sodium Intercalated Phases in Olivine FePO4. *Chem. Mater.* **22,** 4126–4128 (2010).

11. Plashnitsa, L. S., Kobayashi, E., Noguchi, Y., Okada, S. & Yamaki, J. Performance of NASICON Symmetric Cell with Ionic Liquid Electrolyte. *J. Electrochem. Soc.* **157,** A536–A543 (2010).

12. Hong, S. Y. *et al.* Charge carriers in rechargeable batteries: Na ions vs. Li ions. *Energy Environ. Sci.* **6,** 2067–2081 (2013).

13. Alcántara, R., Lavela, P., Ortiz, G. F. & Tirado, J. L. Carbon Microspheres Obtained from Resorcinol-Formaldehyde as High-Capacity Electrodes for Sodium-Ion Batteries. *Electrochem. Solid-State Lett.* **8,** A222–A225 (2005).

14. Komaba, S. *et al.* Electrochemical Na insertion and solid electrolyte interphase for hard-carbon electrodes and application to Na-ion batteries. *Adv. Funct. Mater.* **21,** 3859–3867 (2011).

15. Ponrouch, A., Goni, A. R. & Palacín, M. R. High capacity hard carbon anodes for sodium ion batteries in additive free electrolyte. *Electrochem. commun.* **27,** 85–88 (2013).

16. Oh, S.-M. *et al.* An advanced sodium-ion rechargeable battery based on a tin–carbon anode and a layered oxide framework cathode. *Phys. Chem. Chem. Phys.* **15,** 3827–3833 (2013).

17. Xiao, L. *et al.* High capacity , reversible alloying reactions in SnSb/C nanocomposites for Na-ion battery applications. *Chem. Commun.* **48,** 3321–3323 (2012).

18. Baggetto, L. *et al.* Characterization of sodium ion electrochemical reaction with tin anodes : Experiment and theory. *J. Power Sources* **234,** 48–59 (2013).

19. Datta, M. K. *et al.* Tin and graphite based nanocomposites : Potential anode for sodium ion batteries. *J. Power Sources* **225,** 316–322 (2013).

20. Lin, Y.-M. *et al.* Sn–Cu Nanocomposite Anodes for Rechargeable Sodium-Ion Batteries. *Appl. Mater. Interfaces* **5,** 8273–8277 (2013).

21. Paul, R. A. *et al.* Nanocolumnar Germanium Thin Films as a High-Rate Sodium-Ion Battery Anode Material. *J. Phys. Chem. C* **117,** 18885–18890 (2013).

22. Huang, J. P. *et al.* Electrochemical sodium storage of TiO2(B) nanotubes for sodium ion batteries. *RSC Adv.* **3,** 12593 (2013).

23. Park, S. Il, Gocheva, I., Okada, S. & Yamaki, J. Electrochemical Properties of NaTi2(PO4)3 Anode for Rechargeable Aqueous Sodium-Ion Batteries. *J. Electrochem. Soc.* **158,** A1067–A1070 (2011).

24. González, J. R., Alcántara, R., Ortiz, G. F., Nacmiento, F. & Tirado, J. L. Controlled Growth and Application in Lithium and Sodium Batteries of High-Aspect-Ratio, Self-Organized Titania Nanotubes. *J. Electrochem. Soc.* **160,** A1390–A1398 (2013).

25. Xiong, H., Slater, M. D., Balasubramanian, M., Johnson, C. S. & Rajh, T. Amorphous TiO2 Nanotube Anode for Rechargeable Sodium Ion Batteries. *J. Phys. Chem. Lett.* **2,** 2560–2565 (2011).

26. Senguttuvan, P., Rousse, G., Seznec, V., Tarascon, J.-M. & Palacín, M. R. Na2Ti3O7 : Lowest Voltage Ever Reported Oxide Insertion Electrode for Sodium Ion Batteries. *Chem. Mater.* **23,** 4109–4111 (2011).

27. Armstrong, A. R., Armstrong, G., Canales, J. & Bruce, P. G. TiO 2–B nanowires as negative electrodes for rechargeable lithium batteries. *J. Power Sources* **146,** 501–506 (2005).

28. Lindsay, M. J. *et al.* Anodic titania films as anode materials for lithium ion batteries. *Electrochim. Acta* **52,** 6401–6411 (2007).

29. Bruce, P. G., Scrosati, B. & Tarascon, J.-M. Nanomaterials for Rechargeable Lithium Batteries **. *Angew. Chem. Int. Ed. Engl.* **47,** 2930–2946 (2008).

30. Kavan, L., Kratochvilová, K. & Grätzel, M. Study of nanocrystalline TiO2(anatase) electrode in the accumulation regime. *J. Electroanal. Chem.* **394,** 93–102 (1995).

31. Wu, L., Buchholz, D., Bresser, D., Chagas, L. G. & Passerini, S. Anatase TiO2 nanoparticles for high power sodium-ion anodes. *J. Power Sources* **251,** 379–385 (2014).

32. Ponrouch, A., Marchante, E., Courty, M., Tarascon, J.-M. & Palacín, M. R. In search of an optimized electrolyte for Na-ion batteries. *Energy Environ. Sci.* **5,** 8572–8583 (2012).

33. Linden, D. & Reddy, T. *Handbook of batteries*. (McGraw-Hill, 2002). at <http://m.doko.vn/tai-lieu/handbook-of-batteries-1737272>

34. Ge, P. & Fouletier, M. ELECTROCHEMICAL INTERCALATION OF SODIUM IN GRAPHITE. *Solid State Ionics* **28-30,** 1172–1175 (1988).

35. DiVincenzo, D. P. & Mele, E. J. Cohesion and structure in stage-1 graphite intercalation compounds. *Phys. Rev. B* **32,** 2538–2553 (1985).

36. Doeff, M. M., Ma, Y., Visco, S. J. & De Jonghe, L. C. Electrochemical insertion of sodium into carbon. *J. Electrochem. Soc.* **140,** L169–L170 (1993).

37. Alcántara, R., Mateos, J. M. J. & Tirado, J. L. Negative electrodes for lithium-and sodium-ion batteries obtained by heat-treatment of petroleum cokes below 1000°C. *J. Electrochem. Soc.* **149,** A201–A205 (2002).

38. Thomas, P. & Billaud, D. Sodium electrochemical insertion mechanisms in various carbon fibres. *Electrochim. Acta* **46,** 3359–3366 (2001).

39. Alcántara, R., Jiménez-Mateos, J. M., Lavela, P. & Tirado, J. L. Carbon black : a promising electrode material for sodium-ion batteries. *Electrochem. commun.* **3,** 639–642 (2001).

40. Dubois, M., Naji, A. & Billaud, D. Electrochemical insertion of alkaline ions into polyparaphenylene: effect of the crystalline structure of the host material. *Electrochim. Acta* **46,** 4301–4307 (2001).

41. Cao, Y. *et al.* Sodium ion insertion in hollow carbon nanowires for battery applications. *Nano Lett.* **12,** 3783–3787 (2012).

42. Tang, K. *et al.* Hollow Carbon Nanospheres with Superior Rate Capability for Sodium-Based Batteries. *Adv. Energy Mater.* **2,** 873–877 (2012).

43. Wang, H. *et al.* Nitrogen-Doped Porous Carbon Nanosheets as Low-Cost , High-Performance Anode Material for Sodium-Ion Batteries. *ChemSusChem Commun.* **6,** 56–60 (2013).

44. Wenzel, S., Hara, T., Janek, J. & Adelhelm, P. Room-temperature sodium-ion batteries : Improving the rate capability of carbon anode materials by templating strategies †. *Energy Environ. Sci.* **4,** 3342–3345 (2011).

45. Stevens, D. A. & Dahn, J. R. High Capacity Anode Materials for Rechargeable Sodium-Ion Batteries. *J. Electrochem. Soc.* **147,** 1271–1273 (2000).

46. Stevens, D. A. & Dahn, J. R. The Mechanisms of Lithium and Sodium Insertion in Carbon Materials. *J. Electrochem. Soc.* **148,** A803–A811 (2001).

47. Chevrier, V. L. & Ceder, G. Challenges for Na-ion negative electrodes. *J. Electrochem. Soc.* **158,** A1011–A1014 (2011).

48. Komaba, S. *et al.* Redox reaction of Sn-polyacrylate electrodes in aprotic Na cell. *Electrochem. commun.* **21,** 65–68 (2012).

49. Darwiche, A. *et al.* Better cycling performances of bulk Sb in Na-ion batteries compared to Li-ion systems: An unexpected electrochemical mechanism. *J. Am. Chem. Soc.* **134,** 20805–20811 (2012).

50. Xu, Y., Zhu, Y., Liu, Y. & Wang, C. Electrochemical Performance of Porous Carbon / Tin Composite Anodes for Sodium-Ion and Lithium-Ion Batteries. *Adv. Energy Mater.* **3,** 128–133 (2013).

51. Qian, J. *et al.* High capacity Na-storage and superior cyclability of nanocomposite Sb / C anode for Na-ion batteries. *Chem. Commun.* **48,** 7070–7072 (2012).

52. Didier, C. *et al.* Electrochemical Na-Deintercalation from NaVO2. *Electrochem. Solid-State Lett.* **14,** A75–A78 (2011).

53. Hamani, D., Ati, M., Tarascon, J.-M. & Rozier, P. NaxVO2 as possible electrode for Na-ion batteries. *Electrochem. commun.* **13,** 938–941 (2011).

54. Alcántara, R., Jaraba, M., Lavela, P. & Tirado, J. L. NiCo2O4 Spinel : First Report on a Transition Metal Oxide for the Negative Electrode of Sodium-Ion Batteries. *Chem. Mater.* **14,** 2847–2848 (2002).

55. Sun, Q., Ren, Q.-Q., Li, H. & Fu, Z.-W. High capacity Sb2O4 thin film electrodes for rechargeable sodium battery. *Electrochem. commun.* **13,** 1462–1464 (2011).

56. Nagelberg, A. S. & Worrell, W. L. A Thermodynamic Study of Sodium-Intercalated TaS2 and TiS2. *J. Solid State Chem.* **29,** 345–354 (1979).

57. Mortazavi, M., Wang, C., Deng, J., Shenoy, V. B. & Medhekar, N. V. Ab initio characterization of layered MoS2 as anode for sodium-ion batteries. *J. Power Sources* **268,** 279–286 (2014).

58. Kim, J.-S. *et al.* The discharge properties of Na/Ni3S2 cell at ambient temperature. *J. Power Sources* **178,** 852–856 (2008).

59. Kim, T. B. *et al.* Electrochemical characteristics of Na/FeS2 battery by mechanical alloying. *J. Alloys Compd.* **449,** 304–307 (2008).

60. Kim, Y. *et al.* Composites: An Amorphous Red Phosphorus/Carbon Composite as a Promising Anode Material for Sodium Ion Batteries. *Adv. Mater.* **25,** 10488 (2013).

61. Molenda, J. & Stoklosa, A. Electronic and electrochemical properties of nickel bronze, NaxNiO2. *Solid State Ionics* **38,** 1–4 (1990).

62. Komaba, S., Takei, C., Nakayama, T., Ogata, A. & Yabuuchi, N. Electrochemical intercalation activity of layered NaCrO2 vs . LiCrO2. *Electrochem. commun.* **12,** 355–358 (2010).

63. Ding, J.-J., Zhou, Y.-N., Sun, Q. & Fu, Z.-W. Cycle performance improvement of NaCrO2 cathode by carbon coating for sodium ion batteries. *Electrochem. commun.* **22,** 85–88 (2012).

64. Chen, C.-Y. *et al.* Electrochemical and structural investigation of NaCrO2 as a positive electrode for sodium secondary battery using inorganic ionic liquid NaFSA-KFSA. *J. Power Sources* **237,** 52–57 (2013).

65. Shacklette, L. W., Jow, T. R. & Townsend, L. Rechargeable electrodes from sodium cobalt bronzes. *J. Electrochem. …* **135,** 2669–2674 (1988).

66. Saadoune, I., Maazaz, A., Ménétrier, M. & Delmas, C. On the NaxNi06Co0.4O2 System : Physical and Electrochemical Studies. *J. Solid State Chem.* **122,** 111–117 (1996).

67. Carlier, D. *et al.* The P2-Na2/3Co2/3Mn1/3O2 phase: structure, physical properties and electrochemical behaviour as positive electrode in sodium battery. *Dalt. Trans.* **40,** 9306–9312 (2011).

68. Sauvage, F., Laffont, L., Tarascon, J.-M. & Baudrin, E. Study of the insertion/deinsertion mechanism of sodium into Na0.44MnO2. *Inorg. Chem.* **46,** 3289–3294 (2007).

69. Kim, H. *et al.* Ab initio study of the sodium intercalation and intermediate phases in Na0.44MnO2 for sodium-ion battery. *Chem. Mater.* **24,** 1205–1211 (2012).

70. Hosono, E. *et al.* High power Na-ion rechargeable battery with single-crystalline Na0.44MnO2 nanowire electrode. *J. Power Sources* **217,** 43–46 (2012).

71. Tarascon, J. M., Guyomard, D. G., Wilkens, B., Mc Kinnon, W. R. & Barboux, P. Chemical and electrochemical insertion of Na into the spinel delta-MnO2 phase. *Solid State Ionics* **57,** 113–120 (1992).

72. Komaba, S., Mikumo, T. & Ogata, A. Electrochemical activity of nanocrystalline Fe3O4 in aprotic Li and Na salt electrolytes. *Electrochem. commun.* **10,** 1276–1279 (2008).

73. Komaba, S. *et al.* Electrochemical Insertion of Li and Na Ions into Nanocrystalline Fe3O4 and alpha-Fe2O3 for Rechargeable Batteries. *J. Electrochem. Soc.* **157,** A60–A65 (2010).

74. West, K., Zachau-Christiansen, B. & Jacobsen, T. Sodium insertion in vanadium oxides. *Solid State Ionics* **28-30,** 1128–1131 (1988).

75. Cushing, B. L. & Goodenough, J. B. Li2NaV2(PO4)3: A 3.7 V Lithium-Insertion Cathode with the Rhombohedral NASICON Structure. *J. Solid State Chem.* **162,** 176–181 (2001).

76. Lim, S. Y., Kim, H., Shakoor, R. A., Jung, Y. & Choi, J. W. Electrochemical and Thermal Properties of NASICON Structured Na3V2(PO4)3 as a Sodium Rechargeable Battery Cathode : A Combined Experimental and Theoretical Study. *J. Electrochem. Soc.* **159,** A1393–A1397 (2012).

77. Gopalakrishnan, J. & Rangan, K. K. V2(PO4)3: A Novel NASICON-Type Vanadium Phosphate Synthesized by Oxidative Deintercalation of Sodium from Na3V2(PO4)3. *Chem. Mater.* **4,** 745–747 (1992).

78. Uebou, Y., Kiyabu, T., Okada, S. & Yamaki, J. Electrochemical sodium insertion into the 3D-framework of Na3M2(PO4)3 (M=Fe, V). *Reports Inst. Adv. Mater. Study, Kyushu Univ.* **16,** 1–5 (2002).

79. Tripathi, R., Ramesh, T. N., Ellis, B. L. & Nazar, L. F. Scalable synthesis of tavorite LiFeSO4F and NaFeSO4F cathode materials. *Angew. Chem. Int. Ed. Engl.* **49,** 8738–8742 (2010).

80. Abraham, K. M. INTERCALATION POSITIVE ELECTRODES FOR RECHARGEABLE SODIUM CELLS. *Solid State Ionics* **7,** 199–212 (1982).

81. Yamada, Y., Doi, T., Tanaka, I., Okada, S. & Yamaki, J. Liquid-phase synthesis of highly dispersed NaFeF3 particles and their electrochemical properties for sodium-ion batteries. *J. Power Sources* **196,** 4837–4841 (2011).

82. Lu, Y., Wang, L., Cheng, J. & Goodenough, J. B. Prussian blue : a new framework of electrode materials for sodium batteries. *Chem. Commun.* **48,** 6544–6546 (2012).

83. Wang, L. *et al.* A Superior Low-Cost Cathode for a Na-Ion Battery **. *Angew. Chem. Int. Ed. Engl.* **52,** 1964–1967 (2013).

84. Hu, Y., Kong, W., Li, H., Huang, X. & Chen, L. Experimental and theoretical studies on reduction mechanism of vinyl ethylene carbonate on graphite anode for lithium ion batteries. *Electrochem. commun.* **6,** 126–131 (2004).

85. Weadock, N. *et al.* Determination of mechanical properties of the SEI in sodium ion batteries via colloidal probe microscopy. *Nano Energy* **2,** 713–719 (2013).

86. Ponrouch, A. *et al.* Towards high energy density sodium ion batteries through electrolyte optimization. *Energy Environ. Sci.* **6,** 2361–2369 (2013).

87. Zhang, S. S. A review on electrolyte additives for lithium-ion batteries. *J. Power Sources* **162,** 1379–1394 (2006).

88. Santner, H. J., Korepp, C., Winter, M., Besenhard, J. O. & Möller, K.-C. In-situ FTIR investigations on the reduction of vinylene electrolyte additives suitable for use in lithium-ion batteries. *Anal. Bioanal. Chem.* **379,** 266–271 (2004).

89. Zhang, S. S. Aromatic isocyanate as a new type of electrolyte additive for the improved performance of Li-ion batteries. *J. Power Sources* **163,** 567–572 (2006).

90. Roy, P., Berger, S. & Schmuki, P. TiO 2 Nanotubes : Synthesis and Applications. *Angew. Chem. Int. Ed. Engl.* **50,** 2904–2939 (2011).

91. Macak, J. M., Albu, S. P. & Schmuki, P. Towards ideal hexagonal self-ordering of TiO2 nanotubes. *Phys. status solidi* **1,** 181–183 (2007).

92. Peighambardoust, N.-S. & Nasirpouri, F. Manipulating morphology, pore geometry and ordering degree of TiO2 nanotube arrays by anodic oxidation. *Surf. Coatings Technol.* **235,** 727–734 (2013).

93. Wang, R. *et al.* Photogeneration of Highly Amphiphilic TiO 2 Surfaces **. *Adv. Mater.* **10,** 135–138 (1998).

94. Macák, J. M., Tsuchiya, H., Ghicov, A. & Schmuki, P. Dye-sensitized anodic TiO2 nanotubes ´. *Electrochem. commun.* **7,** 1133–1137 (2005).

95. Paulose, M., Varghese, O. K., Mor, G. K., Grimes, C. A. & Ong, K. G. Unprecedented ultra-high hydrogen gas sensitivity in undoped titania nanotubes. *Nanotechnology* **17,** 398–402 (2006).

96. Ghicov, A. *et al.* TiO 2 nanotubes : H+ insertion and strong electrochromic effects. *Electrochem. commun.* **8,** 528–532 (2006).

97. Macak, J. M., Schmidt-Stein, F. & Schmuki, P. Efficient oxygen reduction on layers of ordered TiO 2 nanotubes loaded with Au nanoparticles. *Electrochem. commun.* **9,** 1783–1787 (2007).

98. Linsebigler, A. L., Lu, G. & Yates, J. T. Photocatalysis on TiO2 surfaces: principles, mechanisms, and selected results. *Chem. Rev.* **95,** 735–758 (1995).

99. Oh, S.-H., Finones, R. R., Daraio, C., Chen, L.-H. & Jin, S. Growth of nano-scale hydroxyapatite using chemically treated titanium oxide nanotubes. *Biomaterials* **26,** 4938–4943 (2005).

100. Lakshmi, B. B., Dorhout, P. K. & Martin, C. R. Sol-gel template synthesis of semiconductor nanostructures. *Chem. Mater.* **9,** 857–862 (1997).

101. Sander, M. S., Côté, M. J., Gu, W., Kile, B. M. & Tripp, C. P. Template-Assisted Fabrication of Dense, Aligned Arrays of Titania Nanotubes with Well-Controlled Dimensions on Substrates. *Adv. Mater.* **16,** 2052–2057 (2004).

102. Bavykin, D. V., Friedrich, J. M. & Walsh, F. C. Protonated titanates and TiO2 nanostructured materials: synthesis, properties, and applications. *Adv. Mater.* **18,** 2807–2824 (2006).

103. Macak, J. M. & Schmuki, P. Anodic growth of self-organized anodic TiO 2 nanotubes in viscous electrolytes. *Electrochim. Acta* **52,** 1258–1264 (2006).

104. Tighineanu, A., Ruff, T., Albu, S., Hahn, R. & Schmuki, P. Conductivity of TiO2 nanotubes: Influence of annealing time and temperature. *Chem. Phys. Lett.* **494,** 260–263 (2010).

105. Lee, B.-G. *et al.* Formation behavior of anodic TiO2 nanotubes in fluoride containing electrolytes. *Trans. Nonferrous Met. Soc. China* **19,** 842–845 (2009).

106. Kowalski, D., Kim, D. & Schmuki, P. TiO2 nanotubes, nanochannels and mesosponge: Self-organized formation and applications. *Nano Today* **8,** 235–264 (2013).

107. Berger, S., Hahn, R., Roy, P. & Schmuki, P. Self-organized TiO2 nanotubes: Factors affecting their morphology and properties. *Phys. Status Solidi* **247,** 2424–2435 (2010).

108. Macak, J. M. *et al.* TiO2 nanotubes: Self-organized electrochemical formation, properties and applications. *Curr. Opin. Solid State Mater. Sci.* **11,** 3–18 (2007).

109. Yu, X., Li, Y., Wlodarski, W., Kandasamy, S. & Kalantarzadeh, K. Fabrication of nanostructured TiO2 by anodization: A comparison between electrolytes and substrates. *Sensors Actuators B Chem.* **130,** 25–31 (2008).

110. Berger, S. *et al.* The origin for tubular growth of TiO2 nanotubes: A fluoride rich layer between tube-walls. *Surf. Sci.* **605,** L57–L60 (2011).

111. Lockman, Z., Sreekantan, S., Ismail, S., Schmidt-Mende, L. & MacManus-Driscoll, J. L. Influence of anodisation voltage on the dimension of titania nanotubes. *J. Alloys Compd.* **503,** 359–364 (2010).

112. Macak, J. M., Hildebrand, H., Marten-Jahns, U. & Schmuki, P. Mechanistic aspects and growth of large diameter self-organized TiO2 nanotubes. *J. Electroanal. Chem.* **621,** 254–266 (2008).

113. Song, Y.-Y., Lynch, R., Kim, D., Roy, P. & Schmuki, P. TiO2 Nanotubes : Efficient Suppression of Top Etching during Anodic Growth. *Electrochem. Solid-State Lett.* **12,** C17–C20 (2009).

114. Albu, S. P. & Schmuki, P. Highly defined and ordered top-openings in TiO2 nanotube arrays. *Phys. status solidi - Rapid Res. Lett.* **4,** 151–153 (2010).

115. Valota, A. *et al.* Influence of water content on nanotubular anodic titania formed in fluoride/glycerol electrolytes. *Electrochim. Acta* **54,** 4321–4327 (2009).

116. Muscat, J., Swamy, V. & Harrison, N. M. First-principles calculations of the phase stability of TiO2. *Phys. Rev. B* **65,** 224112–1 (2002).

117. Liu, Z. *et al.* Nanostructured TiO2(B): the effect of size and shape on anode properties for Li-ion batteries. *Prog. Nat. Sci. Mater. Int.* **23,** 235–244 (2013).

118. Kunze, J., Seyeux, A. & Schmuki, P. Anodic TiO2 Layer Conversion : Fluoride-Induced Rutile Formation at Room Temperature. *Electrochem. Solid-State Lett.* **11,** K11–K13 (2008).

119. Ohtsuka, T., Guo, J. & Sato, N. Raman Spectra of the Anodic Oxide Film on Titanium in Acidic Sulfate and Neutral Phosphate Solutions. *J. Electrochem. Soc.* **133,** 2473–2476 (1986).

120. Asahi, R., Taga, Y., Mannstadt, W. & Freeman, A. J. Electronic and optical properties of anatase TiO2. *Phys. Rev. B* **61,** 7459–7465 (2000).

121. Tang, H., Prasad, K., Sanjinès, R., Schmid, P. E. & Lévy, F. Electrical and optical properties of Ti02 anatase thin films. *J. Appl. Phys.* **75,** 2042 (1994).

122. Pascual, J., Camassel, J. & Mathieu, H. Fine structure in the intrinsic absorption edge of TiO2. *Phys. Rev. B* **18,** 5606–5614 (1978).

123. Eufinger, K., Poelman, D., Poelman, H., Gryse, R. De & Marin, G. B. Photocatalytic activity of dc magnetron sputter deposited amorphous TiO2 thin films. *Appl. Surf. Sci.* **254,** 148–152 (2007).

124. Muñoz, A. G., Chen, Q. & Schmuki, P. Interfacial properties of self-organized TiO 2 nanotubes studied by impedance spectroscopy. *J. Solid State Chem.* **11,** 1077–1084 (2007).

125. Lynch, R. P., Ghicov, A. & Schmuki, P. A Photo-Electrochemical Investigation of Self-Organized TiO 2 Nanotubes. *J. Electrochem. Soc.* **157,** G76–G84 (2010).

126. Diebold, U. & Madey, T. E. Adsorption and electron stimulated desorption of NH3 / TiO2 (110). *J. Vac. Sci. Technol. A* **10,** 2327 (1992).

127. Sergentu, V. V. *et al.* Prediction of negative index material lenses based on metallo-dielectric nanotubes pss. *Phys. status solidi - Rapid Res. Lett.* **2,** 242–244 (2008).

128. Funk, S., Hokkanen, B., Burghaus, U., Ghicov, A. & Schmuki, P. Unexpected Adsorption of Oxygen on TiO 2 Nanotube Arrays : Influence of Crystal Structure. *Nano Lett.* **7,** 1091–1094 (2007).

129. Macak, J. M., Aldabergerova, S., Ghicov, A. & Schmuki, P. Smooth anodic TiO2 nanotubes: annealing and structure. *Phys. status solidi - Rapid Res. Lett.* **203,** R67–R69 (2006).

130. Albu, S. P., Tsuchiya, H., Fujimoto, S. & Schmuki, P. TiO2 Nanotubes - Annealing Effects on Detailed Morphology and Structure. *Eur. J. Inorg. Chem.* 4351–4356 (2010). doi:10.1002/ejic.201000608

131. Tighineanu, A., Albu, S. P. & Schmuki, P. Conductivity of anodic TiO2 nanotubes: Influence of annealing conditions. *Phys. status solidi - Rapid Res. Lett.* 1–5 (2013). doi:10.1002/pssr.201308221

132. Macak, J. M., Gong, B. G., Hueppe, M. & Schmuki, P. Filling of TiO2 Nanotubes by Self-Doping and Electrodeposition. *Adv. Mater.* **19,** 3027–3031 (2007).

133. *EC-Lab Software User ' s Manual, Version 10.2x*. 1–185 (2012).

134. Mabbott, G. A. An Introduction to Cyclic Voltammetry. *J. Chem. Educ.* **60,** 697–702 (1983).

135. Kissinger, P. T. & Heineman, W. R. Cyclic Voltammetry. *J. Chem. Educ.* **60,** 702–706 (1983).

136. Chronoamperometry. at <www.diss.fu-berlin.de/diss/servlets/MCRFileNodeServlet/FUDISS_derivate_000000003216/03_chapter3.pdf?hosts=>

137. *Analytical Electrochemistry: The Basic Concepts*. 1–3 at <www.asdlib.org/onlineArticles/.../Kelly.../PDF-6-Chronoamp.pdf>

138. Gamry Instruments. *Application Note-Basics of Electrochemical Impedance Spectroscopy*. 1–17 (2010). at <www.gamry.com>

139. Scribner Associates-Tutorial. *Electrochemical Impedance Spectroscopy (EIS): A Powerful and Cost- Effective Tool for Fuel Cell Diagnostics*. 1–5 at <www.scribner.com/files/tech-papers/Scribner Associates - Electrochemical Impedance Spectroscopy for Fuel Cell Research.pdf>

140. X-ray Diffraction (XRD). at <web.pdx.edu/-pmoeck/phy381/Topic5a-XRD.pdf>

List of Figures

List of Tables